

Image Evaluation and Optimization in Zone
Plate Coded Imaging

F. D. Kalk

Report No. 123
February, 1982

ACKNOWLEDGEMENTS

The guidance of James Forsyth and the support of the Laboratory for Laser Energetics and the Institute of Optics are gratefully acknowledged. Discussions with Dr. M. P. Givens proved very helpful. The work of Irving Goldstein and David Glocker was invaluable in establishing microfabrication at LLE. I am indebted to the following people for technical assistance: Luther Whitaker for electron microscope work, Joe Trovato and Sarah McGuire for zone plate fabrication, Bob Boni for laser hole drilling, and especially John Grosso for x-ray exposure expertise. Special thanks are due the LLE art department for the illustrations. The travel arrangements provided by Efron, Unlimited, added new meaning to the word luxury. Finally, this work is dedicated to Martin Leff and Sarah Swords, whose love and support have made everything possible.

ABSTRACT

Zone plate coded imaging (ZPCI) is a useful technique for imaging x-ray and particle emissions from laser-produced plasmas. Though past studies have developed a theory of ZPCI system parameters (e.g. resolution), image degradation has not been thoroughly explored, and optimization has not been studied. This thesis is the first treatment of image evaluation and optimization in ZPCI. Both theoretical and experimental studies are performed.

The theoretical construct begins with a simple categorization scheme for optical coded imaging systems. Equating ZPCI with a multiple exposure holographic process permits easy analysis of the reconstruction step. Image degradation is classified as either deterministic (artifacts) or random (noise).

Nonlinear ZPCI is treated for both absorption and phase reconstructions. The high diffraction efficiency and resolution of phase reconstructions can be offset by deterministic image degradation due to intermodulation effects. Ideally, it is possible to compensate for intermodulation, but practical phenomena (such as Fresnel diffraction in the recording step) tend to deter this.

The grain noise treatments of previous workers are extended to account for reconstruction mask density effects and object spatial frequency content. Noise is coupled to the image field and peaks at low frequencies. Shot noise is treated briefly and compared with grain noise.

The experiments performed are the first image evaluations in the x-ray region. Linear ZPCI is shown to have better image fidelity

than nonlinear ZPCI. The variation of artifacts with image size is also demonstrated. Qualitative studies of grain noise verify that phase reconstructions have higher SNR than absorption reconstructions. The variation of SNR with object size is also shown.

Optimization is a compromise between SNR, resolution, and nonlinearity; the images with highest SNR tend to suffer the most deterministic degradation. Measurable figures of merit are derived for determining image fidelity, and procedures are established for successful ZPCI implementation and image assessment.

TABLE OF CONTENTS

	<u>Page</u>
List of Tables.....	ix
List of Figures.....	x
List of Appendices.....	xii
CHAPTER I: INTRODUCTION.....	1
CHAPTER II: THEORY	7
2.1 Introduction.....	8
2.2 Coded Imaging.....	8
2.2.1 Optical Coded Imaging Schemes.....	9
2.2.2 Zone Plate Coded Imaging.....	15
2.3 Previous Theories.....	18
2.3.1 Review of Significant Results.....	19
2.3.2 Limitations of Previous Theories.....	21
2.4 New Theory.....	23
2.4.1 Hologram Equivalent to the Coded Image of a Point Object.....	24
2.4.2 Generalized Multiple Exposure Hologram Analysis.....	28
2.4.3 Linear ZPCI.....	29
2.4.4 Survey of Recording Step Detectors.....	31
2.4.5 Nonlinear ZPCI.....	35
2.4.5.1 Absorption Reconstructions.....	35
2.4.5.2 Phase Reconstructions.....	43
2.4.5.3 Artifact Formation.....	48

TABLE OF CONTENTS, Cont.

	<u>Page</u>
2.4.5.4 Comments on the Feasibility of Quantitative Nonlinear ZPCI.....	50
2.4.6 Noise.....	53
2.4.6.1 Grain Noise Mechanisms.....	54
2.4.6.2 Mathematical Formulation of Noise.....	56
2.5 Information and Optimization.....	62
 CHAPTER III: EXPERIMENTAL INVESTIGATIONS.....	 64
3.1 Introduction.....	65
3.2 Image Evaluation Devices.....	65
3.2.1 X-Ray Exposure System.....	65
3.2.2 Optical Reconstruction Bench.....	67
3.3 Discussion of Validity of Various Figures of Merit.....	70
3.4 Studies of Nonlinear ZPCI.....	72
3.4.1 Film Calibration.....	72
3.4.2 Variation of Image Fidelity with Nonlinearity..	75
3.4.3 Role of Object Information Content in Artifact Formation.....	82
3.4.3.1 Effect of Object Size.....	82
3.4.3.2 Effect of Object Modulation.....	83
3.5 Studies of Grain Noise.....	87
3.5.1 Grain Noise of Uniformly Exposed Plates.....	87
3.5.2 SNR for Absorption and Phase Reconstructions of a Disk Object.....	88
3.5.3 Variation of SNR with Object Size.....	95
3.6 Summary of Experimental Work.....	98

TABLE OF CONTENTS, Cont.

	<u>Page</u>
CHAPTER IV: OPTIMIZATION OF ZPCI.....	99
4.1 Introduction.....	100
4.2 Review of Results.....	100
4.2.1 Deterministic Degradation.....	100
4.2.2 Noise.....	101
4.3 Optimization.....	101
4.3.1 Efficiency of Single Information Element.....	101
4.3.2 Estimation of Deterministic Degradation.....	102
4.3.2.1 Artifact Distribution for a Uniform Object...	103
4.3.2.2 Artifact Distribution for an Object with Contours.....	103
4.3.3 Noise Strength and Object Size.....	108
4.3.4 Optimization Procedures.....	109
4.3.4.1 Example: α -Particle Imaging.....	113
4.3.4.2 Example: X-Ray Imaging.....	114
CHAPTER V: SUMMARY AND SUGGESTIONS FOR FUTURE INVESTIGATIONS.....	119
REFERENCES.....	122

LIST OF TABLES

<u>Table</u>	<u>Page</u>
3.1 Relative Flux Measured at Third Order Images of Three-Disk Object.....	81
3.2 Optical Densities and Reconstruction Efficiencies for Original and Copy Coded Images.....	94

LIST OF FIGURES

<u>Figure</u>	<u>Page</u>
1.1 ZPCI Recording Step.....	3
1.2 ZPCI Reconstruction Step.....	4
2.1 Optical Image Encoding Methods.....	10
2.2 Optical Image Decoding Methods.....	12
2.3 Simple Classification Scheme for Coded Imaging Systems.....	13
2.4 ZPCI Recording System.....	16
2.5 ZPCI Reconstruction System with Relay Lens and D.C. Block.....	16
2.6 The Single Exposure Equivalent Hologram.....	27
2.7 Comparison of t_a -E Curves for Two X-Ray Films at 4.95 keV.....	32
2.8 Moire Pattern of Two Closely Spaced Overlapping Zone Plates.....	40
2.9 Moire Pattern of Two Overlapping Zone Plates with Large Separation.....	40
2.10 Flux Diversion Due to Moire Diffraction Effect for Two Overlapping Zone Plates.....	42
2.11 Spatial Frequency of Grain Noise in Zone Plate Coded Imaging.....	59
3.1 Exposure System Schematic.....	66
3.2 X-Ray Exposure System Cross-Section.....	68
3.3 Optical Reconstruction Bench.....	69
3.4 Calibration of RAR 2491 Film for X-Rays Excited at Two Voltages in Titanium Anode Henke Tube Source.....	74
3.5 Object Used for Comparison of "Linear" and Nonlinear Reconstructions.....	76

LIST OF FIGURES, Cont.

<u>Figure</u>		<u>Page</u>
3.6	Reconstruction of "Linear" and Nonlinear Coded Images.....	78
3.7	Square Root of Relative Flux Versus Hole Area for Three Cases.....	81
3.8	Schematic Diagram and Reconstructions of Disk-Pair Object.....	84
3.9	Apparatus for Measuring Light Scattered from Uniformly Exposed Plate Specimens.....	89
3.10	Relative Scattered Power Versus Spatial Frequency for Uniformly Exposed 649-F Plates....	90
3.11	Comparison of Absorption and Phase Reconstructions of 20 μm Diameter Disk Object...	91
3.12	Reconstruction of Large Object.....	96
4.1	Images of X-Ray and α -Particle Emissions in ICF Studies.....	115
A.1	Zone Plate Fabrication Sequence.....	130
A.2	Schematic Diagram of Reactive Sputter Etcher.....	132
A.3	Ultrathick Zone Plate Fabrication.....	133
A.4	Scanning Electron Micrograph of a Mylar Zone Plate Mold.....	135
A.5	Scanning Electron Micrograph of a Thick Zone Plate.....	137
A.6	Photograph Illustrating Nonvertical Sidewalls of a Zone Plate Mold.....	140

LIST OF APPENDICES

	<u>Page</u>
APPENDIX I: Film Processing Methods.....	126
APPENDIX II: Thick Zone Plate Fabrication.....	128

CHAPTER I

INTRODUCTION

Zone plate coded imaging (ZPCI) is an established method for microscopy of x-ray and particle emissions from laser-produced plasmas. However, no complete treatment of the ZPCI system has been performed, and the result is that only qualitative data analysis has been used. Indeed, there is still some debate concerning the validity of ZPCI as an imaging system. This thesis focusses on the remaining problems and presents a cohesive formulation of ZPCI.

Before an outline of the thesis is sketched, it is necessary to briefly describe ZPCI. ZPCI is essentially a two-step process. In the initial, or recording, step (Figure 1.1), the source of interest, $f(\underline{r})$, casts a shadow of a Fresnel zone plate (of transmission $g(\underline{r}')$) onto a suitable detector (usually photographic film). The recorded shadowgram $h(\underline{r}'')$ is a coded image of the source distribution in that each radiating point (or very small volume) in the source will cast a shadow of the zone plate onto the film; the position, size, and irradiance of any shadow are uniquely determined by the position and strength of the source point casting that shadow. Hence, the coded image is composed of many such zone plate shadows, effectively encoding a three-dimensional source distribution into a two-dimensional shadowgram (or coded image).

In the second, or reconstruction, step, the processed shadowgram (now a transparency) is transilluminated with a collimated laser (see Figure 1.2). A Fresnel zone plate will focus a collimated laser to an infinite set of axial foci; each zone plate shadow in the shadowgram similarly focusses the laser to axial foci, in effect reconstructing the source point that originally cast that zone plate shadow. Thus, the x-ray or particle source is reconstructed, or decoded, as an axial

ZPCI RECORDING SYSTEM

UR
LLE 

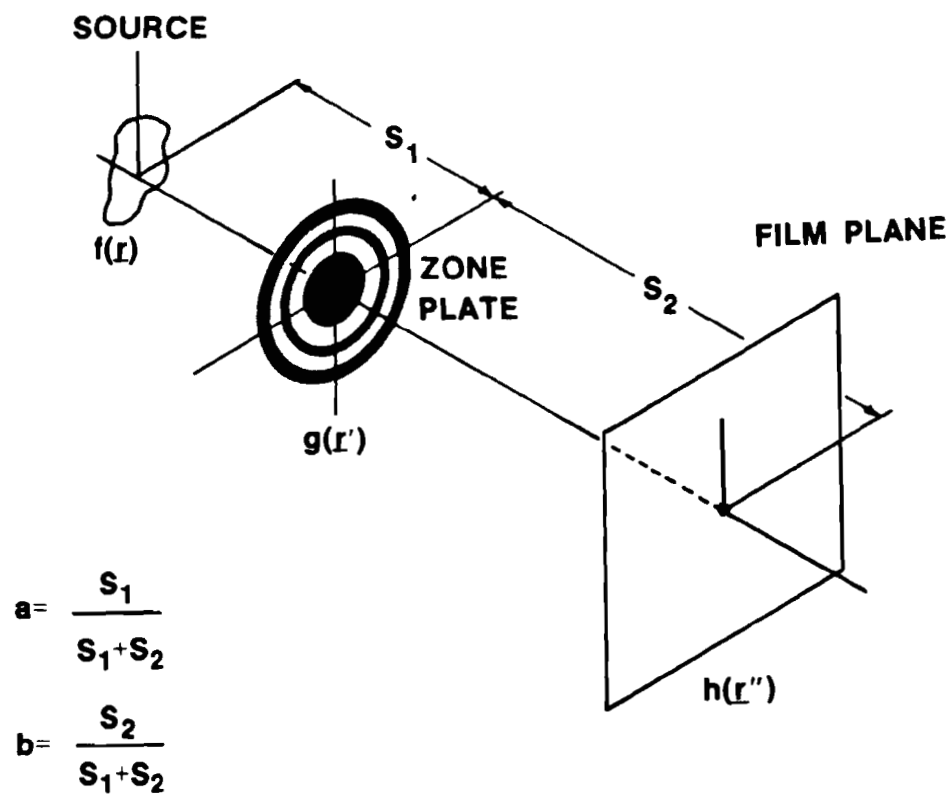
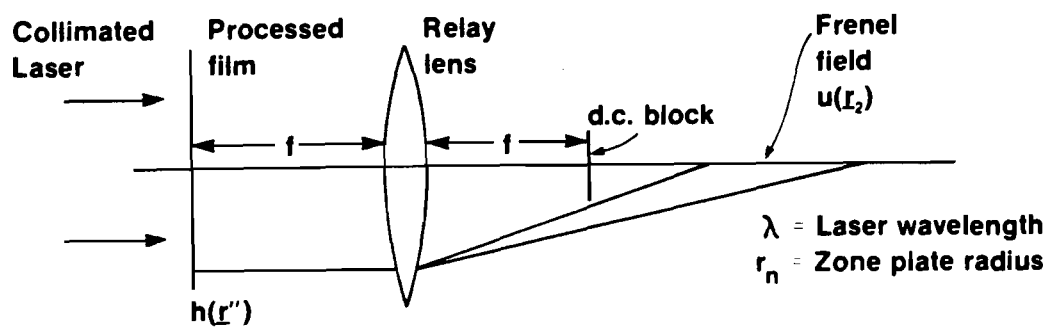


Figure 1.1

ZPCI Reconstruction Step



X120

Figure 1.2

set of visible light images (called image orders). The coded image also transmits a d.c. background component, which can be removed with a focussing lens and blocking filter, as shown in Figure 1.2. In this case, the virtual image orders (corresponding to the virtual foci of the Fresnel zone plate) are relayed by the lens into real image space.

Critical to the success of ZPCI are several factors. First, the Fresnel zone plate in the recording step must contain no structure small enough to cause significant diffraction of the source radiation, i.e. the shadow cast by any source point must be "sharp." Secondly, since the shadowgram reconstructs several image orders, the various images must not interfere with each other. Finally, the overlapping zone plate shadows in the coded image must not mutually interfere; otherwise, loyal images are not produced.

A complete treatment of ZPCI entails exploration of three areas. Fundamental system parameters, such as resolution, must first be defined. Then image degradation mechanisms must be treated. These mechanisms include both deterministic and random effects. Finally, a thorough optimization exercise must be drafted, including the definitions of figures of merit adequately describing the system performance. The first area, i.e. the description of the system, has been treated completely. Image degradation mechanisms have been partially studied, and the area of optimization is virtually untouched.

This dissertation constitutes the most complete examination of ZPCI to date. The issues cited above are defined and explored,

enabling the user of ZPCI to establish confidence limits in any situation. Chapter II is a complete theoretical treatment of image degradation mechanisms in ZPCI. This treatment is founded on the similarity between ZPCI and multiple exposure holography (MEH), whereby the extensive work in holography simplifies the analysis of noise and nonlinear processes in ZPCI. Chapter III is an experimental investigation in which the concepts of Chapter II are both confirmed and clarified. Chapter III contains the first detailed experimental comparison of nonlinear and linear ZPCI. It is also the only study performed in the x-ray region, which is the spectral region of interest in ZPCI. Also, grain noise is explored in Chapter III, and the effect of object size, the importance of which is predicted in the theory, is illustrated.

Chapter IV is the prime contribution of the thesis. It is a presentation of a procedure for optimizing ZPCI in practice. The behavior of image degradation mechanisms is reviewed, and simple design rules are established. Examples are presented to illustrate the results of the study. Chapter V contains a brief summary of the work and suggestions for future endeavors in ZPCI.

CHAPTER II

THEORY

2.1 Introduction

This chapter is a comprehensive treatment of the theoretical aspects of ZPCI. Major contributions in the field are reviewed, and new results are presented. This theory is a cohesive formulation that will aid in the creation of rules for optimization of ZPCI.

The theme of this chapter is that ZPCI is but one of a host of optical coded imaging systems, and fitting it into a general coded imaging scheme permits the exploitation of its similarity with other types of coded imaging. Following a brief discussion of general coded imaging, the basic mathematical structure of ZPCI is introduced. Then previous work in ZPCI is reviewed, and unsolved problems are identified. An original theoretical formulation is then presented, beginning with the establishment of an equivalence between ZPCI and multiple exposure holography (MEH). Deterministic image degradation is discussed in detail, with attention given to phase and amplitude reconstructions and to the possibility of quantitative nonlinear imaging. Then noise is treated, and results are obtained that contrast with previous workers' assertions. Finally, information capacity is treated briefly as a prelude to the chapter on optimization.

2.2 Coded Imaging

The expression coded imaging describes any imaging process in which image formation is accomplished in a sequence of two or more steps. In the initial, or encoding, step, information from the object is modulated and detected. After appropriate processing of this coded information, a decoding, or reconstruction, step is performed to obtain the desired image. The nature of the steps depends upon the object.

The following is a brief outline of the factors that affect the use of coded imaging. A classification of coded imaging systems is presented, and examples clarify the organization. A short introduction to information and noise poses questions which arise when coded imaging is used.

2.2.1 Optical Coded Imaging Schemes

A desired image can usually be obtained with direct imaging methods. Occasionally, however, conventional optics does not provide sufficient information, while coded imaging does. A practical example is the recent progress in inertial confinement fusion, which has necessitated the microscopy of objects that emit high energy radiations; the failure of reflective and refractive optical elements to adequately image these emissions is the impetus for this work.

Once coded imaging is chosen, the radiation to be detected determines the recording step. If the object is not self-luminous, its anticipated optical properties and the desired information must be considered for adequate illumination to be provided. The coherence of the detected radiation dictates the nature of the modulation; coherent radiation can be interferometrically modulated, while incoherent radiation is readily coded by shadowgraphy, or coded aperture recording. The recording medium considered here is restricted to photographic film and similar detectors because the reconstruction methods treated will be optical. The transmittance versus exposure (t - E) character of the detector after processing is therefore important. Figure 2.1 illustrates the two recording methods.

The reconstruction is determined by the recording method. Much

OPTICAL IMAGE ENCODING METHODS

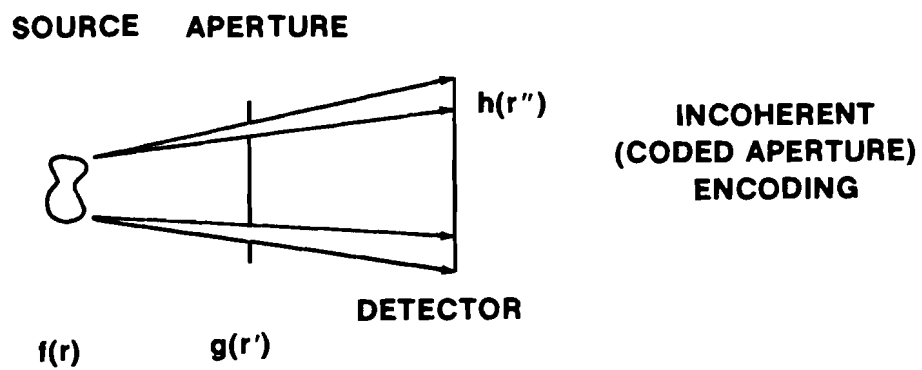
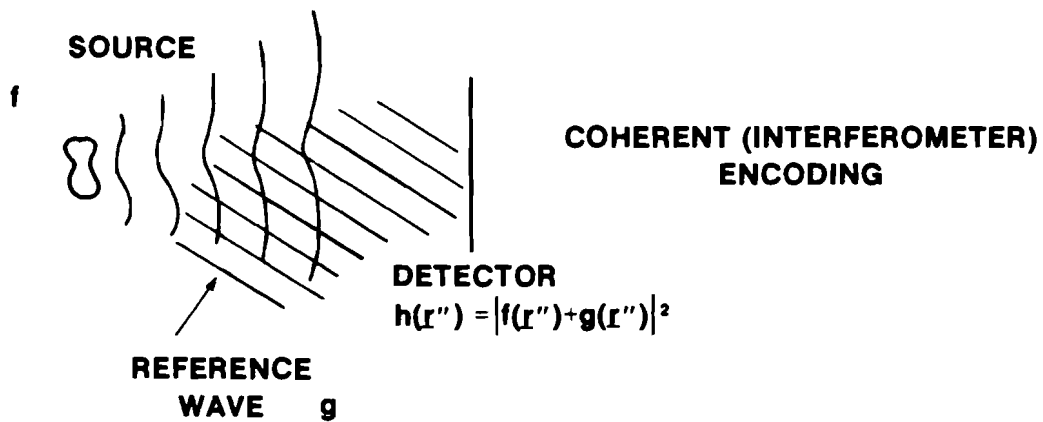


Figure 2.1

as encoding, decoding can be classified as incoherent or coherent (see Figure 2.2); however, a coded imaging system need not encode and decode with radiations of the same degree of coherence. Figure 2.3 is a chart categorizing some coded imaging systems according to the combination of encoding and decoding steps used for each. Some examples follow.

Example 1: incoherent encoding / incoherent decoding

pinhole array coded aperture imaging

As depicted in Figure 2.1, the incoherent source radiation shadows a random pinhole array onto film. The encoding process is described as:

$$f(\underline{r}) * g(\underline{r}') = h(\underline{r}'')$$

where $f(\underline{r})$ is the source emission distribution, $g(\underline{r}')$ is the mask transparency function, and $h(\underline{r}'')$ is the exposure distribution. The reconstruction is formed by convolving $h(\underline{r}'')$ with $k(\underline{r}''')$, as in figure 2.2. Proper choice of k will yield $g(\underline{r}') * k(\underline{r}''') = 1$. Then

$$v(\underline{r}_2) = h(\underline{r}'') * k(\underline{r}''') = f(\underline{r}).$$

This case is instructive because it is the only case of its type in which the autocorrelation of the mask function is a delta function. Thus, the encoding and decoding steps can use the same mask form.

Example 2: coherent recording / coherent reconstruction

holography

The radiation from the object and some reference wave interfere, and a recording is made. Reconstruction is achieved by illuminating the processed hologram with the reference wave, whereupon the object is reconstructed.

$$\text{Recording: } E = |R + O|^2 = |R|^2 + |O|^2 + R^*O + RO^*$$

$$\text{Film characteristic: } t = \gamma E$$

$$\text{Reconstruction: } I = Rt = R\gamma(|R|^2 + |O|^2) + |R|^2\gamma O + R^2\gamma O^*$$

OPTICAL IMAGE DECODING METHODS

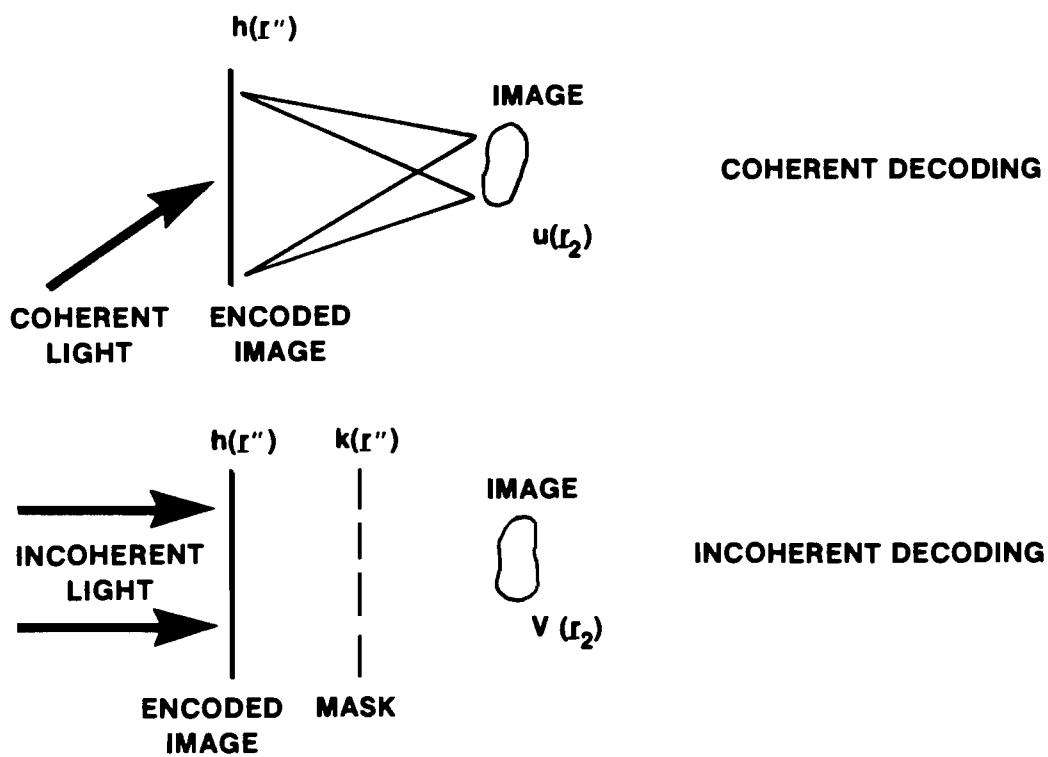


Figure 2.2

X263

SIMPLE CLASSIFICATION SCHEME FOR CODED IMAGING SYSTEMS

UR
LLE 

		<i>RECORDING METHOD</i>	
		COHERENT	INCOHERENT
<i>RECONSTRUCTION METHOD</i>	COHERENT	HOLOGRAPHY	ZPCI MEH
	INCOHERENT		CODED APERTURE IMAGING

Figure 2.3

Here R and O are the reference and object wave amplitudes at the hologram plane, E is the exposure in the recording step, t is the amplitude transmittance after processing, γ is a constant, and I is the image wave. Note that the reconstruction contains a term proportional to the object wave.

Example 3: incoherent recording / coherent reconstruction

multiple exposure holography

Many holograms are recorded successively on an emulsion. Each hologram recording is linear in amplitude, but the addition of hologram recordings is linear in intensity. Each hologram may have its own reference wave, and a desired image can be reconstructed by illuminating the hologram with the appropriate reference wave.

$$\text{Recording: } E = \sum_i E_i = \sum_i |R_i + O_i|^2$$

$$\text{Film response: } t = \gamma E$$

$$\text{Reconstruction: } I_i = R_i t = R_i \gamma \sum_i E_i$$

Subscript i denotes the i^{th} hologram recording. Some algebra leads to the result that R_i will reconstruct O_i . If all R_i are identical, all O_i will be reconstructed simultaneously, just as in ZPCI.

It should be pointed out that the film characteristics have not been considered in detail. Since film processing techniques can be varied to increase the SNR of ZPCI, the issue of film response must be addressed. This is the subject of Section 2.4.4. Image degradation (both random and deterministic) must also be considered. The following paragraphs briefly introduce noise and information.

The term noise refers to the random fluctuation of the signal in an information channel, but it has always been subjected to a more flexible interpretation. Deterministic image degradation in ZPCI due

to recording system nonlinearity has often been termed noise, when in fact it is information. Noise in optical systems, particularly holography, is a difficult problem and as such has been treated in a crude fashion. One of the goals of this theoretical treatment is to model the noise properties of ZPCI.

Information capacity is related to noise. The information content of an object can be defined as the product of the number of resolvable elements in the object and the number of gray levels in an element. The information capacity of an imaging system refers to the ability of the system to faithfully image the object. Factors that affect information capacity include film resolution, f-number, and similar quantities. Of importance in coded imaging is the nature of the encoding step, which imposes inherent limitations on the information capacity. Further discussion of information and noise requires a more thorough treatment of ZPCI, which now proceeds.

2.2.2 Zone Plate Coded Imaging

What follows is a sketch of the relevant mathematical details of ZPCI. Figure 2.4 illustrates the ZPCI recording step. The object, with emission distribution $f(\underline{r})$, casts a shadow of the zone plate of transmittance $g(\underline{r}')$ onto film. The film exposure $h(\underline{r}'')$ is related to $f(\underline{r})$ and $g(\underline{r}')$ by the expression

$$h(\underline{r}'') = \frac{1}{4\pi(s_1 + s_2)^2} \iint d^2\underline{r} f(\underline{r}) g(a\underline{r}'' + b\underline{r}), \quad [2.1]$$

where $\underline{r}' = a\underline{r}'' + b\underline{r}$, and a , b , s_1 , and s_2 are shown in Figure 2.4. The transmission function for a Fresnel zone plate with inner zone radius r_1 , total zone number n , and total radius r_n , is given by

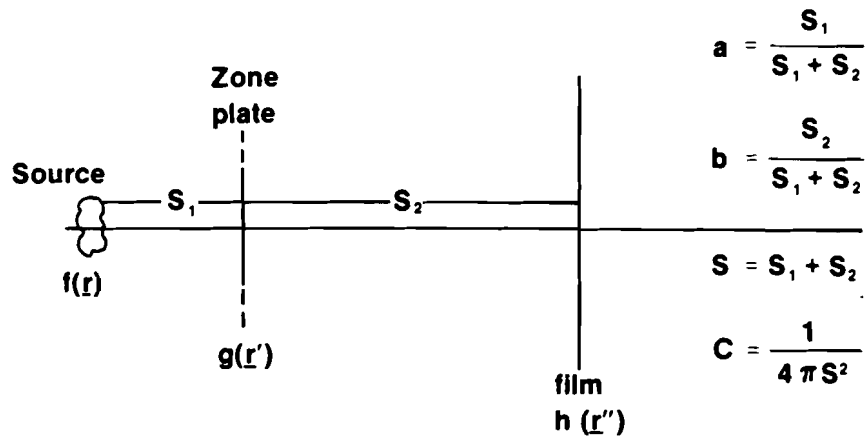


Figure 2.4 ZPCI Recording System

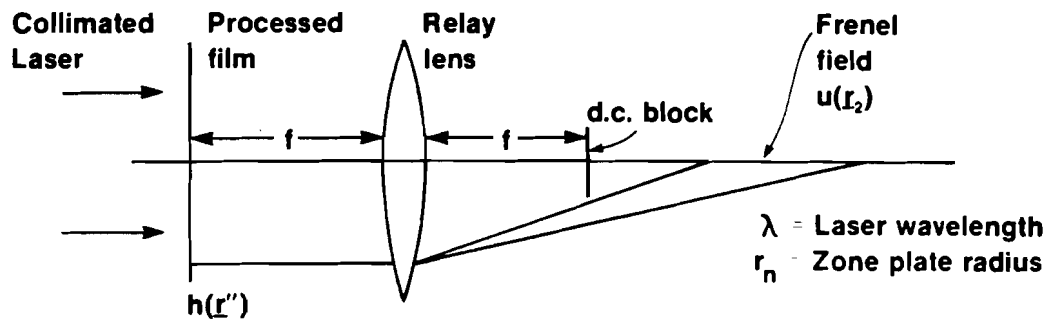


Figure 2.5 ZPCI Reconstruction System with Relay Lens and D.C. Block

X120

$$g(\underline{r}') = \left\{ \frac{1}{2} - \frac{1}{\pi i} \sum_{\substack{m=-\infty \\ \text{odd}}}^{\infty} \frac{1}{m} \exp\left[\frac{i\pi m}{r_1^2} (\underline{r}')^2 \right] \right\} \text{circ}\left(\frac{\underline{r}'}{r_n}\right) \quad [2.2]$$

$$= \left\{ \frac{1}{2} + \bar{g}(\underline{r}') \right\} \text{circ}\left(\frac{\underline{r}'}{r_n}\right) .$$

Since the recording is a shadowgram, the zone plate must contain no structure small enough to cause significant diffraction of the object radiation. Further, for imaging to be practical, the object area must be much smaller than the zone plate area.

The exposure is a convolution of the object emission distribution and the coded aperture transmission function. Typically, the film response is complicated, especially for soft x-rays (energies of 1-8 keV). For reasons which will become clear, the film should respond such that $t_a(\underline{r}'')$, the amplitude transmittance after processing, is linearly related to $h(\underline{r}'')$.

Reconstruction can be accomplished in several ways, one of which has widespread acceptance (see Figure 2.5). The processed coded image, with amplitude transmittance $t_a(\underline{r}'')$, is transilluminated by a collimated laser, and the Fresnel diffraction pattern is viewed downstream. The d.c. component of the Fresnel pattern is undesirable, so it is eliminated by placing a lens and blocking filter after the coded image. The Fresnel pattern is symmetrical about the plane of the coded image, with real and virtual orders; by means of the lens and filter, the virtual orders can be viewed without the presence of the d.c. light, thereby acquiring improved contrast. The expression for the Fresnel pattern (without relay lens and blocking filter) is

$$u(\underline{r}_2) = \frac{\exp\left(\frac{2\pi i d}{\lambda}\right)}{i\lambda d} \iint d^2 \underline{r}'' t_a(\underline{r}'') \exp\left\{ \frac{i\pi}{\lambda d} (\underline{r}_2 - \underline{r}'')^2 \right\} , \quad [2.3]$$

where $u(\underline{r}_2)$ is the reconstruction field, d is the distance into the field from the coded image, and λ is the wavelength of the laser used for reconstruction.

Equation [2.3] can be modified to account for the relay lens and filter, but the change is unimportant for present purposes, so it is omitted. For special values of d , the field assumes the form of a deconvolution of $h(\underline{r}'')$ with amplitude proportional to the original object distribution $f(\underline{r})$. Since the coded image is a Fresnel transform of the object while the image field is a Fresnel transform of the coded image, matching the scales of the two transforms results in the proper reconstruction of the object.

If $t_a(\underline{r}'')$ is linearly related to $h(\underline{r}'')$, the imaging process is "loyal." However, in many practical situations, t_a vs h is nonlinear; the effect of the nonlinearity is to introduce artifacts in the reconstruction field, but these artifacts are ordinarily small. In any event, the quantities that can be linearly related are the object distribution $f(\underline{r})$ and the image field $u(\underline{r}_2)$. What is measured is $|u(\underline{r}_2)|^2$, and thus ZPCI cannot be considered linear in even the strictest case; the image irradiance must usually be considered as only a relative indicator of $f(\underline{r})$. This fact is discussed later.

2.3 Previous Theories

This section is a review of previous studies of ZPCI. Four groups have made contributions to the field, and the contributions have been fairly exclusive in focus. This disconnection might explain the fact that the optical reconstruction has not been thoroughly explored, resulting in inadequate investigation of image degradation.

Following a review of previous work, the limitations of that work will be discussed, and questions will arise which require attention.

2.3.1 Review of Significant Results

ZPCI was first suggested for use in x-ray astronomy.⁽¹⁾ However, it lay dormant until Barrett and his colleagues applied it to nuclear medicine.⁽²⁻⁵⁾ Barrett's contributions include the use of transform theory to analyze the image code,^(3,5) off-axis zone plate theory (spatial heterodyning),⁽²⁾ the treatment of shot noise,⁽⁵⁾ and the use of ZPCI for gamma ray imaging in nuclear medicine.⁽⁴⁾

Barrett pointed out that coded imaging is closely related to the transform properties of zone plates. He introduced the concept of bandwidth to describe the efficiency of the encoding process. The realization that there are low and high spatial frequency cutoffs for every Fourier component of a zone plate transmission function enabled Barrett to propose matched imaging, a method employing half-tone screens to spatially heterodyne the object spectrum and match it to the response bandwidth of the coded aperture. Thus, Barrett could image large objects, such as those of interest in nuclear medicine.

Several papers on coded imaging have originated at l'Institute d'Optique in Orsay, the principle investigators being Fonroget and Brunol.⁽⁶⁻⁹⁾ With interest initially in nuclear medicine, they have recently used annular apertures for microscopy of laser-produced plasmas. Because of their interest in generalized coded aperture imaging, they have used digital reconstructions. Their theory has focussed on associating an MTF with any coded imaging system, and they assert that annular aperture codes are superior to zone plates:

The advantages of digital deconvolution are that quantitative information about object emissions and freedom from image degradation are possible. Digital reconstructions have been employed by several workers, notably Fenimore and Cannon,⁽¹⁰⁾ who use uniformly redundant arrays because of the uniformity of the sidelobes in the autocorrelation function (recall Example 1, Section 2.2.1).

The description of ZPCI as a linear system is proper if the incoherent (autocorrelation) method of reconstruction is used. Due to practical difficulties, this is sparingly used. In addition, the transfer function derived for ZPCI by the French workers appears to be in conflict with that obtained by Ceglio.⁽¹¹⁾ This difference will be discussed later.

The principal contributor to ZPCI is Ceglio.⁽¹¹⁻¹⁴⁾ His is the definitive work on the deterministic theory of ZPCI. He performed a cursory study of reconstruction artifacts due to recording nonlinearity. Also, he applied ZPCI to microscopy of laser-produced plasmas.

Ceglio pointed out that, in the ideal case, linearity in ZPCI (with coherent reconstruction) exists between object emittance and image field amplitude. Because only image irradiance can be measured, ZPCI is not a linear system, but its transfer properties are still important. Ceglio showed that a system impulse response function can be derived for the primary order image. He also derived and evaluated a "coherent transfer function" for linear ZPCI, with which he showed the system frequency response to be effectively flat from d.c. out to some cutoff value.

Ceglio found that the effect of nonlinear recording is the introduction of artifacts in the reconstructions. For the absorption case,

he indicated the general trends of artifact contributions, such as dependence upon reconstruction order and object size. Ceglio concluded that artifact contributions are small enough to be insignificant in the primary image. He also expanded slightly on Barrett's shot noise analysis, with essentially identical results.

The work of Gur^(15,16) stands as a complement to the work of Ceglio. Gur's primary contribution was to investigate high order reconstructions with their attendant increase in spatial resolution. Perhaps as important was his identification of speckle due to grain noise as a major image degradation mechanism. Gur also applied coherence theory to the recording step, illustrating some points which are put to use in this current work.

Spatial resolution is enhanced with increasing order number since the effective f-number of the system is inversely proportional to order number. The increase in the number of resolution elements and the decrease in available reconstruction flux at high orders result in a commensurate decrease in SNR. The noise in ZPCI is due mainly to speckle from grain noise in the reconstruction mask. Though Gur identified the origin of the noise, he did not study it completely.

Strictly speaking, the recording process is not described by ray optics, and Gur's treatment of the propagation of the mutual intensity through the system shows this. From this treatment, Gur concluded that the recorded zones do not have "sharp" edges, but instead have altered profiles which affect the flux distribution in reconstruction.

2.3.2 Limitations of Previous Theories

There are two topics in ZPCI which have received insufficient

treatment: information capacity/image degradation and system optimization. Any treatment of information capacity must account for the properties of detectors, such as noise and sensitivity, as well as inherent system resolution due to diffraction phenomena. Neither shot noise nor grain noise has been adequately studied. The image degradation due to recording nonlinearities is deterministic and hence is not noise. Artifacts can in principle provide information about the object; this aspect of ZPCI is unexplored.

Despite all that is written about ZPCI, design rules have not been devised, probably because of the disagreement among the various authors about the fidelity of the process. Barrett and Horrigan,⁽⁵⁾ Fonroget, et. al.,^(6,7) and Ceglio⁽¹¹⁾ have all calculated functions related to the transfer properties of ZPCI, and the three groups appear to obtain different answers. Ceglio's calculation of the first order coherent transfer function indicates an essentially flat frequency response from d.c. to the cutoff value, while Fonroget, et. al., calculate an MTF for the first order system which, they assert, is poor. In fact, an MTF cannot be associated with ZPCI since the system is not linear in the incoherent quantities. Further, Fonroget's calculation is based on a zone plate with ten zones, while Ceglio points out that the zone plate should have at least 100 zones to have a high quality transfer function. The debate will undoubtedly continue.

Existing theories must be extended to optimize ZPCI. Questions remaining to be answered include: Can reconstruction efficiency be increased? What zone plate is best in a given situation? What is noise, what is nonlinearity, and how do they affect a practical system? These questions provide the motivation for this work.

2.4 New Theory

The purpose of this section is the development of a theory which can be used to optimize ZPCI. The result of the theory should be the derivation of some figure(s) of merit indicating the fidelity of ZPCI in any situation. Consequently, an accurate treatment of image degradation should receive priority.

The theory proceeds as follows. The equivalence of ZPCI and multiple exposure holography (MEH) is established. This exercise consists of two parts, (1) the equating of the coded image of a point object and some single exposure hologram, and (2) the extension of the equivalence to coded images of extended objects and multiple exposure holograms. This equivalence yields a closed form expression which is applicable to the study of nonlinear imaging and permits the investigation of noise by extension of the results of noise studies in holography.

The investigation of nonlinear imaging is preceded by an analysis of "linear" imaging, in which it is shown that linear imaging is not always loyal. The study of nonlinearity is broader than previous work in that it accounts for both amplitude and phase modulation properties of the reconstruction mask. Also, artifacts are treated as information rather than noise, and it is shown that, in practice, nonlinear ZPCI presents problems which warrant further treatment.

Noise is investigated in detail, and the results depart from those of other workers. It is shown that the noise is concentrated at the image, presenting serious problems unless proper care is taken when using ZPCI. The decrease in SNR with increase in object size is also explained.

2.4.1 Hologram Equivalent to the Coded Image of a Point Object

In order to establish an equivalence between the coded image of a point object and some hologram, a hologram with the same exposure distribution as the coded image must be found. With this equivalence established, any coded image may be considered to be equivalent to some multiple exposure hologram, and the reconstructed image field is easily investigated.

Recall the recording equation for ZPCI:

$$h(\underline{r}'') = \frac{1}{4\pi(s_1 + s_2)^2} \iint d^2\underline{r} f(\underline{r}) g(a\underline{r}'' + b\underline{r}). \quad [2.1]$$

The coded image for a point object can be obtained by substituting $f(\underline{r}) = a_1 \delta(\underline{r} - \underline{R}_1)$, where \underline{R}_1 is the location of the point object.

$$\text{Then} \quad h(\underline{r}'') = \frac{a_1}{4\pi(s_1 + s_2)^2} g(a\underline{r}'' + b\underline{R}_1) \quad [2.4]$$

is a magnified version (i.e. a point projection) of the zone plate, centered at $\underline{r}'' = -\frac{b}{a} \underline{R}_1$ with a size of $1/a$ times the size of the zone plate. When the expression for g is expanded using [2.2], eq. [2.4] becomes

$$\begin{aligned} h(\underline{r}'') &= \frac{a_1}{4\pi(s_1 + s_2)^2} \left\{ \frac{1}{2} - \frac{1}{\pi i} \sum_{\substack{m=-\infty \\ \text{odd}}}^{\infty} \frac{1}{m} \exp \left[\frac{i\pi m}{2} (a\underline{r}'' + b\underline{R}_1)^2 \right] \right\} \\ &= a_1 C_0 \left\{ \frac{1}{2} + \bar{g}(a\underline{r}'' + b\underline{R}_1) \right\}, \end{aligned} \quad [2.5]$$

$$\text{where } C_0 = \frac{1}{4\pi(s_1 + s_2)^2} \text{ and } \bar{g}(\underline{r}') = -\frac{1}{\pi i} \sum_{\substack{m=-\infty \\ \text{odd}}}^{\infty} \frac{1}{m} \exp \left[\frac{i\pi m}{2} |\underline{r}'|^2 \right].$$

Several authors have discussed the similarity between zone plates

and holograms, and calculations have been made of the amplitudes of reference and subject waves.⁽¹⁷⁻²⁵⁾ However, none calculated the hologram reference and subject amplitude distributions that interfere to form a true Fresnel zone plate. Horman⁽²⁵⁾ came close to the correct answer but did not succeed because he made an incorrect assumption about hologram formation.

The exposure in hologram formation is

$$E_H = |A_R + A_S|^2 = |A_R|^2 + |A_S|^2 + A_R^* A_S + A_R A_S^* , \quad [2.6]$$

where A_R is the amplitude of the reference wave at the hologram, and A_S is the subject wave amplitude. Since [2.5] contains a series, [2.6] must also contain a series in order to be equated to [2.5]. But if both A_R and A_S contain a series, the products of terms in eq. [2.6] will produce cross terms that might complicate the equivalence analysis. Now, consider $\bar{g}(\underline{r}')$:

$$\bar{g}(\underline{r}') = \pm \frac{1}{2} \quad (\text{real})$$

$$\text{and } |\bar{g}(\underline{r}')|^2 = \frac{1}{4} \quad (\text{a constant}).$$

Choosing A_R as a constant and A_S as a constant multiplied by \bar{g} will yield a hologram with the proper E_H . Specifically,

$$\begin{aligned} E_H &= |A_H|^2 = |A_R|^2 + |A_S|^2 + A_R^* A_S + A_R A_S^* \\ &= |A_R|^2 + |A_S|^2 + \text{constant} \cdot \bar{g}. \end{aligned}$$

$$\text{Let } A_S = -\frac{A_O}{\pi i} \sum_{\substack{m=-\infty \\ \text{odd}}}^{\infty} \frac{1}{m} \exp \left[\frac{i\pi m}{r_1^2} (a\underline{r}'' + b\underline{R}_1)^2 \right] .$$

$$\text{Then } E_H = a_1 C_O \left\{ \frac{1}{2} - \frac{1}{\pi i} \sum_{\substack{m=-\infty \\ \text{odd}}}^{\infty} \frac{1}{m} \exp \left[\frac{i\pi m}{r_1^2} (a\underline{r}'' + b\underline{R}_1)^2 \right] \right\} . \quad [2.6]$$

Thus, $|A_R|^2 - \frac{A_o^2}{4} = \frac{a_1 C_o}{2}$ and $2A_R A_o = a_1 C_o$. These equations are satisfied if $A_R = \frac{\sqrt{a_1 C_o}}{2}$ and $A_o = \sqrt{a_1 C_o}$. More explicitly,

$$A_S = -\frac{2A_R}{\pi i} \sum_{\substack{m=-\infty \\ \text{odd}}}^{\infty} \frac{1}{m} \exp \left(\frac{i\pi m}{r_1^2} (a\underline{r}'' + b\underline{R}_1)^2 \right).$$

The amplitude at the hologram plane is

$$A_H = A_R + A_S = \sqrt{a_1 C_o} \left\{ \frac{1}{2} - \frac{1}{\pi i} \sum_{\substack{m=-\infty \\ \text{odd}}}^{\infty} \frac{1}{m} \exp \left(\frac{i\pi m}{r_1^2} (a\underline{r}'' + b\underline{R}_1)^2 \right) \right\},$$

which is just the interference of a plane wave of amplitude $\frac{\sqrt{a_1 C_o}}{2}$ propagating along the normal to the hologram plane and a subject wave given by the series A_S . The locations of the point sources that create the subject wave correspond to the real and virtual foci of the Fresnel zone plate of primary focal length $r_1^2/a\lambda$ centered at $\underline{r}'' = -\frac{b}{a} \underline{R}_1$. The relative strength of the m^{th} order point source, with the first order strength normalized to unity, is $A_m = \frac{1}{m}$. Figure 2.6 is a schematic diagram of the layout of the hologram, which will be called the single exposure equivalent hologram (SEEH).

A point of interest about the SEEH is that the linear reconstruction yields both the subject and reference waves, but the conjugate waves are identical to the original ones, so the conjugate reconstruction is "loyal." Another point is that in this short analysis, certain high order phase effects have been ignored, but it is easy to show that they are not significant. Further, in reality, the recording has limited lateral extent due to the finite zone plate size. This can be included in a $\text{circ}[(\underline{r}'' + \frac{b}{a} \underline{R}_1)/(r_n/a)]$ factor in eq. [2.6]. The circ

THE SINGLE EXPOSURE EQUIVALENT HOLOGRAM

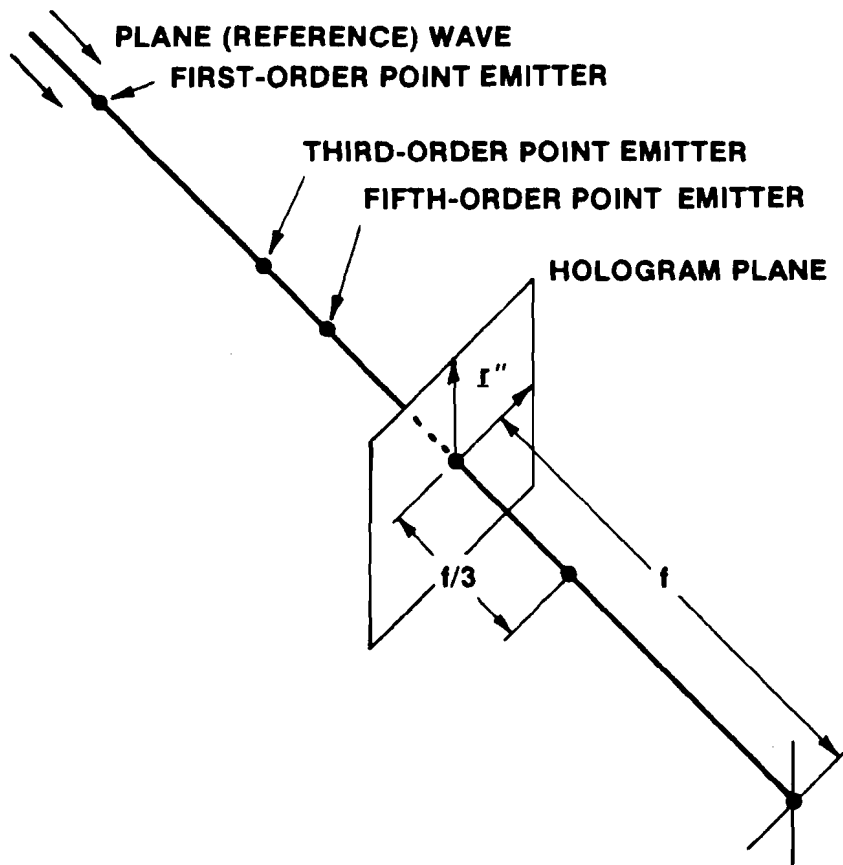


Figure 2.6

factor results in the reconstruction of a point source being an Airy disk rather than a true point.

2.4.2 Generalized Multiple Exposure Hologram Analysis

The SEEH analysis can be generalized to account for extended objects. This amounts to finding a multiple exposure hologram equivalent to the zone plate coded image of an arbitrary source. For simplicity, only planar sources will be considered. An extended source can be described as:

$$f(\underline{r}) = \sum_j a_j \delta(\underline{r} - \underline{R}_j). \quad [2.7]$$

The a_j can be constrained to lie between 0 and 1 without loss of generality. The exposure for the shadowgram of $f(\underline{r})$ is

$$h(\underline{r}'') = \sum_j \frac{a_j}{4\pi(s_1 + s_2)^2} g(a\underline{r}'' + b\underline{R}_j). \quad [2.8]$$

Note that with $0 \leq a_j \leq a_{\max}$, the exposure due to any source point will have a value between 0 and $a_{\max}/[4\pi(s_1 + s_2)^2]$. This can be incorporated into the multiple exposure hologram that has the exposure equivalent to $h(\underline{r}'')$. With $A_R^{(j)}$ and $A_S^{(j)}$ the j^{th} reference and subject wave amplitudes at the hologram plane, the exposure at the hologram plane can be written:

$$E_H = \sum_j E_j = \sum_j |A_R^{(j)} + A_S^{(j)}|^2$$

$$\text{or } E_H = \sum_j C_O a_j \left| \frac{1}{2} - \frac{1}{\pi i} \sum_{\substack{m=-\infty \\ \text{odd}}}^{\infty} \frac{1}{m} \exp \left[\frac{i\pi m}{r_1} (a\underline{r}'' + b\underline{R}_j)^2 \right] \right|^2. \quad [2.9]$$

The exposure for the j^{th} hologram is a binary distribution that varies between 0 and $C_O a_j$, and the total exposure varies between 0 and $\sum_j C_O a_j$.

$$\text{Let } c_j = \frac{\sqrt{c_{oj} a_j}}{2} \text{ and } \bar{g}(a_{\underline{r}''} + b_{\underline{R}_j}) = -\frac{1}{\pi i} \sum_{\substack{m=-\infty \\ \text{odd}}}^{\infty} \frac{1}{m} \exp\left(\frac{i\pi m}{2r_1} (a_{\underline{r}''} + b_{\underline{R}_j})^2\right).$$

$$\text{Then } E = \sum_j |c_j + 2c_j \bar{g}_j|^2 = \sum_j 2c_j^2 (1 + 2\bar{g}_j), \quad [2.10]$$

where $\bar{g}_j = \bar{g}(a_{\underline{r}''} + b_{\underline{R}_j})$.

Equation [2.10] is the hologram exposure equivalent to the ZPCI exposure produced by the source distribution in eq. [2.7]. Again, each E_j in eq. [2.10] must be multiplied by a circ function that accounts for the finite extent of the zone plate. The hologram equivalent to the coded image of a multi-point object will be called MEEH, for multiple exposure equivalent hologram.

Coupling the exposure (either eq. [2.8] or [2.10]) with the response of the recording medium reveals the image field just as in holography. Also, noise studies in holography can be adapted to the analysis of noise in ZPCI. The remainder of this chapter concentrates on the exploitation of the established equivalence.

2.4.3 Linear ZPCI

The next few paragraphs illustrate the application of the MEEH analysis to "linear" ZPCI. The analysis shows that, even for the linear case, it is possible to obtain images that are not faithful reconstructions of the object. This infidelity can be related to the coherence properties of the reconstruction process.

Linear ZPCI is defined as the case in which the coded image exhibits linearity between recording exposure and reconstruction amplitude transmittance (as pointed out earlier, ZPCI is never linear; only t-E is). Thus the coded image amplitude transmittance is given by

$$t_a(\underline{r}''') = \gamma \sum_j 2C_j^2 (1 + 2\bar{g}_j), \quad [2.11]$$

where γ is a normalization constant defined such that $0 \leq t_a \leq 1$. Clearly, $\gamma = 1/\sum_j 4C_j^2$. The reconstruction is accomplished mathematically by multiplying $t_a(\underline{r}''')$ by the original reference wave, which is a constant. Eq. [2.11] defines the field just after the coded image in Fig. 2.5; the field contains the original recording information and is thus a faithful reconstruction of the object.

There are two important points here. First, for many types of radiation, the amplitude transmittance of a film after processing is not proportional to the exposure. For example, for x-rays, optical density is usually found to be linear with exposure.⁽²⁶⁻²⁸⁾ Secondly, the field is not measurable; the irradiance is. Hence, the coherent nature of the decoding process can affect the image.

Consider the coded image of two point sources which are separated by the lateral resolution distance of the zone plate system in use. The reconstruction of this coded image will be a double peaked irradiance distribution, but the distance between the peaks will not be the same as the true (magnified) distance between the two original points. This image shifting property of ZPCI is independent of the recording linearity; it is due to the fact that the image is the absolute square of the sum of the complex amplitudes corresponding to the two separate point sources rather than the sum of the separate irradiances. This property of coherent imaging systems is illustrated in reference 29.

The two-point object is not the only case in which coherent effects cause image distortion. An edge will be shifted from its actual position in ZPCI. Edge shift in coherent optical systems is well known.⁽²⁹⁾

2.4.4 Survey of Recording Step Detectors

The principal application of ZPCI is microscopy of x-ray and α -particle emissions from laser-produced plasmas.^(13,48) The recording medium and its response to the radiation depend not only on the radiation but on the processing steps prior to reconstruction. Hence, a discussion of the various detection/processing scenarios is in order.

Traditionally in photography, the response of film to radiation is described by the relationship between exposure (E) and post-developed optical density (D). Holographers prefer to work with the t-E curve outlined earlier because of the coherent nature of laser light. For the same reason, the t-E curve is the important quantity in ZPCI. D and t are related by the equation $t = \exp[-1.15 D]$.

The x-ray response of silver halide emulsions depends upon the energy of the photons.^(26-28,30) For soft x-rays, film sensitivity can vary by a factor of ten over a fairly small energy range (1-8 keV). Figure 2.7 illustrates the t_a -E curve for two films at a photon energy of 4.95 keV. The No Screen film exhibits D-E linearity at 4.95 keV for $D < 1.41$, adequate density for ZPCI. Thus, $t_a = \exp(-\alpha E)$ for No Screen at 4.95 keV. Recall, though, that α varies with photon energy. The RAR 2490 film in Figure 2.7 cannot be described by an operating curve for soft x-rays. An empirical function describing the film's response in the 0.5 - 8.0 keV region is:

$$D = \log_{10} \{ 1 + \text{antilog}_{10} [A(\epsilon) \log_{10} E + B(\epsilon)] \}, \quad [2.12]$$

where $A(\epsilon)$ and $B(\epsilon)$ are energy-dependent parameters. Because of its low grain density, RAR 2490 film is not able to stop x-rays more energetic than about 8 keV.

The hard x-ray response (> 8 keV) of films is fairly simple:

COMPARISON OF t_g -E CURVES FOR TWO
X-RAY FILMS AT 4.95 KeV
(CORRECTED FOR FOG)

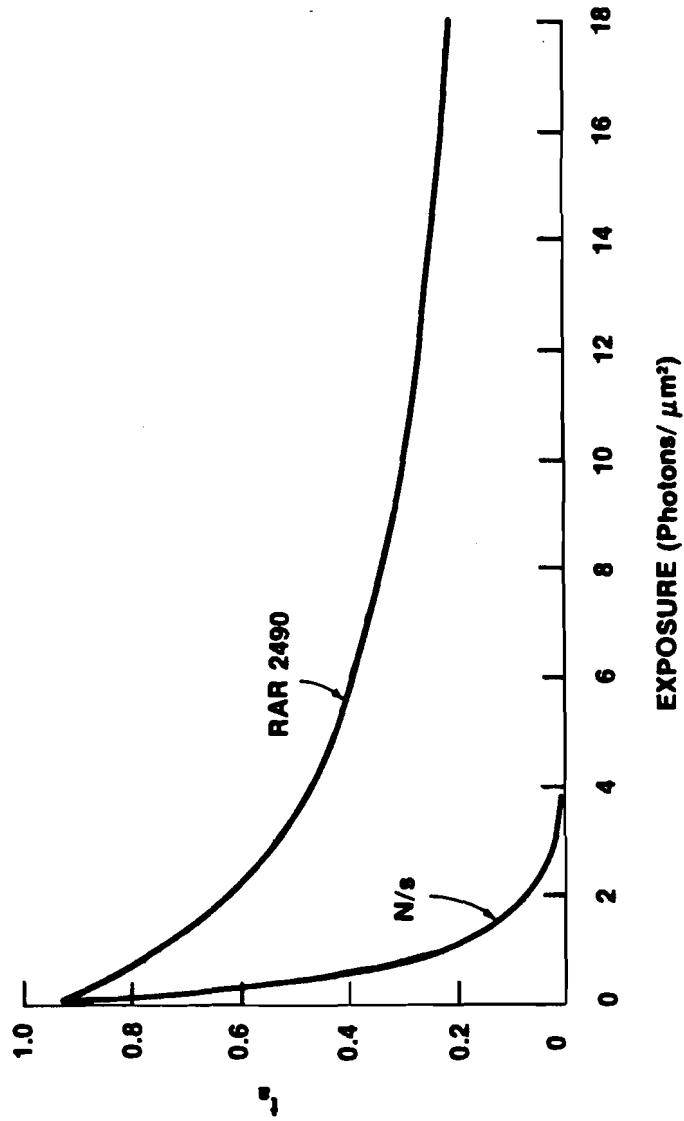


Figure 2.7

$$t_a = t_o \exp[-1.15 \sigma E], \quad [2.13]$$

where σ is a slowly varying function of energy (σ varies by a factor of ten between 8 keV and 100 keV). Eq. [2.13] was used by Ceglio⁽¹¹⁾ in his nonlinearity studies. Both equations presented above imply a nonlinear t-E behavior. However, the spectrum of recorded x-rays in laser fusion is never mono-energetic, and the film can be expected to exhibit a response that varies with the spectrum. This does not exclude even a linear t-E response, evidence for which will be presented in the experimental section.

The α -particles in laser fusion studies have energies in the range of 3-4 MeV and can be recorded with track detectors, such as cellulose nitrate. Damage sites in the molecular structure of a detector are produced along the path of a particle travelling through the medium. Subsequent immersion of the medium in an etchant (typically an alkyl solution) results in an etch rate along the particle path significantly greater than the (bulk) etch rate of the undamaged medium. If the detector is thin enough, this "development" process can produce holes through the medium coincident with the particle paths.

A coded image recorded on a track detector may be contact-copied onto a photographic film. This requires thin, opaque track detectors so that only holes etched through the medium will pass light during copying. Cellulose nitrate absorbs green light and thus can be copied with it. Other detectors, such as CR-39 (a polycarbonate), are clear; a way to copy such detectors would be to flash a thin metal coating (e.g. aluminum) onto the surface before copying, thereby producing holes in an opaque medium.

Copying the coded image permits versatile film processing. The

light flux passing through the medium is proportional to the recorded particle flux. Using visible light in copying allows control of linearity, just as in holography. The t-E curve for visible light usually exhibits a strong quadratic nonlinearity along with a much weaker cubic contribution. A polynomial approximation to the t-E curve for Kodak 649-F holographic plate is⁽³¹⁾

$$t = 0.92 - 0.575 \cdot 10^{-3} E - 0.137 \cdot 10^{-3} E^2 + 0.735 \cdot 10^{-6} E^3, \quad [2.14]$$

where E is in units of microjoules per square centimeter.

Whatever the method of detection, silver grain emulsion is generally used as the reconstruction mask. The diffraction efficiency of the mask can be increased by bleaching the emulsion as is done in holography. Bleaching converts the optically dense silver to transparent silver halide. Chang and George⁽³⁸⁾ used the Lorentz-Lorenz equation to calculate the dielectric constant ϵ of an emulsion of tiny silver halide particles of dielectric constant ϵ_2 embedded in a gelatin of dielectric constant ϵ_1 with volumetric fill fraction f:

$$\epsilon = \epsilon_1 + \frac{3f\epsilon_1}{\frac{\epsilon_2 + 2\epsilon_1}{\epsilon_2 - \epsilon_1} - f} \quad [2.15]$$

Lamberts⁽³⁷⁾ showed that there exists a reasonably linear relationship between prebleached optical density and post-bleached optical path length for emulsions in which the exposure is not extremely high and the emulsion thickness is constant. It is thus reasonable to expect a linear relationship between exposure and post-bleached optical path for bleached hard x-ray coded images. The complex transmittance is then

$$t_p(\underline{r}'') = t_o \exp[iyE(\underline{r}'')], \quad [2.16]$$

where t_o is a constant less than or equal to unity.

This short survey has not fully addressed the behavior of films, but it has introduced the relevant t-E response functions. Other aspects of film response are explored as the need arises.

2.4.5 Nonlinear ZPCI

The results of Section 2.4.4 imply the need for a study of nonlinear ZPCI. As already mentioned, Ceglio⁽¹¹⁾ analyzed the first-order image in nonlinear ZPCI and concluded that source emission contours are preserved in the image. However, his analysis is incomplete. A thorough study of nonlinear ZPCI must analyze all nonlinearities and images.

The treatment here proceeds as follows. The responses of two important detectors are analyzed, and the magnitude of any artifact is easily found. It is shown that even-order artifacts provide information about odd-order image fidelity, making quantitative nonlinear ZPCI possible in principle. However, a realistic parametric description is not precise, and a section is devoted to a discussion of the practical aspects of ZPCI, especially Fresnel diffraction in the recording step. The results of this study serve as groundwork for much of the chapter on optimization.

2.4.5.1 Absorption Reconstructions

Absorption reconstruction masks are produced by two methods, (1) processing of direct x-ray recordings and (2) processing visible light copies of track detector recordings. Equations [2.13] and [2.14] are therefore important. Equation [2.13] is the more complex of the two, so analysis of it will illustrate the general procedure:

$$t_a = t_o \exp(-1.15 \sigma E). \quad [2.13]$$

Recall the ZPCI exposure for a multi-point object:

$$E = \sum_j 2C_j^2 (1 + 2\bar{g}_j) = \sum_j 4C_j^2 \left(\frac{1}{2} + \bar{g}_j\right). \quad [2.10]$$

A general expression for the t-E relationship (assuming a characteristic curve can be applied here) can be written

$$t_a(\underline{r}''') = \sum_{k=0}^{\infty} \alpha_k \left[\sum_j 4C_j^2 \left(\frac{1}{2} + \bar{g}_j\right) \right]^k, \quad [2.17]$$

where the α_k are expansion coefficients. If t-E is of the same form as eq. [2.13], then

$$\alpha_k = \frac{(-1.15\sigma)^k}{k!},$$

where $D = \sigma E$. For example, for E in photons per square micron, at 8 keV energy No Screen film exhibits σ equal to about one density unit per photon per square micron. Equation [2.17] becomes

$$t_a(\underline{r}''') = \sum_{k=0}^{\infty} \frac{(-1.15\sigma)^k}{k!} \left[\sum_j 4C_j^2 \left(\frac{1}{2} + \bar{g}_j\right) \right]^k.$$

In order to expand the sum over j, it is necessary to assume that the object has a definite number of points, say N. Employing the multinomial expansion formula yields

$$t_a(\underline{r}''') = \sum_{k=0}^{\infty} \left[(-1.15\sigma)^k \sum_{k_j} \frac{E_1^{k_1} E_2^{k_2} \dots E_N^{k_N}}{k_1! k_2! \dots k_N!} \right], \quad [2.18]$$

where $E_j = 4C_j^2 \left[\frac{1}{2} + \bar{g}(\underline{a}_{R_j} + \underline{b}_{R_j}) \right]$ and the sum denoted by \sum_{k_j} is taken over all nonnegative integers k_1, k_2, \dots, k_N for which $k_1 + k_2 + \dots + k_N = k$. Eq. [2.18] is the generalized nonlinear t-E equation for D-E linearity. E_j is the j^{th} point-exposure.

Equation [2.18] is easily analyzed. Note that \sum_{k_j} can be studied

for one value of k at a time, i.e. $\sum_{k=0}^{\infty}$ can be studied term by term. For a given k , $\sum_{k_j}^j$ has N^k terms, N of which are of the form $(E_j)^k/k!$. Now, since $(\frac{1}{2} + \bar{g}_j)^k = \frac{1}{2} + \bar{g}_j$, then $E_j^k = 4^k C_j^{2k} (\frac{1}{2} + \bar{g}_j)$. [2.19]

Thus, a nonlinearity will generate some terms which are image terms.

The d.c. term in eq. [2.18] is

$$t|_{d.c.} = 1. \quad [2.20a]$$

The linear (image) term is

$$\begin{aligned} t|_{k=1} &= -1.15 \sigma \sum_{j=1}^N E_j \\ &= -4.6 \sigma \sum_{j=1}^N C_j^2 (\frac{1}{2} + \bar{g}_j). \end{aligned} \quad [2.20b]$$

Since for each value of k , there are N image terms, these terms can be incorporated into the primary transmittance expression:

$$t|_{\text{primary}} = \sum_{k=1}^{\infty} \frac{(-4.6 \sigma)^k}{k!} \sum_{j=1}^N C_j^{2k} (\frac{1}{2} + \bar{g}_j). \quad [2.20c]$$

A fraction of about N^{1-k} of the amplitude in the k^{th} order nonlinearity is image contribution, which is divided between the (equivalent) reference and object waves derived in the equivalent hologram analysis. Most of the image flux is due to the linear transmittance term because the coefficients in the series for $t_a(\underline{r}'')$ decrease quickly for large k (for linear $D \ll E$).

Artifact contributions arise from all terms in [2.18] that are not in eq. [2.20]. Some points of interest, outlined by Ceglio, are: (1) Artifacts with an even number of the $(E_j)^{k_j}$ as factors will focus into the even orders and in principle will not hinder the images (which fall in odd orders). Ceglio calls these "even point correlations."

(2) All artifacts have coefficients reduced by the k -exponent and the factorials in eq. [2.18]. Hence, even the odd-point correlations, which focus in odd orders, are reduced in importance relative to their primary image counterparts.

(3) When artifacts arise, phase effects occur which can degrade the image. Ceglio states that phase effects will be a defocussed background contribution, but this is not so for multi-point correlations in which artifacts can focus in image orders.

(4) The strength of artifacts is dependent upon the amount of overlap of the contributing zone plates. [However, if the object size in ZPCI is restricted to be small compared with the zone plate, and a substantial number of zones is assumed, say 25, then the overlap area of a two-point moire is about half the open area of the zone plate. This approximation is correct for all k . Hence, for small objects, the degree of nonlinearity in the recording is the factor that determines the strength of the moire effects.]

High order artifacts have amplitude transmittance contributions that decrease in a way elucidated by rewriting eq. [2.18] as

$$t_a(\underline{r}'') = \sum_{k=0}^{\infty} \left[(-1.15\sigma)^k \sum_{k_j} \frac{4^k C_1^{2k_1} C_2^{2k_2} \cdots C_N^{2k_N}}{k_1! k_2! \cdots k_N!} \left(\frac{1}{2} + \bar{g}_1 \right)^{k_1} \left(\frac{1}{2} + \bar{g}_2 \right)^{k_2} \cdots \left(\frac{1}{2} + \bar{g}_N \right)^{k_N} \right]. \quad [2.18a]$$

Eq. [2.18a] indicates that for a high order artifact, the product of the k_j 's can be less than k , so the factorial does not always decrease an artifact more than its image counterpart. However, the coefficient will decrease because of the C_j 's.

Ceglio intended to show that artifacts are greatly reduced in importance relative to the first order image. However, he neglected several factors. Imperfect shadowcasting in the recording step causes each $E_j(\underline{r}'')$ to contain even as well as odd-order coefficients. Thus, even-point correlations can focus in odd orders and degrade images (see Section 2.4.5.4). Also, sharp contours in the object can produce strong artifacts (Section 2.4.5.3). Finally, the strongest artifact is the linear grating produced by the overlap of two zone plates.⁽³²⁻³⁴⁾ It affects all orders because it diffracts light out of the image wave. Figures 2.8 and 2.9 show the moire patterns for two overlapping zone plates at different separations.

The linear grating can be traced to the cross terms in the summation over the k_j in equation [2.18a]. Consider the two-point object given by $f(\underline{r}) = \delta(\underline{r} - \underline{R}_1) + \delta(\underline{r} - \underline{R}_2)$. Equation [2.18a] will have the form

$$\sum_{\substack{n=-\infty \\ \text{odd}}}^{\infty} \frac{1}{n} \exp \left[\frac{i\pi n}{r_1} (a\underline{r}'' + b\underline{R}_1)^2 \right] \sum_{\substack{m=-\infty \\ \text{odd}}}^{\infty} \frac{1}{m} \exp \left[\frac{i\pi m}{r_1} (a\underline{r}'' + b\underline{R}_2)^2 \right].$$

The dominant terms in this "cross-sum" are those in which m and n are small, say ± 1 , and for which the artifacts strongly affect the region of interest in the Fresnel field. For moire zone plates, the focal distance is given by

$$d_{\text{moire}} = d_M = \frac{r_1^2}{\lambda a^2 (m + n)} \quad [2.21a]$$

while for the real images the focal distance is

$$d_I = \frac{r_1^2}{\lambda a^2 p}, \quad [2.21b]$$



Figure 2.8 Moiré Pattern of Two Closely Spaced Overlapping Zone Plates

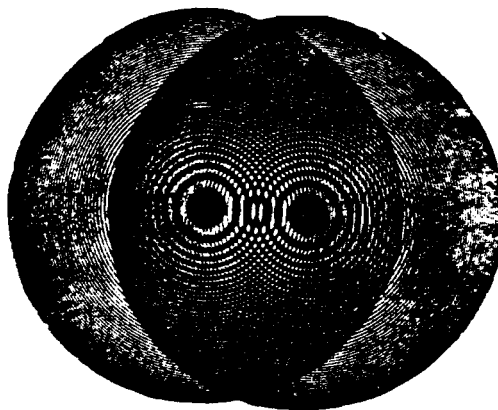


Figure 2.9 Moiré Pattern of Two Overlapping Zone Plates with Large Separation

where p is the reconstructed image order. Since m , n , and p are all odd, then $d_M \neq d_I$, and the interference of moire artifacts with images should be minimal. Consider, however, the case for which $m = -n$: here, $d_M = \infty$, and the artifact does not focus. Then, for $\underline{R}_2 = -\underline{R}_1$ (this is for simplicity, but generality is not lost), the terms of interest are

$$\begin{aligned} \frac{1}{m} \exp \left[\frac{i\pi m}{r_1^2} (a\underline{r}'' + b\underline{R}_1)^2 \right] \frac{1}{(-m)} \exp \left[\frac{-i\pi m}{r_1^2} (a\underline{r}'' - b\underline{R}_1)^2 \right] \\ = -\frac{1}{m^2} \exp \left[\frac{4i\pi mab}{r_1^2} \underline{r}'' \cdot \underline{R}_1 \right] . \end{aligned} \quad [2.22]$$

For a given m , equation [2.22] represents a linear grating with grating vector parallel to the line joining the two object points and having period $L = r_1^2 / (4a^2 R_{1,m})$. If $m = 1$, the grating is quite strong relative to the other moire effects and will degrade all images because it acts to diffract light out of the image wave. If the grating is a factor in a third-order nonlinearity (i.e. equation [2.22] would be multiplied by an E_j in [2.18]), it causes the construction of an "image" laterally shifted relative to the actual image. This effect is illustrated in Figure 2.10; only the image wave and the first nonlinearly diffracted orders are shown (i.e. $m = 1$). The shift of these "moire image waves" from the real image wave is given by

$$x = \frac{m\lambda z}{L} , \quad [2.23]$$

where x is the displacement, z is the axial distance into the Fresnel field from the mask, L is the moire grating period, and λ is the reconstruction wavelength.

FLUX DIVERSION DUE TO MOIRÉ DIFFRACTION GRATING EFFECT FOR TWO OVERLAPPING ZONE PLATES

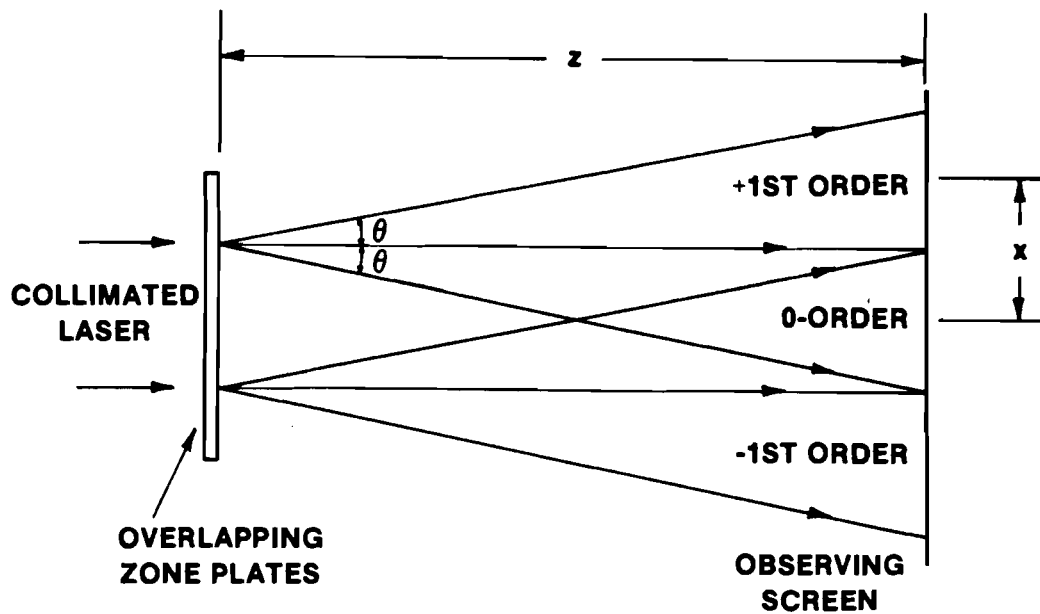


Figure 2.10

The third-order nonlinear artifact contribution just mentioned will be reduced in importance relative to the real image because of the C_j 's in equation [2.18]. Second order artifacts are stronger, but their importance must be measurable on the reconstruction bench if deterministic degradation is to be completely characterized. This topic is discussed in detail in Chapters III and IV, and methods for determining artifact importance are presented.

Only the moire effects for a two-point object have been discussed. For a multi-point object, the moire effects will compete for the available reconstruction flux just as the various point coded images will. Hence, diffraction efficiency into any one artifact point or displacement will vary strongly with object size. This topic is discussed in Section 2.4.5.3.

2.4.5.2 Phase Reconstructions

One of the drawbacks of ZPCI is the low diffraction efficiency of the Fresnel zone plate, which focusses only 10% of the flux from a collimated laser into the first order. The remaining flux is focussed in other real orders, diverged (as from virtual foci), or just passed through the system as d.c. flux. One way to increase diffraction efficiency is to convert the zone plate from an amplitude to a phase modulation device. Phase zone plates can be four times as efficient in focal irradiance as absorption zone plates. A coded image that is bleached (henceforth called a phase coded image) can be expected to have brighter images than an unbleached one, just as in holography.

Bleached holograms suffer from what is known as phase noise,⁽³⁵⁾

which is nonlinearity for phase transmittance. Phase noise is due to the self-interference of the object wave in the nonlinear terms of the t-E film function. Consider a hologram exposed as follows:

$$E(x) = |U_R(x) + U_O(x)|^2, \quad [2.24]$$

where $E(x)$, $U_R(x)$, and $U_O(x)$ are the hologram plane values of the total exposure and complex reference and object amplitudes, respectively. Assume the hologram is processed such that $t(x) = \exp[i\gamma E(x)]$, where γ is a proportionality constant. Expanding the exponential and grouping terms yields

$$\begin{aligned}
 t(x) &= 1 + i\gamma (|U_O|^2 + |U_R|^2) \\
 \text{d.c.} &\begin{cases} \nearrow \\ \rightarrow \\ \searrow \end{cases} \begin{aligned} & - \frac{1}{2} \gamma^2 \{(|U_O|^2 + |U_R|^2)^2 + 2|U_O|^2 |U_R|^2\} \\ & - \frac{1}{6} i\gamma^3 \{(|U_O|^2 + |U_R|^2)^3 + 6|U_O|^4 |U_R|^2 + 6|U_O|^2 |U_R|^4 + \dots\} \end{aligned} \\
 \text{image} &\begin{cases} \nearrow \\ \searrow \end{cases} \begin{aligned} & + U_O U_R^* \left(i\gamma - \gamma^2 |U_O|^2 - \gamma^2 |U_R|^2 - \frac{1}{2} \gamma^3 |U_O|^2 |U_R|^2 + \dots \right) \\ & + U_O^* U_R \left(i\gamma - \gamma^2 |U_O|^2 - \gamma^2 |U_R|^2 - \frac{1}{2} \gamma^3 |U_O|^2 |U_R|^2 + \dots \right) \end{aligned} \\
 \text{2nd order} &\begin{cases} \nearrow \\ \searrow \end{cases} \begin{aligned} & + U_O^2 U_R^{*2} \left(-\frac{\gamma^2}{2} - \frac{1}{2} \gamma^3 (|U_O|^2 + |U_R|^2) + \dots \right) \\ & + U_O^{*2} U_R^2 \left(-\frac{\gamma^2}{2} - \frac{1}{2} \gamma^3 (|U_O|^2 + |U_R|^2) + \dots \right) \end{aligned} \\
 \text{3rd order} &\begin{cases} \nearrow \\ \searrow \end{cases} \begin{aligned} & - \frac{1}{6} \gamma^3 U_O^3 U_R^{*3} + \dots \\ & - \frac{1}{6} \gamma^3 U_O^{*3} U_R^3 + \dots \end{aligned}
 \end{aligned} \quad [2.25]$$

Note that the first order images contain terms that have $|U_O|^2$ as a factor; the object structure will affect the image fidelity. A point object cannot suffer from phase noise. The SNR,⁽³⁶⁾ to second

order (neglecting $|U_R|^2$), for the primary image is

$$\text{SNR} = \frac{\gamma(i - |U_R|^2)}{-\gamma^2 |U_O|^2} = \frac{-i}{\langle \gamma |U_O|^2 \rangle} + \frac{K}{\gamma},$$

where $\langle \dots \rangle$ denotes spatial average and K is the beam balance ratio.

Call $E_T = |U_R|^2 + \langle |U_O|^2 \rangle$ the total average exposure. Then

$$\text{SNR} = \frac{1 + K}{\gamma E_T} + \frac{K}{\gamma}. \quad [2.26]$$

SNR increases with beam balance ratio K , but diffraction efficiency is high when K is small. Hence, phase holograms suffer intrinsically from noise.

According to definitions already established, the phase noise is not noise at all, but rather deterministic image degradation. This self-interference or intermodulation phenomenon occurs in all holograms for which t vs E is nonlinear. Thus, the gain in diffraction efficiency afforded by bleaching may be accompanied by a decrease in image fidelity.

The preceding statements can be extended to account for the case of ZPCI. The treatment proceeds as follows. The SEEH with t - E given by equation [2.16] is analyzed and shown to suffer no intermodulation distortion for certain cases. The extension to the MEEH provides a comparison with the generalized nonlinear absorption coded image and serves to further punctuate the concept of deterministic image degradation.

Consider the case for which $E(\underline{r}'')$ is the SEEH. Then

$$\begin{aligned} t_p(\underline{r}'') &= t_o \exp(i\phi) = t_o \exp(i\gamma E) \\ &= t_o \exp[2i\gamma C_1^2 (1 + 2\bar{g}_1)]. \end{aligned} \quad [2.27]$$

The optimum diffraction efficiency occurs for ϕ having a minimum value of zero and maximum of π . Since $E_{\max} = 4C_1^2$, then $\gamma = \pi/4C_1^2$. For $C_1 = \frac{1}{2}$, $\gamma = \pi$, and

$$t_p = t_o \exp\left(\frac{i\pi}{2}\right) \exp(i\pi\bar{g}_1). \quad [2.28]$$

The previously mentioned properties of \bar{g} can be used with algebraic manipulation to yield

$$t_p = 2t_o\bar{g}_1. \quad [2.29]$$

Recall the expression for the optimum absorption SEEH:

$$t_a = t_o \left[\frac{1}{2} + \bar{g}_1 \right]. \quad [2.30]$$

The phase transmittance function of [2.29] diffracts all the transmitted light into the image orders, while the absorption function diffracts only half the amplitude into the image. Hence, four times as much signal flux is available in the phase case as in the absorption case.

The ideal SEEH contains an object with an infinite number of points. It is easy to see, though, that $|u_o|^2$ is a constant for the SEEH, rendering it free of intermodulation degradation. This fact is independent of the nonlinearity, and it leads to an interesting concept: if a coded image (be it hologram or otherwise) has a binary exposure distribution, it can be processed free of intermodulation distortion. The SEEH example illustrates the power of spatially redundant information storage: a large number of object points can be encoded into only two gray levels.

The case of phase reconstruction can be extended to complex objects by considering again that the exposure function at the film in the recording step is given by equation [2.10]:

$$E = \sum_{j=1}^N E_j = \sum_j 4C_j^2 \left(\frac{1}{2} + \bar{g}_j \right). \quad [2.10]$$

The t-E function can be written for phase transmittance as

$$t_p = t_o \exp \left(i\gamma \sum_j 4C_j^2 \left(\frac{1}{2} + \bar{g}_j \right) \right). \quad [2.31]$$

This can be rewritten for the case of optimum use of the phase transmittance by letting the maximum phase be π , the minimum zero.

Then

$$\gamma = \frac{\pi}{\sum_j 4C_j^2} \quad [2.32]$$

$$\text{and} \quad t_p = t_o \sum_{k=0}^{\infty} \left((i\gamma)^k \sum_{k_j} \frac{E_1^{k_1} E_2^{k_2} \dots E_N^{k_N}}{k_1! k_2! \dots k_N!} \right), \quad [2.33]$$

where the definitions following equation [2.18] hold. Equation [2.33] is the phase transmittance for a general object of N points. Eqs. [2.18] and [2.33] are identical except that alternate terms of [2.33] change phase due to the presence of the i in the sum over k. If σ in equation [2.18] is made complex, then [2.18] describes both phase and amplitude transmittance. As in [2.18], for each k in [2.33], \sum_{k_j} has N^k terms, N of which have the form $(E_j)^k/k!$ and are image terms.

The primary image term for $k = 1$ is

$$t_p|_{k=1} = 4t_o i\gamma \sum_j C_j^2 \left(\frac{1}{2} + \bar{g}_j \right). \quad [2.34a]$$

The primary image term for all k is

$$t_p|_{\text{primary}} = t_o \sum_{k=1}^{\infty} \frac{(i\pi)^k}{\left(\sum_{j'} 4C_{j'}^2 \right)^k k!} \sum_{j=1}^N C_j^{2k} \left(\frac{1}{2} + \bar{g}_j \right). \quad [2.34b]$$

The image contribution from the nonlinear terms is complicated by

the phase relationships between the various terms. The image field has real and imaginary components, complicating the irradiance distribution, and phase effects cause problems similar to those in the image expression of equation [2.20c]. These effects can degrade the image by lowering its amplitude. All previous statements concerning artifacts apply here as well.

The flux transmittance of the bleached coded image is always higher than that of the unbleached one. Hence, the phase reconstruction will yield a brighter image than the absorption one, with the attendant deterministic image degradation of commensurate importance. If the formation of artifacts is the strongest image degradation for the absorption case, bleaching will provide no gain in image fidelity. However, if the dominant degradation mechanism is one that does not increase with total flux transmittance of the reconstruction mask, then bleaching can increase image fidelity over a nonlinear absorption coded image. If the absorption mask is linearly recorded, the effect of bleaching depends on the information content of the object, which will now be addressed.

2.4.5.3 Artifact Formation

Only one- and two-point objects have been considered so far. Larger objects can be studied by rewriting equation [2.17] as

$$t = \sum_{k=0}^{\infty} \alpha_k k! \sum_{k_j} \frac{E_1^{k_1} E_2^{k_2} \dots E_N^{k_N}}{k_1! k_2! \dots k_N!}, \quad [2.17a]$$

where the notation is that following equation [2.18a]. Let all N object points have equal strength. For any k , \sum_{k_j} has N^k terms, where $E_j^{k_j}$ is considered a single term. Assume the optimum transmittance

modulation is always achieved; the transmittance available for an arbitrary intermodulation order in the t-E polynomial is constant. The amplitude is divided equally among N^k terms, and the relative diffraction efficiency for a k^{th} order point is $\alpha_k^2 N^{-2k} / 2^{2k}$.

For $N = 1$ (the image), the relative efficiency of imaging due to a point is $\alpha_1^2 / 4N^2$, and the total relative image flux is $\alpha_1^2 / 4N$. The relative flux into the k^{th} order is $\alpha_k^2 N^{-k} 2^{-2k}$. Hence, artifact efficiencies decrease more quickly with increasing object size than does image efficiency. The ratio of image efficiency to k^{th} order artifact efficiency is

$$\frac{\eta_1}{\eta_k} = 2^{2k-2} \frac{\alpha_1^2 N^{-1}}{\alpha_k^2 N^{-k}} = 2^{2k-2} N^{k-1} \left(\frac{\alpha_1}{\alpha_k} \right)^2.$$

In Section 3.4.1, the α_k for Kodak RAR 2491 film, a standard x-ray detector in laser fusion, are found to be $\alpha_0 = 0.92$, $\alpha_1 = 0.243$, $\alpha_2 = 0.0475$, and $\alpha_3 = 0.0035$ (these values are only valid under certain specified conditions and should not be considered useful otherwise). Even for a two-point object, $\eta_1 / \eta_2 > 200$.

Let $\Delta\eta_k$ be the efficiency of a single point in the k^{th} nonlinear order. If all points are not the same strength, $\Delta\eta_1 / \Delta\eta_k$ can be small. Suppose that for a two-point object, one point emits 91% of the total source flux. One $k=2$ artifact is about 80% as strong as the weaker of the two image points. This result can be extended to larger objects; marked contours in an object result in peaks in the intermodulation distortion which can produce significant degradation. In an extended object, a grainy appearance might be observed as a

result of intermodulation effects.

2.4.5.4 Comments on the Feasibility of Quantitative Nonlinear ZPCI

The preceding comments point to a potentially interesting issue. If the odd orders of reconstruction contain images and correlation degradations, and the even orders contain only correlation effects, then it might be possible to quantify the deterministic image degradation by comparing the irradiances for the various reconstructed orders. Such a scheme would involve some assumptions about the object size and radiance. From equations [2.18] and [2.18a], it can be seen that the second order of reconstruction will contain even-number-point correlations of all values up to the number of object points. In general, then, it is not possible to identify a reconstruction field with a single order of correlation. The problem is complicated by the fact that there can be many orders of nonlinearity in the recording detector response (the sum over the k_j 's in [2.18]).

For any object larger than a few resolution cells, the quantitative interpretation of artifacts is not feasible, i.e. it is not easy to calculate a particular odd-point correlation from a knowledge of the irradiance distribution in an even reconstructed order. However, information about the cumulative even order correlation effect is contained in the even orders. For any object consisting of more than a few resolution cells, the odd and even order artifact contributions can be easily associated. For a broad, diffuse object, the even and odd order correlations are very similar, and it might appear feasible to use this fact in developing confidence levels in the image. For example, perhaps the even order irradiance could be subtracted from

the odd order irradiance to yield a "loyal" image. In principle, this could be done. For objects consisting of discrete points, the interpretation is very complex, as already stated. The amount of work devoted to developing a computer program to reduce the data could be more appropriately applied to developing a program that would digitally reconstruct the original coded image; such a program would have the added advantage of being quantitative.

Matters become even more complicated when imperfect shadowcasting in the recording step is considered. Fresnel diffraction of x-rays by the zone plate aperture and partial transmission of radiation through zone edges cause apodization of the zones, resulting in a redistribution of the Fourier coefficients describing the zone plate. Hence, even for linear recording, there will be even order images. It is even possible that some even orders might be stronger than adjacent odd orders, or that some odd orders might be missing, as in diffraction gratings in which the ratio of slit spacing to slit width has special values. In fact, the Fresnel zone plate has such missing orders (all the even ones). The redistribution of coefficients casts serious doubt that correlation effects can be measured. Gur studied diffraction in the recording step and developed criteria for shadow sharpness; interested readers are referred to his work for details.⁽¹⁵⁾

Since quantitative analysis of deterministic image degradation is such a cloudy issue, it is hardly surprising that ZPCI is not used for obtaining quantitative information. In fact, ZPCI cannot be considered viable unless rules are developed that indicate the image fidelity that can be obtained in a given situation. This matter

is addressed later as part of a general view of information throughput in ZPCI.

This concludes the discussion of nonlinear ZPCI. The salient features are:

- (1) The coherent nature of the reconstruction step can cause image distortion in even linear ZPCI.
- (2) Artifacts are deterministic and are therefore information. In principle, artifacts can be used to gain knowledge about the object because of this deterministic property.
- (3) Imperfect shadowing of the zone plate mask in the recording step, either by Fresnel diffraction or partial transmission through zone edges, causes a redistribution of the Fourier coefficients of the zone plate. This redistribution destroys the exclusive nature of the focussing of artifacts and images, rendering point (2) above useless in practice.
- (4) The dominant artifact is second-order and is manifest as either focussed or non-focussed radiation. Proper implementation of ZPCI entails some way to estimate second-order degradation.
- (5) For x-ray films, in which the D vs E function is approximately linear, the phase reconstruction is about as nonlinear as the amplitude reconstruction, though certain phase effects can complicate the phase case more than the amplitude case. Thus, when the dominant degradation is deterministic, phase reconstructions might not further affect image fidelity.
- (6) Whereas the flux diffraction efficiency into a single image point varies as $1/N^2$, where N is the number of object cells, artifact

diffraction efficiencies vary as $1/N^{2k}$, where k is the order of non-linearity. Hence, nonlinear reconstructions are more loyal for large objects than for small ones. The effect of nonlinearity is to create a grainy appearance in large images and discrete artifact points in small, discrete images.

The practical ramifications of nonlinear ZPCI will be addressed in the experimental chapter, and methods for estimating the importance of deterministic image degradation will be presented in the chapter on optimization.

2.4.6 Noise

Noise in ZPCI causes random fluctuations in the complex amplitude transmittance function of the reconstruction mask, resulting in image degradation. These fluctuations arise from shot noise (due to the quantum nature of the source radiation in the recording step), emulsion thickness variations, and grain noise. Ceglio⁽¹¹⁾ treated shot noise. Gur⁽¹⁵⁾ treated zone plate edge serration in the recording step as noise, but high quality zone plates can be easily fabricated (see Appendix II), so edge serration is unimportant. Emulsion thickness variations are affected by the recording exposure and are not really noise; however, the spatial frequency response of emulsion relief is variable and results in a nonuniform flux contribution to the image. Emulsion relief effects can be mitigated by the use of a liquid gate with the mask, as will be shown in the experimental chapter.

Grain noise was addressed by Gur,⁽¹⁵⁾ but his treatment was

sketchy. The treatment here proceeds along the following lines. First, the underlying physical mechanisms of grain noise are briefly described. Then the functional form of grain noise is introduced. The resulting noise expression is discussed, taking into account real grain noise spectra of films. Finally, shot noise is shown to be of the same functional form as grain noise and is incorporated into the treatment.

2.4.6.1 Grain Noise Mechanisms

Grain noise has two distinct causes, grain distribution fluctuations and the scattering properties of grains. Grain distribution is affected by several factors, including the original (undeveloped) grain distribution, grain size and sensitivity ranges, and the statistical imperatives of the exposure/development process.⁽³⁹⁾ The literature contains debate about grain distribution, and the reader is referred to reference 30 for details. The scattering properties of grains are complex, and the attempt will be made here to illustrate the complexity.

The developed grain is a mass of silver, the structure of which can vary from compact and spherical to extended and fibrous. Size can range from a few tens of nanometers in diameter to about a micron, with the latter size corresponding to a coarse-grained film. Light scattering by small particles has been extensively studied,⁽⁴⁰⁾ but typically the particles are assumed to be ideal with respect to size, shape, and optical properties; the Mie scattering theory becomes extremely complicated for real photographic grains. This problem is further complicated when the emulsion in the immediate vicinity of

the grain is considered. Development of silver halide emulsions involves the chemical reduction of silver halide, and along with this development is the evolution of oxidation products which can cause crosslinking of gelatin molecules in the vicinity of the individual grains. Crosslinking hardens the gelatin, essentially locking into place the mechanical state of the emulsion, which might typically be swollen from its undeveloped state. The exact properties of the hard gelatin shell surrounding a grain will depend on the properties of the developer, gelatin, and grain, such as activity and diffusion lifetime of the oxidation products.⁽⁴¹⁾ Hence, the actual scatterer is the silver grain surrounded by a complicated dielectric medium.

Bleaching can cause more complication of the issues because bleaches change not only the chemical and physical properties of the grain, but of the surrounding gelatin as well.⁽⁴²⁾ Various bleaches are touted as being superior by some authors, yet are poorly viewed by others. In this present work, the major grain noise contribution was found to occur in a film of coarse grain size, while the bleaching method used was not found to introduce an increase in scattering of the fine-grained emulsion used. Hence, bleached emulsions were found to have less grain noise (relative to signal levels) than unbleached ones. The complicated scattering properties of the grain embedded in a gelatin shell is not the whole of the problem, however. The multitude of grains in the emulsion warrant the treatment of the problem as one of multiple scattering. It should be appreciated that the scattering properties of the emulsion are complex and that their functional form might be measured but not necessarily calculated from first principles.

2.4.6.2 Mathematical Formulation of Noise

Studies of grain noise in holography^(43,44) have assumed that the noise is additive, i.e.

$$\tau(\underline{r}'') = t(\underline{r}'') + \tau'(\underline{r}''), \quad [2.35]$$

where $\tau(\underline{r}'')$ is the hologram amplitude transmittance, $t(\underline{r}'')$ is the deterministic transmittance, and $\tau'(\underline{r}'')$ is the noise transmittance. Numerous studies of film scatter⁽⁴⁵⁻⁴⁷⁾ have found scattered intensity to increase linearly with optical density of the film. Thus, $\langle \tau'(\underline{r}'') \rangle$ depends upon $t(\underline{r}'')$. $t(\underline{r}'')$ is usually taken to be relatively constant, simplifying the expression for $\tau'(\underline{r}'')$. In ZPCI, $t(\underline{r}'')$ cannot be assumed constant, so the explicit dependence of $\langle \tau'(\underline{r}'') \rangle$ on $t(\underline{r}'')$ must be maintained.

The scattered light due to emulsion granularity exhibits a non-uniform spatial frequency spectrum. Brandt⁽⁴⁶⁾ has measured noise power spectra in the range of interest in ZPCI (<20 cycles/mm) and has found the noise power spectrum for Kodak Pan X film to be given by

$$I(\xi) \approx \frac{\alpha' I_0}{\xi^2}, \quad [2.36]$$

where $I(\xi)$ is the power scattered into unit spatial frequency at frequency ξ , I_0 is the incident power, and α' is a density-dependent parameter. The Pan X study is singled out here because Pan X closely matches the properties of RAR 2490 film, which is used in the experiments for our work. For Pan X, $\alpha' \approx 8 \cdot 10^{-4}$ (cycles/mm)² for a diffuse density of 1.0.

$\tau'(\underline{r}'')$ must include both the density variation effects and the spatial frequency effects of the noise transmittance. Since

scattered intensity is linearly related to optical density of the film, $\langle \tau'(\underline{r}''') \rangle$ is not linearly related to $t(\underline{r}'')$. However, a linear dependence can be assumed if the transmittance variation attributed to any radiating object cell is small. The spatial frequency effect can be incorporated by noticing that for a uniformly exposed and developed film, the scattered noise is a convolution of $I(\xi)$ in equation [2.36] with a delta function. It is then reasonable to assume that the noise transmittance is the product of some function of the deterministic transmittance and the transform of $1/\xi$ (call this transform $\tilde{\xi}$). Since $\langle \tau'(\underline{r}''') \rangle$ is linear with $t(\underline{r}'')$, then

$$\tau'(\underline{r}''') = t(\underline{r}'') \tilde{\xi} \tau'_0(\underline{r}''), \quad [2.37]$$

where $\tau'_0(\underline{r}'')$ is a random function. Thus,

$$\tau(\underline{r}'') = t(\underline{r}'') [1 + \tilde{\xi} \tau'_0(\underline{r}'')]. \quad [2.38]$$

The reconstruction step is a Fresnel transformation of $\tau(\underline{r}'')$. The noise amplitude in the image plane is the convolution of the deterministic image amplitude and the speckle pattern that is the Fresnel transform of $\tau'_0(\underline{r}'')$. For linear ZPCI, the transmittance of equation [2.11] can be combined with equation [2.37] to yield a resultant noise amplitude in the image field of

$$\begin{aligned} F_r \{ \tau'(\underline{r}''') \} &= \sum_{j=1}^N F_r \{ \tau'_0(\underline{r}'') \tilde{\xi} 4C_j^2 \left(\frac{1}{2} + \bar{g}_j \right) \} \\ &= \sum_{j=1}^N \left[F_r \{ \tau'_0(\underline{r}'') \tilde{\xi} \} * F_r \{ 4C_j^2 \left(\frac{1}{2} + \bar{g}_j \right) \} \right], \quad [2.39] \end{aligned}$$

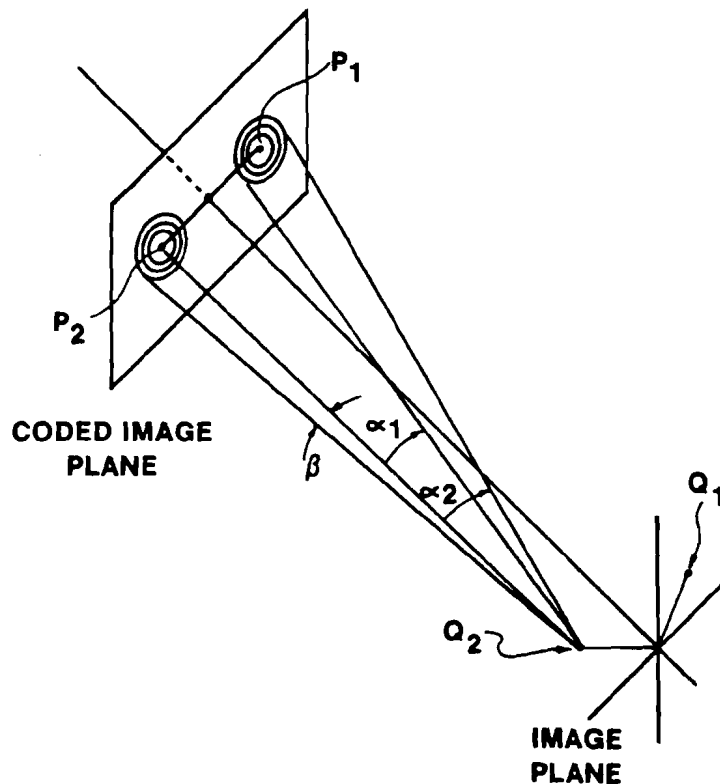
where F_r denotes Fresnel transform. The noise in the image plane is just the sum of noise contributions from all the SEEH's. The contribution from each SEEH is just the convolution of the deterministic

transmittance and the scattering from $\tilde{\xi} \tau'_0(\underline{r}'')$. For nonlinear ZPCI, equation [2.39] becomes algebraically more challenging, but the results are similar.

The equivalent multiple exposure hologram is a sum of Fresnel holograms, so the grain noise must be treated as such. The image is in the far field of the individual grains, so Fresnel hologram grain noise can be treated much as the noise in Fourier transform holograms (see reference 31, p. 354). However, the noise at any point in the Fresnel field is a result of flux contributions from a range of spatial frequencies. Usually, an average spatial frequency can be chosen for each point, and the noise power at that frequency can be used to define the noise power at the point of interest. In ZPCI, the noise from each SEEH is centered on the axis of that SEEH. All SEEH's exhibit identical noise power spectra (each with respect to its own axis). The noise at any image field point is the resultant of the noise contributions from all the SEEH's, with each SEEH adding noise from a range of frequencies centered on its axis. Figure 2.11 illustrates this concept.

Ceglio⁽¹¹⁾ determined noise to be insignificant by introducing the concept of information compression, in which the noise uniformly covers the image field, while the information is focussed to a small image, resulting in a high ratio of image-to-noise amplitude. This view of information compression is oversimplified because it assumes that the noise uniformly covers the image field; equation [2.39] indicates that the noise is peaked at the image due to the presence of $t(\underline{r}'')$ in the noise transmittance expression. In fact, equation

SPATIAL FREQUENCY OF GRAIN NOISE IN ZONE PLATE CODED IMAGING



The zone plate centered at P_2 reconstructs an image point at Q_2 . The zone plate centered at P_1 focuses at Q_1 . The maximum and minimum spatial frequencies of the noise at Q_2 due to the zone plate at P_1 are defined by the angles α_1 and α_2 , while the noise at Q_2 due to the zone plate at P_2 is contributed from spatial frequencies beginning at d.c. and extending to a cutoff defined by angle β .

Figure 2.11

[2.39] leads to the result that the diffraction patterns of the defocussed images in any image plane (which are just rings surrounding the image) will appear granular due to the grain noise.

Due to the assumption that the object is of limited extent, the noise will vary slowly over the extent of the image because the angular subtense of the image at the coded image mask is small. Thus, the average noise irradiance may be considered to be constant at the image (for a given object size) regardless of object shape. This assumption is least secure for objects consisting of a few discrete points separated by large distances (say, the inner zone diameter).

The above arguments lead to the result that the average noise power \bar{I}_N is just the frequency-averaged noise introduced by the emulsion. Denote I_N as the noise power scattered into a point in the image plane and $I(\xi_0)$ as the noise power at frequency ξ_0 , with ξ_0 being the average frequency of the image. Then

$$I_N = \frac{I(\xi_0)}{\lambda^2 d^2}, \quad [2.40]$$

where d is the reconstruction distance and λ is the reconstruction wavelength. For Pan X, $10^{-4} I_0 \leq I(\xi_0) \leq 2 \cdot 10^{-3} I_0$, where I_0 is the incident power and ξ_0 varies from 2 to 25 cycles/mm (this is for a density of 1.0). For $d = 300$ cm and $\lambda = 0.633 \mu\text{m}$, $\bar{I}_N \approx 5 \cdot 10^{-4} I_0$. From equation [2.39], it is readily deduced that the noise irradiance varies as $1/N^2$, where N is the number of object cells. For ten object cells, then,

$$\bar{I}_N \approx 5 \cdot 10^{-6} I_0. \quad [2.41]$$

The signal power can be considered as well. First order

receives 0.1% of the total flux. Following Goodman,⁽⁴³⁾ we can write

$$\text{SNR} = \frac{I_i}{I_N} \left(1 + \frac{2I_i}{I_N} \right)^{-\frac{1}{2}} . \quad [2.42]$$

Hence, for Pan X and ten object cells, $\text{SNR} \approx 10$. For bleached emulsions, I_i is about four times greater than for unbleached emulsions, so SNR would increase to 20. The preceding remarks indicate the need for a fine-grain film in ZPCI. Unfortunately, ZPCI is often used when too little flux is available for pinhole cameras to be viable, so a sensitive, coarse-grain film is often chosen.

Spatial shot noise due to the quantum nature of the source radiation is important in ZPCI. This discussion will enhance the findings of earlier shot noise studies^(5,11) by pointing out the similarities and differences between shot noise and grain noise.

Shot noise is generally considered to be affected by two major factors, flux emitted per source information element and zone plate aperture size. The more flux emitted per resolution cell, the lower the shot noise. Grain noise is not a function of source strength. On the other hand, the zone plate aperture size affects both grain noise and shot noise. For constant resolution, increasing the aperture size decreases shot noise because more flux is collected per resolution element. But grain noise increases with increasing aperture size because noise irradiance is increased. Signal power increases exactly as grain noise power with increasing aperture size, so $\text{SNR}_{\text{grain}}$ does not change with aperture size. However, SNR_{shot} increases with increasing aperture size.

Previous treatments of shot noise implicitly assume a relatively constant exposure and consider deterministic transmittance variations

to affect only signal levels. In fact, shot noise is affected by these variations much as grain noise is (equation [2.37]). The random transmittance variation is a function of the transmittance. Thus, as stated earlier, information compression is valid only in a somewhat more complex form than its original construction.

Shot noise also has a different spatial frequency content than grain noise. Grain noise power varies inversely with the square of the spatial frequency, whereas shot noise should be uniform for all spatial frequencies below some cutoff value. The cutoff value is undoubtedly related to the detector area affected by exposure to one quantum of radiation, whether the quantum is a particle or a photon.

2.5 Information and Optimization

This section is a short consolidation of the ideas already developed. Within the framework of information, it poses problems that will be addressed in the chapters on experimentation and optimization.

In conventional information theory, the concept of information capacity refers to the maximum amount of information a channel can transfer. Noise is random degradation of the information and lowers the fidelity of the transfer process. In principle, the encoding and decoding processes can be performed in a manner such that the error in transmission is arbitrarily small.⁽⁴⁹⁾ In ZPCI, this amounts to reducing shot and grain noise. Yet it was shown earlier that the coherent decoding process requires an encoding step that may leave some information "scrambled" and effectively lost. The amount of lost information is dependent upon the degree of nonlinearity.

In order to fully exploit ZPCI, the user must establish some figure(s) of merit describing system behavior. This is difficult for ZPCI because both random and deterministic degradation depend upon object information content, i.e. on object size and contour geometry. Thus, using a priori information about the object, the user can "tune" the system by varying total information capacity (zone plate parameters), deterministic degradation (linearity), and random degradation (detectors). In addition, the decoding process should include some means of verifying image fidelity. Direct measurement of quantities such as SNR would be ideal.

Clearly, optimization is a multi-step process. First, the system must be tuned to optimize certain (as yet undetermined) figure(s) of merit that relate to image fidelity. Secondly, the system output must be analyzed to determine real image fidelity. It is advantageous to optimize in the first step what is measured in the second. The next chapter will illustrate concepts set forth in this chapter, while the chapter on optimization will expand the ideas of this section into general guidelines for successful use of ZPCI.

CHAPTER III

EXPERIMENTAL INVESTIGATIONS

3.1 Introduction

The results of Chapter II indicate that ZPCI must be applied with discretion. The purpose of this chapter is to experimentally verify the results of Chapter II while shedding more light on the problem of optimization by showing what can be achieved with ZPCI in practice.

The chapter begins with a description of the devices used for encoding and decoding information. Then a short discourse concerning the various possible figures of merit will serve to introduce the experiments performed. A comparison of linear and nonlinear ZPCI is presented, with emphasis placed on the roles of object information content and severity of nonlinearity. Then noise is studied as a function of both diffraction efficiency of the reconstruction mask and object size. Finally, the experiments are summarized in order to fit them into the optimization scheme that is the subject of Chapter IV.

3.2 Image Evaluation Devices

This section is a description of the apparatus used to perform the experiments in ZPCI. A system that allows encoding of emissions from predetermined objects is first discussed. Then the reconstruction bench is described.

3.2.1 X-Ray Exposure System

All exposures were performed by using a diffuse x-ray source to backlight (through a beryllium foil) a metal foil complement of the object of interest (Figure 3.1). For example, a uniform disk object

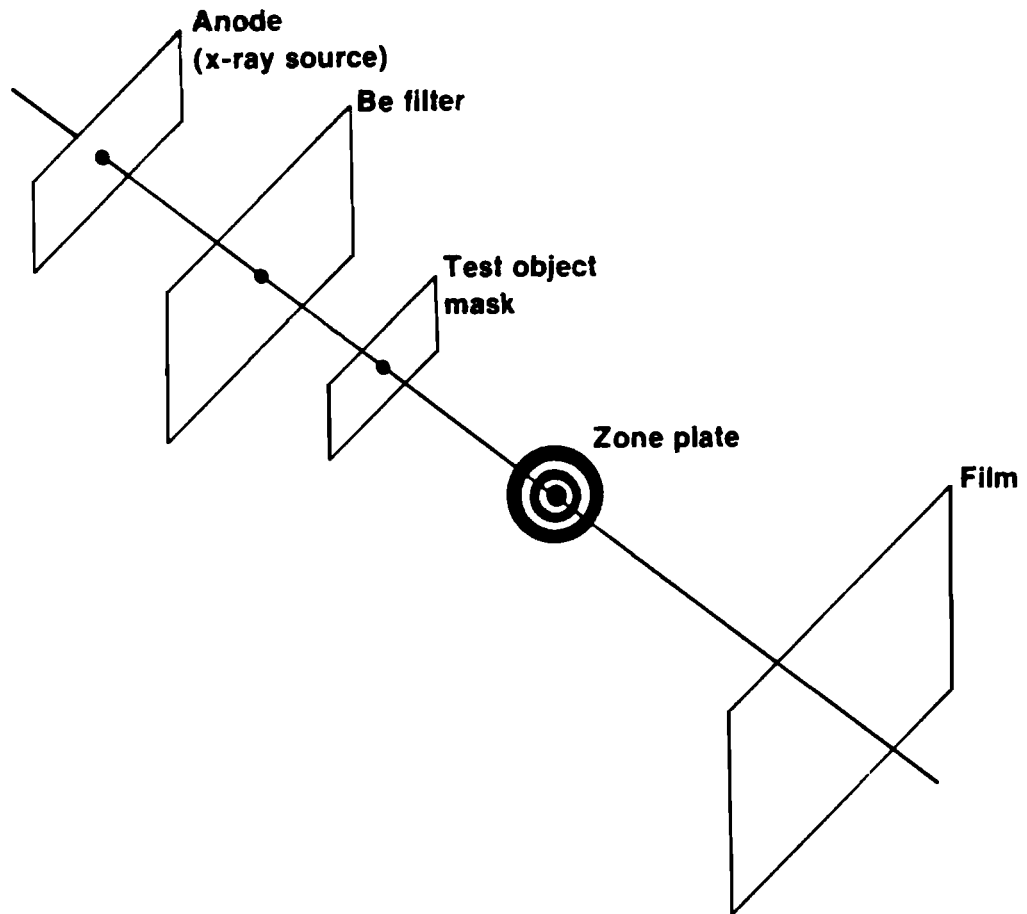


Figure 3.1 Exposure System Schematic

X203

of diameter d can be simulated by backlighting a gold foil in which there is a hole of diameter d . The object then shadows a Fresnel zone plate onto film.

The x-ray source employed is known as a Henke tube, after its inventor.⁽⁵⁰⁾ Electrons from a heated filament are accelerated into an anode of several square centimeters area, creating a broad source of x-rays. The anode material determines the photon energy. All the experiments described here used a titanium anode, and the accelerating voltage was varied to change the relative strength of the various emission lines (see Section 3.4.1).

The exposure apparatus was operated in a vacuum chamber at 10^{-6} to 10^{-7} torr pressure. The Be filter served to eliminate x-rays soft enough to be significantly diffracted by the zone plate while providing a light tight environment for the film. Exposure times varied from one minute to 26 hours; lack of relative motion between object mask, zone plate, and film was maintained by mounting all three on rings which were press-fitted into a brass tube (Figure 3.2). Hence, system geometry could be easily varied.

3.2.2 Optical Reconstruction Bench

The reconstruction bench is shown in Figure 3.3. A He-Ne laser is focussed by a 20x microscope objective and spatially filtered by a $15\ \mu\text{m}$ pinhole. The filtered beam is collimated by a 31.8 cm focal length lens of variable aperture ($f/9 - f/22$). The collimated beam transilluminates the reconstruction mask, which is positioned at the front focal plane of the relay lens. The relay lens is identical to the collimator and relays virtual images into the real image field.

X-RAY EXPOSURE SYSTEM CROSS-SECTION

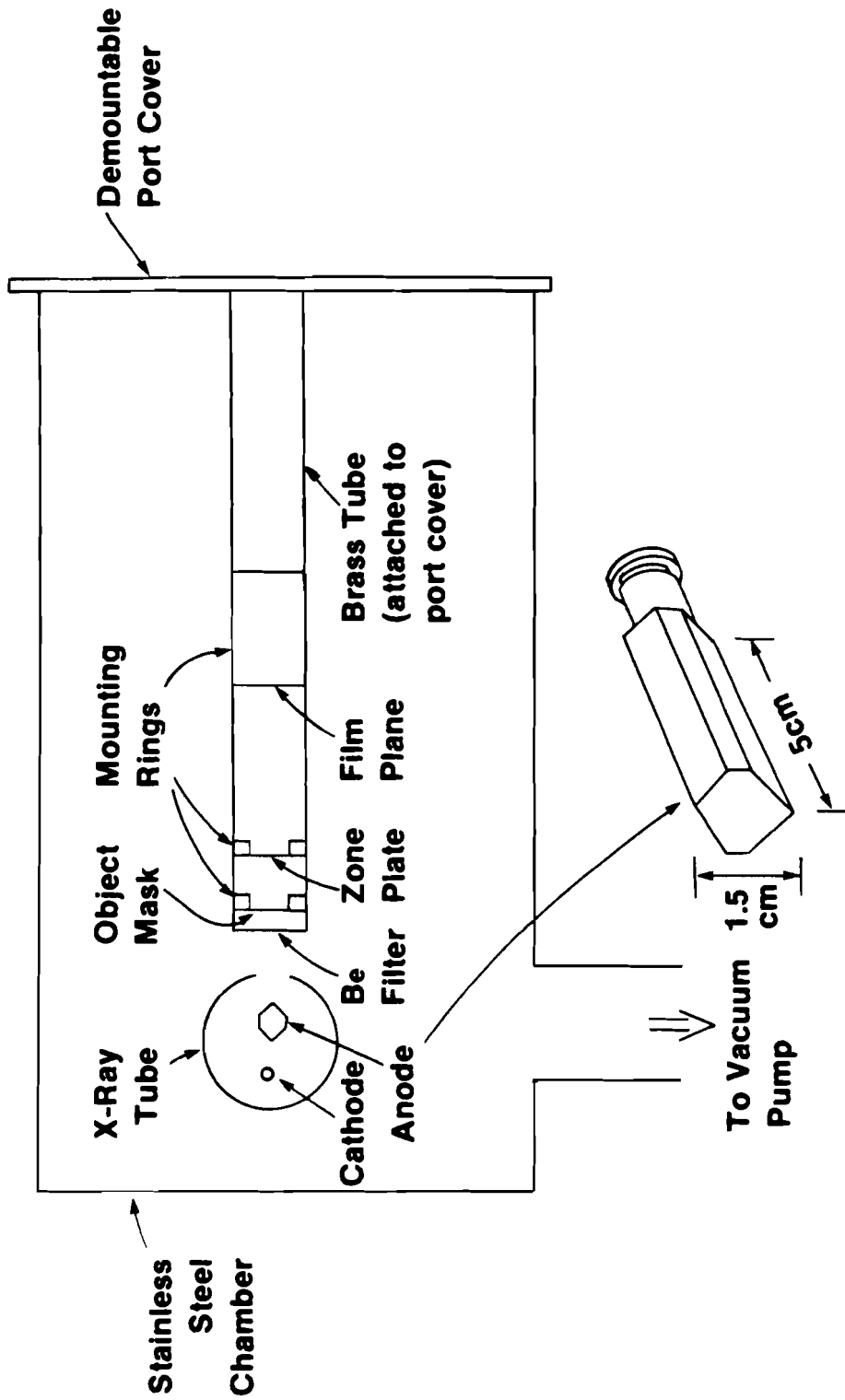


Figure 3.2

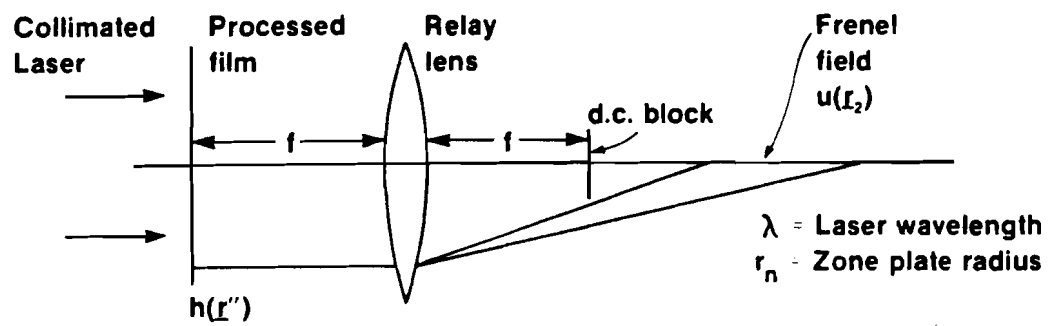


Figure 3.3 Optical Reconstruction Bench

X120

The rear focal plane of the relay lens contains a 100 μm diameter circular aluminum disk mounted on a thin glass stalk of 5 μm diameter. The disk can be positioned to block the (focussed) d.c. light. This plane is also the Fourier transform plane of the reconstruction mask.

Since the reconstructed images fall at distances which lie at integral fractions of the primary focal length from the reconstruction mask, the relayed images lie at integral multiples of the conjugate of the primary focal length. For example, for a relay lens of focal length 31.8 cm and a (virtual) primary reconstructed focal length of 300 cm, by Newton's law the relayed (and now real) conjugate image lies a distance $f_1' = f_{\text{lens}}^2 / f_1 = 3.37$ cm behind the rear focal plane of the relay lens. The p^{th} order is reconstructed a distance f_1 / p from the mask, so the p^{th} order relayed conjugate image lies a distance $f_p' = pf_1'$ behind the rear focal plane. This property allows easy location of the various orders if the exact geometry of the encoding system is known. A disadvantage is the variation of magnification with order number; care must be taken to avoid demagnifying beyond the resolution of the relay lens.

The reconstructed images can be viewed with a microscope or photographed with a microscope-camera combination. In addition, a pinhole-photodiode combination can scan the magnified image to provide irradiance information.

3.3 Discussion of Validity of Various Figures of Merit

Optimization of any imaging system requires evaluation methods. The methods traditionally used for evaluating direct imaging systems are not always effective in characterizing coded imaging systems.

This section is a discussion of MTF, impulse response, and edge response, and the role of each in ZPCI system evaluation. Experiments are suggested which illustrate the inconclusive nature of evaluations using these criteria and suggest, as in Chapter II, the value of concepts such as information.

MTF exemplifies the difficulty in applying standard methods in evaluating ZPCI. Technically, ZPCI is not a linear incoherent system, so MTF cannot be used for evaluation. But even if the image complex amplitude could be measured, the concept of contrast transfer is inadequate because of the role of object information content in system performance. Object size determines image irradiance as pointed out in Chapter II, so the absolute image modulation at a given spatial frequency will vary with object size. Clearly, use of MTF could lead to erroneous results in evaluation studies.

Impulse response can lead to incomplete results. Absolute irradiance of a single image point will vary with the information that occupies the remainder of the image field, even though the irradiance distribution around the point remains qualitatively the same. In a similar manner, edge response does not provide complete information. If nonlinear ZPCI is used, the situation is even more complicated. For example, the image of a point object provides little information about the image of a two-point object.

The root of the failure of the traditional evaluation methods is simple: only a certain amount of amplitude (or phase) modulation is available in the reconstruction mask, and this modulation is divided among the various image and artifact cells in a way that

depends upon object information content and system linearity. Some comparison of the useful image information content (not artifacts) with object information content would yield an "information fidelity fraction" which could be helpful. A measure of SNR is necessary as well; this must account for the decreasing diffraction efficiency in the mask associated with increasing object information content. Thus, parameters such as resolution and contrast transfer have meaning in ZPCI, but only within the more general framework of information and noise.

To illustrate the elusive nature of ZPCI characterization, it is only necessary to measure some simple parameter, such as image spot energy distribution, for two different objects. Though in relative terms the parameter may be the same for the two objects, the SNR would in fact be quite different. Measurements in the experiments to follow will confirm this assertion.

3.4 Studies of Nonlinear ZPCI

This section explores nonlinear ZPCI with concentration on two themes. After an explanation of the method used to vary linearity, a comparison of linear and nonlinear imaging is presented for a small object with marked contours. Then the role of object size in nonlinear ZPCI is illustrated.

3.4.1 Film Calibration

As mentioned in Section 2.4.4, the soft x-ray response of photographic emulsions is complicated; the t-E behavior for mono-energetic x-ray exposures is nonlinear. Also, knowledge of the t-E

behavior at several different x-ray energies does not allow one to predict the t-E behavior for an exposure consisting of some known mixture of those energies.⁽²⁶⁾ In other words, adding the densities contributed by the "component" exposures will not yield the final density that is observed. For a given energy spectrum, a complete film calibration must be performed; considerably more work is necessary than for visible light calibrations, in which addition of densities due to component exposures is valid.

The exposure system in Section 3.2.1 emits very "pure" spectra with proper loading of the anode.⁽⁵⁰⁾ Spectra with greater than 90% of the total energy in the K_{α} lines are achievable. Experiments were performed with a Ti anode (K_{α} lines at 4.5 keV) and various currents and accelerating voltages. It was discovered that RAR 2491 film exhibited t-E behavior with linearity dependent upon acceleration voltage (see Figure 3.4). At an anode voltage of 9 keV, the t-E behavior was nonlinear, while linearity was achieved at 7 keV for an optical density less than 1.0. A crude third-order approximation to the 9 keV curve in Figure 3.4 is

$$t = 0.9 - 0.2433 E + 0.0475 E^2 - 0.0035 E^3, \quad [3.1]$$

where E is in the relative scale of the figure. The linear relation is given by

$$t = 0.9 - 0.095 E. \quad [3.2]$$

Appendix I describes film processing and measurement essentials.

Figure 3.4 indicates that a controlled study of nonlinearity is possible. The next two sections are presentations of such work.

**CALIBRATION OF RAR 2491 FILM FOR
X-RAYS EXCITED AT TWO VOLTAGES
IN TITANIUM ANODE HENKE
TUBE SOURCE**

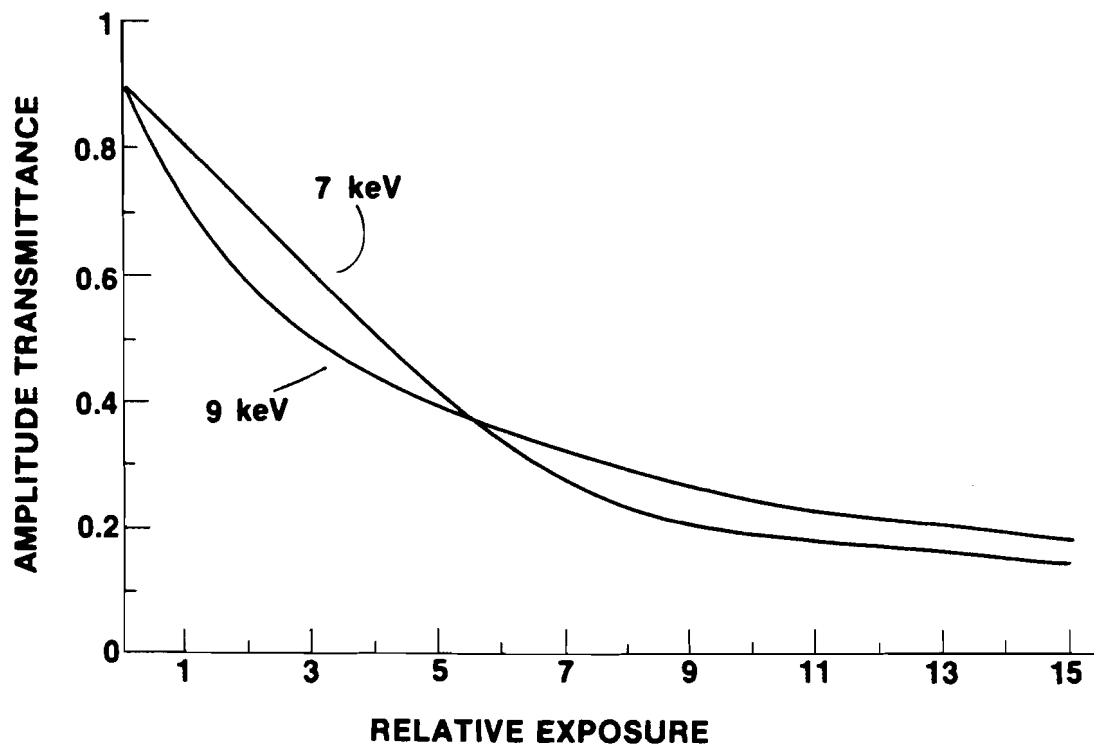


Figure 3.4

3.4.2 Variation of Image Fidelity with Nonlinearity

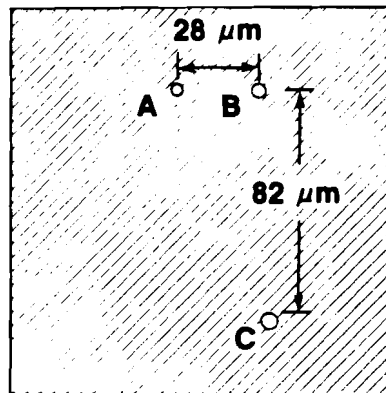
In this section, the results of Section 3.4.1 are used to compare linear and nonlinear ZPCI. Image fidelity is investigated for a known object which is imaged with three types of t-E curves: linear, nonlinear absorption, and phase. A simple object is used so that the results can be easily interpreted.

The object mask consisted of a 10 μm thick gold foil perforated with three small laser drilled holes as shown schematically in Figure 3.5a. Average hole diameters (measured on a light microscope) are listed in the figure. The laser drilling produced irregular shapes, a typical cross-section of which is shown schematically in Figure 3.5b.

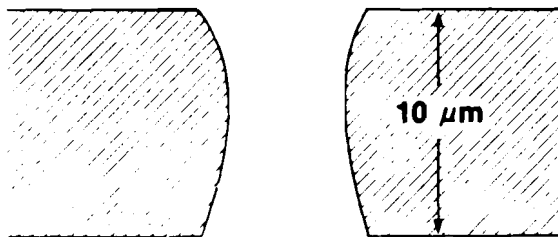
Two coded images of the object mask were recorded in the exposure system. The zone plate was of 2.5 μm thick gold and had an inner zone diameter of 400 μm and outer zone width of 16.3 μm (37 zones). The geometry of the exposure was $s_1 = 2$ cm, $s_2 = 10$ cm, yielding a first order resolution of just over 28 μm (see Figure 2.4).⁽⁵¹⁾ Two of the disks in the object were separated by the resolution distance, but they were of different radiance due to their different sizes, so they should not be resolvable in first order.

One shadowgraph was recorded linearly with a maximum density of 1.0 ($E_{\text{max}} = 6$ on the 7 keV curve in Figure 3.4). The other was nonlinearly recorded with a maximum density of 1.25 ($E_{\text{max}} = 10$ on the 9 keV curve in Figure 3.4). Diffraction efficiency is proportional to the square of the transmittance modulation, so the nonlinear reconstruction should be about 30% more efficient than the linear case; if it is assumed that diffraction efficiency is inversely

**OBJECT USED FOR COMPARISON OF
"LINEAR" AND NONLINEAR RECONSTRUCTIONS**



a. Schematic diagram of 3-point object
Hole diameter:
A- $4.3 \mu\text{m}$
B- $6.0 \mu\text{m}$
C- $7.4 \mu\text{m}$



**b. Schematic diagram of
typical hole-cross-section.**
Note varying diameter.

Figure 3.5

proportional to the square of the order number, then the nonlinear case will reconstruct higher orders than the linear case only if eighth order is obtainable in the linear case.

The nonlinear shadowgraph was contact-copied onto Kodak 649-F plate, and the plate was developed and bleached as described in Appendix I. Maximum efficiency of bleached plates occurred for a maximum prebleached density of about two. Equations [2.14] and [3.1] can be combined to obtain a fifth or sixth order polynomial for the 649-F prebleached t-E function. Bleaching changes t-E according to the discussion in Section 2.4.4, but the calculation will not be given here. It should be noted, however, that, due to their different t-E curves, the phase and nonlinear absorption reconstructions should not be identical.

Figure 3.6 shows the results of the reconstructions of the three coded images. Note that, as predicted, disks A and B of Figure 3.5 are not resolved in the first order reconstructions. Both absorption cases reconstruct sixth order, so the efficiency enhancement of the nonlinear over the linear case is not apparent. The phase is much more efficient than the absorption cases, as expected. Also, the nonlinear absorption case suffers some obscuration, possibly due to emulsion stress effects. This hypothesis is supported by the fact that the phase reconstructions, which were performed with the coded image in a liquid gate to mitigate emulsion relief effects, exhibit crisp images. The linear case, free of artifacts, has superior image fidelity, while the nonlinear cases suffer from deterministic degradation. In addition, the presence of

Figure 3.6 Reconstructions of "Linear" and Nonlinear Coded Images

Note the superior image fidelity of the linear reconstructions, especially in third order. The phase reconstructions are very crisp compared to the nonlinear absorption images, evidence that the liquid gate improves the reconstruction. Notice also that the phase reconstructions are obtained in much higher orders than the absorption reconstructions.

RECONSTRUCTIONS OF "LINEAR" AND
NONLINEAR CODED IMAGES

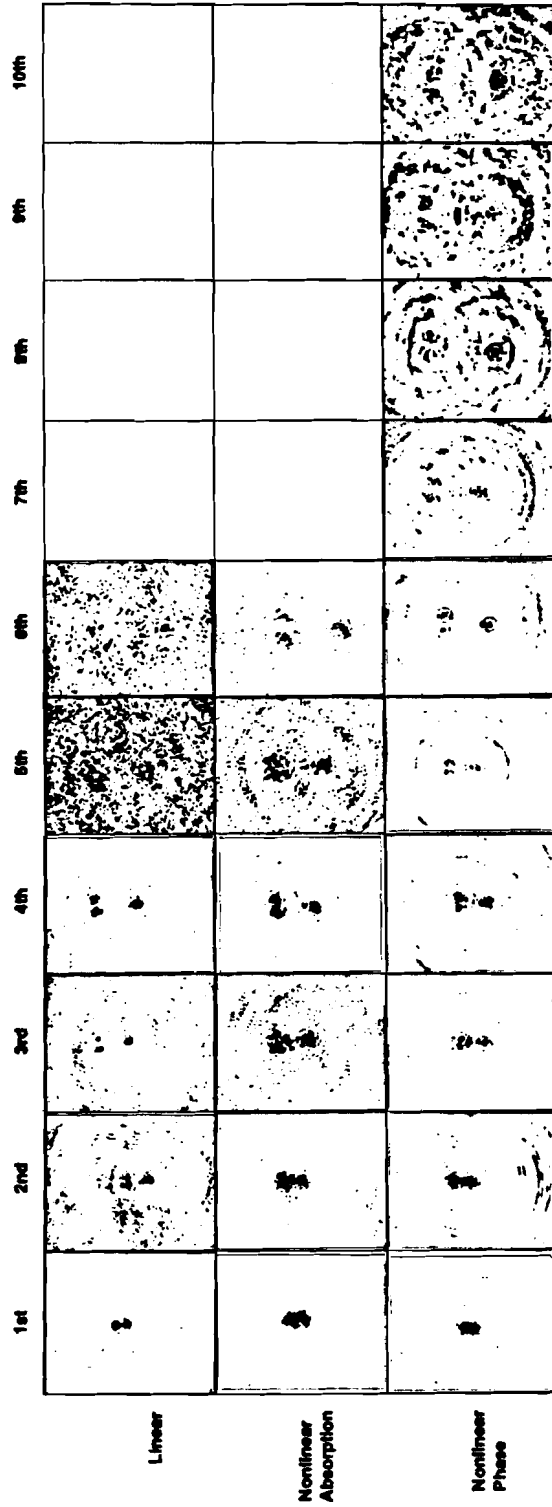


Figure 3.6

even-order images and the fact that sixth order is stronger than fifth order in the linear case suggest that Fresnel diffraction in the recording step caused redistribution of the Fourier coefficients of the zone plate transmission function.

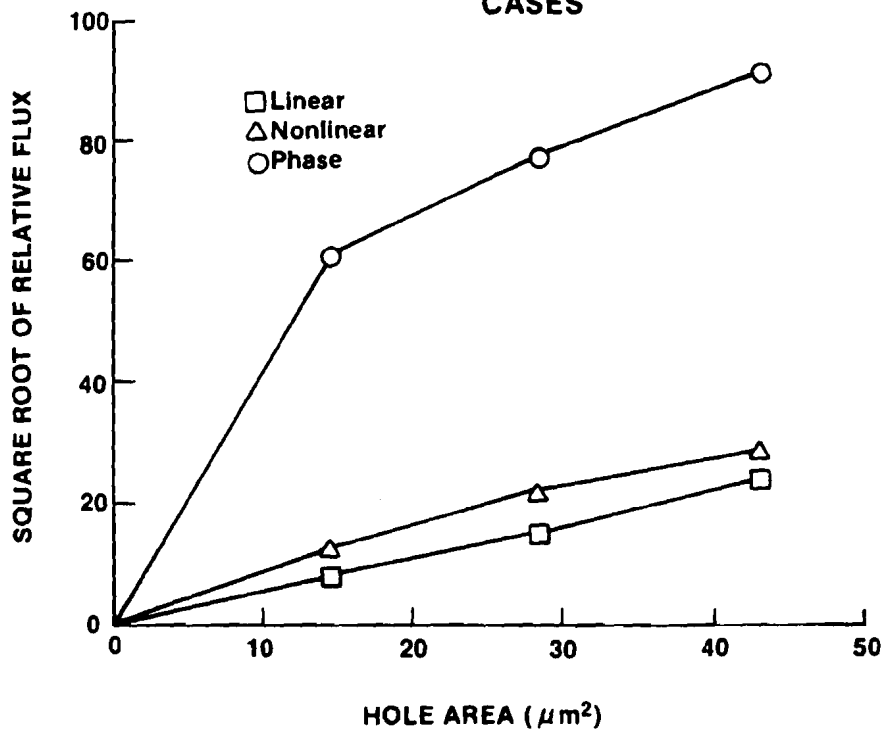
Table 3.1 displays results of flux measurements of the third order images in Figure 3.6. Total flux of each disk was measured with a photodiode. Neglecting phase effects in the linear case, the square root of the measured flux for any disk should be proportional to the area of the corresponding hole in the object foil. The nonlinear cases should not be loyal. Figure 3.7 is a graph of the square root of the measured flux vs area of the corresponding hole for the three cases. As indicated by the graph, the linear case is quantitatively correct, while the phase case is the least loyal image.

The nonlinear images suffer from irradiance compression, as might be expected from the shape of the nonlinearity in Figure 3.4. The stronger an object point, the more its corresponding image point irradiance is "compressed" in the nonlinear case. It is no surprise that the phase case has both the most prominent artifacts and the greatest image compression. Use of equation [3.1] with the nonlinear absorption case reveals that 50% of the reconstruction mask image transmittance contributes to artifacts, while 46% of the image flux is artifact flux. The phase case is even worse; from Figure 3.7 it can be shown that about 70% of the image flux is focussed into the artifacts. Indeed, the total flux in the eight most prominent artifacts in the third-order phase image was measured to be virtually identical to the total flux in the image points.

Table 3.1 **RELATIVE FLUX MEASURED AT
THIRD ORDER IMAGES OF THREE-
DISK OBJECT**

HOLE DESIGNATIONS/ AREA	RELATIVE FLUX (AND ITS SQUARE ROOT) MEASURED AT IMAGE OF HOLE		
	Linear Case	Nonlinear Cases	
		Absorption	Phase
A/ $14.5 \mu\text{m}^2$	73 (8.5)	165 (12.9)	3700 (60.9)
B/ $28.3 \mu\text{m}^2$	250 (15.8)	500 (22.4)	6020 (77.6)
C/ $43.0 \mu\text{m}^2$	600 (24.5)	860 (29.3)	8400 (91.7)

Figure 3.7 **SQUARE ROOT OF RELATIVE FLUX
VERSUS HOLE AREA FOR THREE
CASES**



The calculation of exact artifact strengths from equation [2.18] fails in practice because of the redistribution of the zone plate Fourier coefficients in the recording step. If the zone plate transparency function is exactly known, such a calculation would be possible. But it would be advantageous to measure the redistribution, and the only easy way to do such a thing requires a linear recording.

3.4.3 Role of Object Information Content in Artifact Formation

The conclusions of Chapter II indicated more than just the dependence of artifact formation on t-E nonlinearity. Artifacts were found to decrease in importance with increasing object size and to increase in importance with increasing spatial modulation of object emission. In other words, object information content strongly influences deterministic degradation. Some simple experiments illustrating this influence are now described.

3.4.3.1 Effect of Object Size

The effect of object size can be studied by comparing the various orders of reconstruction of a single object. For example, in first through fourth orders, the three-disk object of Figure 3.5 radiates from three resolution cells, while in orders higher than fourth, it effectively radiates from more than three resolution cells (e.g. in seventh order, it radiates from about 6.8 cells). Hence, orders higher than fourth should suffer less artifact degradation than first through fourth orders. Irradiance measurements confirm this idea. Visual comparison of the phase reconstructions in Figure 3.6 shows that artifacts tend to become less significant

with increasing order number above fourth order. Up to fourth order, however, the artifacts are of approximately equal importance in all orders, as expected.

The decrease in artifact significance with increasing order number is not coincident with a decrease in irradiance compression. The relative flux contribution at any disk is invariant with order number. The number of radiating resolution cells changes with order number, and at high orders, in which all disks are resolved, the number of cells occupied by a disk is proportional to the disk area. Thus, each cell in a disk suffers the same irradiance compression that the unresolved disk does in the low orders.

3.4.3.2 Effect of Object Modulation

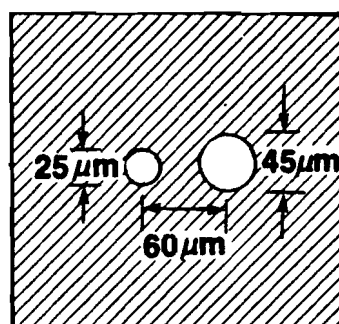
The greater the variation in strength of the emitters in the object, the greater the artifact degradation. This is illustrated by comparison of Figures 3.6 and 3.8. Figure 3.8a is a schematic diagram of a disk-pair object. The disks, of nominal diameters $25\ \mu\text{m}$ and $45\ \mu\text{m}$, are slightly elliptical and are separated by $60\ \mu\text{m}$ center-to-center. This object was encoded at 9 keV as previously described. Two recordings were made. The first resulted in $t_{\text{max}} = 0.9$, $t_{\text{min}} = 0.32$ (see Figure 3.4). The second was pre-exposed to light and had $t_{\text{max}} = 0.46$, $t_{\text{min}} = 0.38$. Figure 3.8b is the first order reconstruction of the first recording ($\Delta t = 0.58$), and Figure 3.8d is the reconstruction of the $\Delta t = 0.08$ recording. Figures 3.8c and e are plots of the irradiance distributions along lines joining the open circles in the reconstructed images.

In first order, the disk-pair object is only 17% larger than

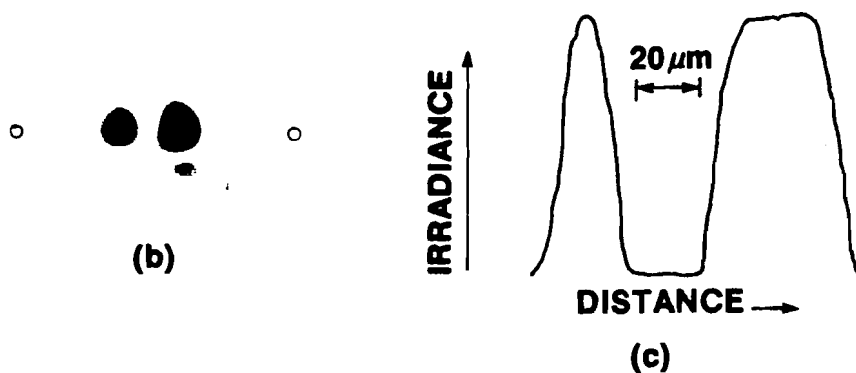
Figure 3.8 Schematic Diagram and Reconstructions of Disk-Pair Object

There is very little discernible difference between the nonlinear and linear reconstructions in this figure. This is due to the fact that there is no difference in the emission strengths of the various radiating cells in the object.

SCHEMATIC DIAGRAM AND RECONSTRUCTIONS OF DISK- PAIR OBJECT

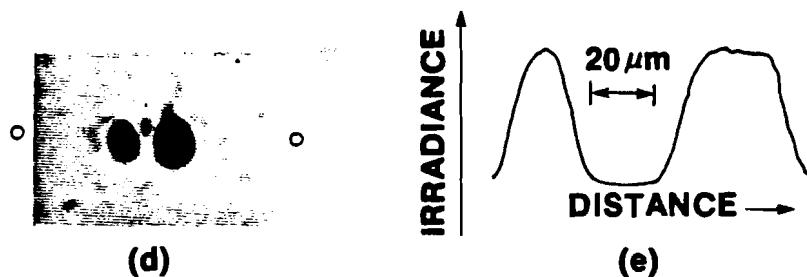


(a)



(b)

(c)



(d)

(e)

- (a) Schematic diagram of object foil
- (b) Nonlinear reconstruction of (a)
- (c) Irradiance distribution along line connecting circles in (b)
- (d) Reconstruction of (a) with less nonlinearity than in (b)
- (e) Irradiance distribution along line connecting circles in (d)

Figure 3.8

the three-disk object, which should result in only a small difference in deterministic degradation. However, $\Delta t = 0.58$ for the disk-pair in Figure 3.8b, while $\Delta t = 0.66$ for the three-disk object; the lower Δt and slightly larger size should combine to yield a more loyal reconstruction of the disk-pair. Yet it is still reasonable to expect some artifact degradation for the disk-pair. Figures 3.8b and d exhibit little if any degradation, though. The reason for this is that all radiating resolution cells in the disk-pair object emit the same amount of flux, while each radiating cell of the three-disk object emits an unique amount of flux. Equation [2.18] readily predicts greater image fidelity for the disk-pair.

All radiating cells in the disk-pair will experience the same irradiance compression, and the image fidelity is therefore not affected. On the other hand, the radiating cells in the three-disk object suffer varying compressions, as shown in Section 3.4.2, and image fidelity is degraded.

Comparison of Figures 3.8b and d suggests further the dependence of artifact formation on object modulation. The images were reconstructed from coded images with different effective t - E curves, yet there is no discernible difference in image fidelity (the t - E function for the recording resulting in the image of Figure 3.8d can be expressed as

$$t = 0.63 - 0.051 E, \quad [3.3]$$

where E varies from 3.33 to 4.9 in Figure 3.4). This comparison is analogous to the comparison in Figure 3.6 of the linear and nonlinear absorption reconstructions, in which a distinct difference

in image fidelity appears. Evidently, then, object modulation is a major factor in the degradation of image fidelity with increasing nonlinearity.

3.5 Studies of Grain Noise

As mentioned in Chapter II, it may be possible to increase SNR by bleaching the coded image. This section explores that idea in a three step approach. First, the grain noise distributions of uniformly exposed and developed plates are measured to explore any difference between bleached and unbleached media. Then the SNR for a simple disk object is evaluated for both absorption and phase reconstructions. Finally, the variation of SNR with object size is illustrated.

3.5.1 Grain Noise of Uniformly Exposed Plates

Usually the bleached mask in ZPCI will be a contact copy of the actual coded image; this arrangement allows flexibility in choosing both the recording medium and the reconstruction mask. X-ray films or track detectors can be used for encoding, while holographic media suitable for bleaching can serve as reconstruction masks. Holographic media have extremely low scattering properties because of their fine grain,^(45,46) and so the noise in the image field will actually be just that transferred from the original recording medium to the holographic plate in the copying step.

The problem of interest here is the determination of whether or not bleaching introduces additional noise in the medium. Suppose that, upon bleaching, the noise power increases just as much as the

diffraction efficiency. Then bleaching does not improve SNR. Only if noise power increases less than diffraction efficiency is anything gained by bleaching.

To address the problem, the following experiment was performed. Several Kodak 649-F plates were uniformly exposed and developed. Each plate in turn was placed in the experimental apparatus of Figure 3.9. The irradiance was measured in the back focal plane of the lens with a pinhole/diffuser/photodiode setup. The results of a representative case are given in Figure 3.10. The plates were then bleached in brominated methanol (Appendix I) and remeasured in the apparatus of Fig. 3.9. Figure 3.10 shows results of the bleached counterpart of the unbleached emulsion shown in the figure.

There was no discernible difference in the noise power of bleached and unbleached plates. Only signal power (i.e. d.c.) was different. In Figure 3.10, the measured points are connected by straight lines, which is why the two cases appear to have different noise levels below 2.5 cycles/mm. From the data of Figure 3.10, is safe to infer that bleaching can increase SNR.

3.5.2 SNR for Absorption and Phase Reconstructions of a Disk Object

What follows illustrates the increase in SNR achievable with bleaching. A disk object was chosen for this study due to the simplicity of the associated noise. The object is shown schematically in Figure 3.11a.

A shadowgram of the object was recorded on RAR 2491 film at 9 keV in the exposure system of Figure 3.2. As before, $s_1 = 2$ cm, $s_2 = 10$ cm, and the zone plate resolved 28 μm in first order. The

APPARATUS FOR MEASURING LIGHT SCATTERED FROM UNIFORMLY EXPOSED PLATE SPECIMENS

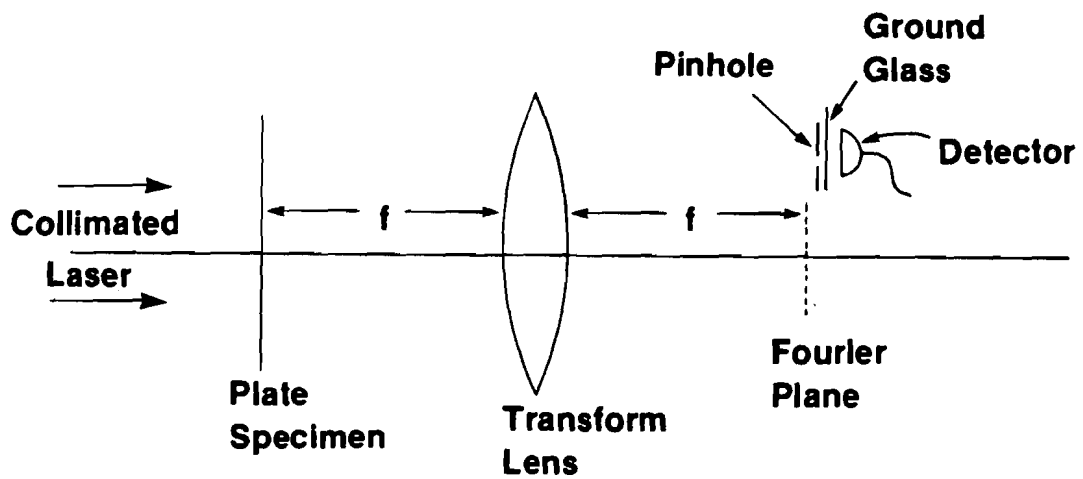


Figure 3.9

Figure 3.10

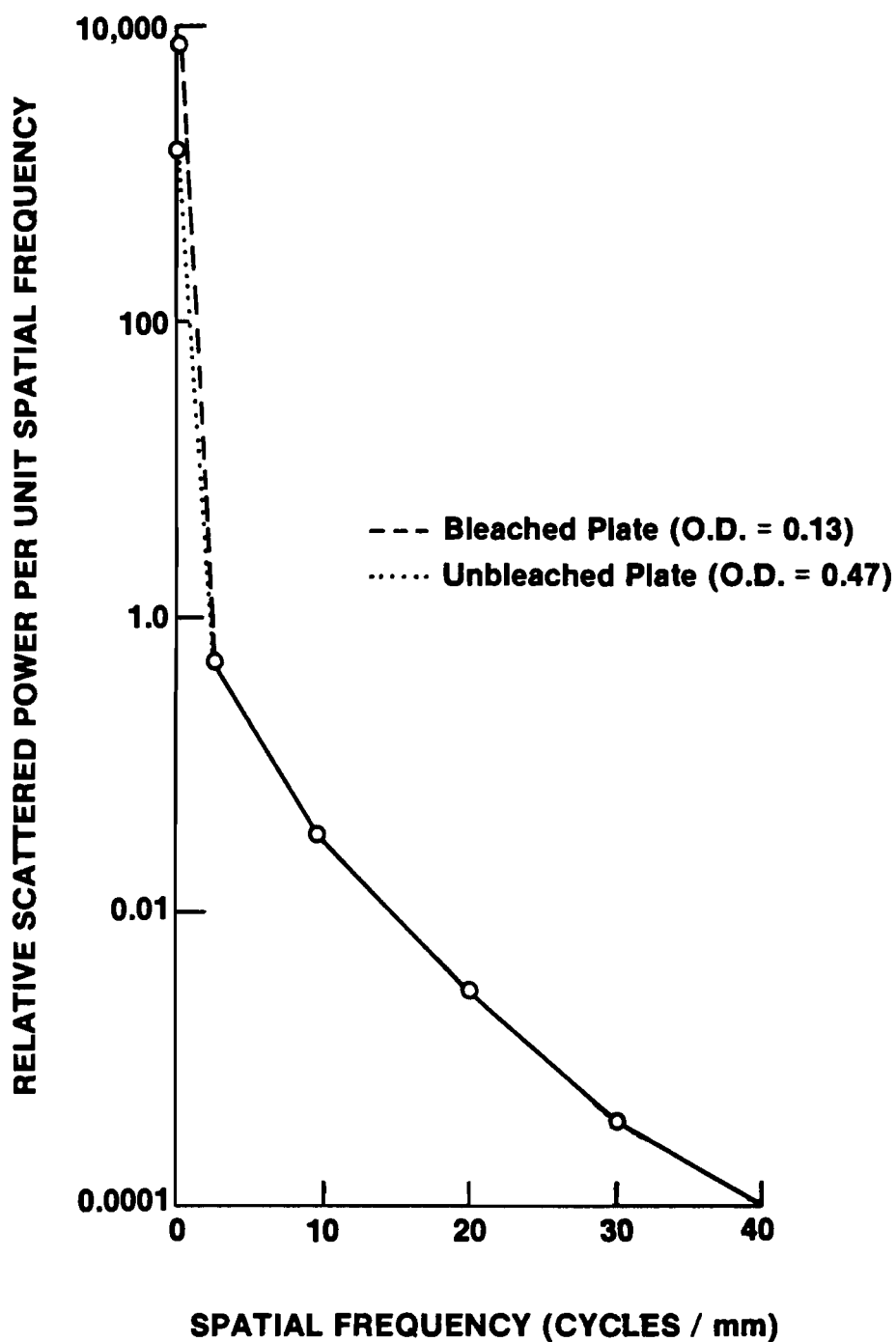
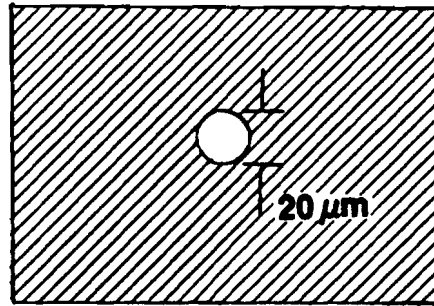
**RELATIVE SCATTERED POWER VERSUS
SPATIAL FREQUENCY FOR UNIFORMLY
EXPOSED 649-F PLATES**

Figure 3.11 Comparison of Absorption and Phase Reconstructions
of 20 μm Diameter Disk Object

As in Figure 3.6, the phase reconstruction provides higher diffraction efficiency than the absorption case, and higher order images are thus obtainable.

COMPARISON OF ABSORPTION AND PHASE RECONSTRUCTIONS OF 20 μm DIAMETER DISK OBJECT



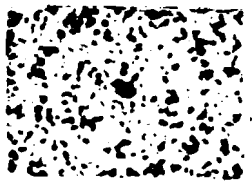
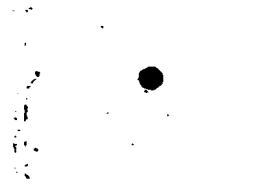
(a) Object Schematic

**Absorption
Reconstruction**

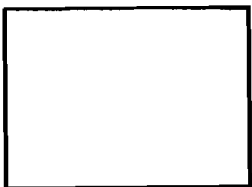
**Phase
Reconstruction**



First Order



Fourth Order



Seventh Order

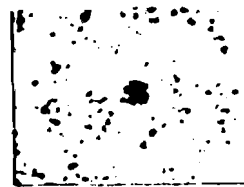


Figure 3.11

coded image was copied onto several 649-F plates, which were developed and bleached as in Appendix I. Table 3.2 is a list of the original shadowgram and the plates, their prebleached and post-bleached maximum optical densities, and their maximum orders of reconstruction (after bleaching for the plates) for $\text{SNR} > 1$. Figure 3.11b shows some of the images from the original shadowgram and plate d.

As might be anticipated from studies in holography, the phase reconstruction can be more efficient than the absorption case. The phase case peaks in efficiency for a prebleached density of about 2, similar to results obtained with other holographic plates bleached in bromine.⁽⁵²⁾ Notice also the difference in the appearances of the lowest order images; the liquid gate used in the phase case evidently permits a crisper image. The absence of sidelobes in the higher orders is due to the fact that the disk is unresolved in first order, so the manifestations of the coherent decoding are strongest there. A useful rule is to use a mid-order reconstruction to avoid both coherent effects for small, discrete object cells and noise limitations in the highest orders.

The gain in SNR for phase reconstructions must be weighed against the increase in deterministic degradation. If the object is continuous with no marked emission contours, bleaching can be useful. For discrete, small objects, bleaching may actually provide a gain in SNR but a loss in deterministic image fidelity. The gain in SNR for bleaching is determined by the efficiency of the original mask and the processing of the copy. The diffraction efficiency can be increased by as much as a factor of four, as was indicated in Section 2.4.5.2.

OPTICAL DENSITIES AND RECONSTRUCTION EFFICIENCIES
FOR ORIGINAL AND COPY CODED IMAGES

2491 film or 649-F plate	Maximum optical density		Maximum order with SNR > 1
	absorption	phase	
2491 film	1.40	—	6
plate a	0.40	0.06	3 (phase)
plate b	0.76	0.09	5 (phase)
plate c	1.54	0.15	7 (phase)
plate d	1.98	0.20	8 (phase)
plate e	3.15	0.24	6 (phase)

Table 3.2

3.5.3 Variation of SNR with Object Size

Equation [2.38] predicts that the noise transmittance has two factors, one random and one deterministic. The deterministic component $t(\underline{r})$ imparts to the noise the spatial distribution of the image. Hence, a noise model with a white spatial frequency spectrum would predict identical SNR for large and small objects, whereas it is known that small objects have higher SNR than large ones. The ξ factor in equation [2.38], which emphasizes low spatial frequencies, enables the model to predict increasing SNR for increasing high spatial frequency content in the object. Thus, large objects suffer lower SNR than small ones.

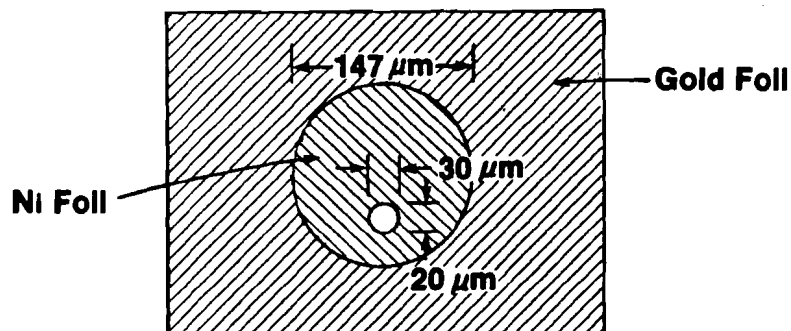
Figure 3.12a shows an object substantially larger than those of previous sections. Imaged under conditions identical to those used previously, the object appeared as in Figures 3.12b and c. Even the first order reconstruction was unfaithful. Evidently, the larger the object, the lower the SNR.

The case just presented provides an interesting example of the difficulty involved in calculating noise based on some average spatial frequency. The object contains both high and low spatial frequencies, and from Figure 3.12 it is clear that the low frequencies are more strongly affected by the noise. In this case, the object frequency spectrum is heavily weighted toward the low frequencies, and the average frequency is thus fairly low. On the other hand, an object with a large portion of high frequencies will have a higher average frequency. The images of Figure 3.12 appear to have significant high frequency content due to the presence of

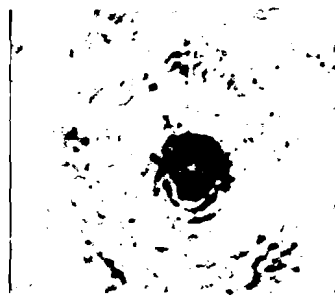
Figure 3.12 Reconstruction of Large Object

This case has low SNR. The graininess of the image might be misinterpreted as high frequency information, leading the user to believe that the image has significantly more deterministic degradation than it really does (see Section 4.3.2.2).

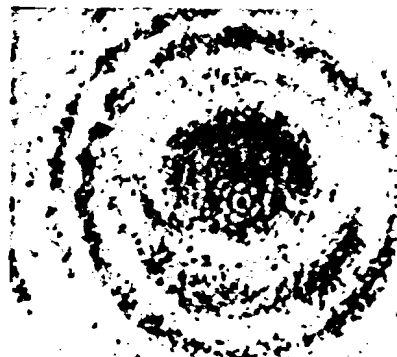
RECONSTRUCTION OF LARGE OBJECT



(a) Object Schematic . A $170\ \mu\text{m}$ diameter hole in Au foll was covered with $2.5\ \mu\text{m}$ thick Ni foll. A $20\ \mu\text{m} \times 30\ \mu\text{m}$ hole was drilled in Ni foll. This represents a small, bright object on a dim, diffuse background.



(b) First order reconstruction of (a)



(c) Second order reconstruction of (a)

Figure 3.12

noise, and the average frequency might be misjudged. It is important to have some a priori information about the object in order that such calculations can be made accurately.

3.6 Summary of Experimental Work

This chapter has confirmed the major results of Chapter II. Nonlinear ZPCI has been shown to degrade the image in a manner strongly dependent upon object information content. Noise has been shown to vary with object geometry and system linearity, with small objects and phase reconstructions providing highest SNR. However, SNR only includes noise, and cases of high SNR might actually have low image fidelity. For example, the phase reconstructions of Fig. 3.6 have the highest SNR in this study, but they have the worst deterministic image fidelity as well.

The presence of two distinct image degradation mechanisms in ZPCI is just cause for a reconsideration of figures of merit necessary to completely characterize the system. As seen in Figure 3.8, impulse response or relative contrast transfer can be constant for the system regardless of linearity or object information content. Yet linearity and information content are strong factors in determining image fidelity. Evidently, parameters such as resolution and contrast transfer suggest what can in principle be achieved with ZPCI, while in practice other concepts must be used. The next chapter addresses practical optimization.

CHAPTER IV
OPTIMIZATION OF ZPCI

4.1 Introduction

This chapter is the first presentation of a formal procedure for optimizing ZPCI. Following a short review of Chapters II and III, guidelines for estimating image degradation are developed. Examples are used to illustrate concepts and introduce the issues confronting the ZPCI user. Optimization evolves as a compromise between several issues.

4.2 Review of Results

In this section, factors determining the importance of each image degradation mechanism are reviewed.

4.2.1 Deterministic Degradation

Deterministic degradation is important for two reasons. First, the ZPCI system is rarely used in situations in which t - E is linear. Furthermore, nonlinear ZPCI can provide a significant increase in reconstruction efficiency over the linear case.

Artifact formation depends upon two factors: the exact nature of the nonlinearity and the object information content. Artifact strength increases with nonlinearity strength. For example, if equation [3.1] is the system t - E characteristic (with $E < 10$), the quadratic nonlinearity can produce artifacts as strong as the image (for small objects). On the other hand, increasing object size results in decreasing artifact importance. The information distribution in the object is important as well; diffuse objects are imaged more loyally than objects with high modulation.

4.2.2 Noise

Noise is determined by (1) the properties of the detector in the recording step, (2) object emission strength (shot noise), and (3) object information content. Film grain noise peaks at low spatial frequencies. Object information content determines the spatial frequency spectrum of the object. Broader objects suffer more grain noise than small ones. Shot noise can be a problem in particle imaging, in which low object flux results not only in higher random transmittance fluctuation in the reconstruction mask but also in less diffraction efficiency.

4.3 Optimization

In this section, procedures for estimating image degradation are developed. In the estimation of both artifacts and noise, the uniform object is treated first. The treatments are then extended to include more complex objects. Finally, the process of optimization is illustrated with examples.

4.3.1 Efficiency of a Single Information Element

An information element is the smallest amount of information measurable in the object. For N radiating resolution cells in the object and G_j information elements in the j^{th} cell, the object contains

$$G = \sum_{j=1}^N G_j \text{ information elements. [4.1]}$$

The recording step exposure can be thought of as consisting of G information elements rather than N resolution cells, with all elements emitting the same amount of flux. Thus, all elements

have the same image field strength (in linear ZPCI). Some elements coincide spatially. Equation [2.10] can be rewritten:

$$E = \sum_{j=1}^G \alpha_0^2 (1 + 2\bar{g}_j). \quad [4.2]$$

All quantities are defined as in Section 2.4.2. Equation [2.7] can be written as

$$f(\underline{x}) = \sum_{j=1}^G \delta(\underline{x} - \underline{R}_j), \quad [4.3]$$

where some of the R_j may be coincident.

It is readily seen that the relative diffraction efficiency for a single information element is $1/G^2$, if none of the R_j coincide. However, if some R_j 's coincide, all the information elements at a given position add coherently in reconstruction, and the relative efficiency of the i^{th} pixel will be G_i^2/G^2 . The single information element can be considered independently of other (spatially coincident) elements only in terms of reconstruction field amplitude.

4.3.2 Estimation of Deterministic Degradation

The problem of accurately determining artifact strengths was alluded to briefly in Section 2.4.5.4. Since deterministic degradation cannot be directly measured, some estimation criteria must be devised. Evidently, film linearity, object size, and object modulation must be included in the estimation process. It is assumed here that the artifact distribution can be found in any reconstructed order, much as the image can. With the possible exception of particle imaging, this is a safe assumption. Hence, artifact and image strength are compared directly.

4.3.2.1 Artifact Distribution for a Uniform Object

The uniform object represents the simplest case for estimating artifact strengths. For a uniform object of N resolution cells, the ratio of the reconstruction diffraction efficiency of a single k^{th} order artifact to that of an image cell is

$$\frac{\Delta\eta_k}{\Delta\eta_1} = \left(\frac{\alpha_k}{\alpha_1} \right)^2 \frac{1}{N^{2k-2}} .$$

For the RAR 2491 film of equation [3.1], with $N = 20$, $\frac{\Delta\eta_2}{\Delta\eta_1} \approx 10^{-4}$. The total image-to-artifact ratio is $\eta_1 / \eta_2 \approx 3 \cdot 10^{-3}$.

The quadratic artifact contribution at a point in the image of an extended object can be spatially averaged over several artifacts if the object consists of discrete emitting regions and the emitting regions all have similar strengths. If the object is continuous, spatial averaging is unnecessary, as in the case of the uniform object. For a uniform disk object of radius R , it is easy to show that the quadratic artifact strength at a point a distance d from the center is proportional to $R^2 \cos^{-1}(d/R) - d\sqrt{R^2 - d^2}$. For a disk covering twenty resolution cells, then, the artifact irradiance can be as much as 10^{-2} times the image irradiance (this occurs at the center of the image). Thus, even if the central resolution cell of the disk is non-emitting, the artifact irradiance at that point is negligible.

4.3.2.2 Artifact Distribution for an Object with Contours

The preceding discussion appears to indicate that artifacts are negligible compared to the image irradiance. For extended objects with smooth contours, this is indeed the case. Nonlinear

imaging of objects with sharp contours, however, can produce artifacts which are significant, and a method for estimating the significance is then necessary. Computation of artifact strength requires knowledge of the film t-E curve, the object spatial and spectral distributions, and the propagation characteristics of radiation through the recording system. If the object spatial distribution is not known, deterministic degradation is difficult to assess.

Consider a three-point object recorded with t-E as in equation [3.1] and exposure not exceeding ten in Figure 3.4. Let the worst case be invoked, in which two of the points produce equal exposures (E_2) and the third point produces a weak exposure E_1 ($E_1 < E_2$). In order for the image of the weak point to be stronger than the quadratic artifact produced by the nonlinear interaction of the two stronger exposures, $\alpha_1 E_1 > \alpha_2 E_2^2 / 2$. Thus, $E_2 < 2.41 E_1$.

If E_1 is distributed over more than one resolution cell, E_2 must be smaller in order that the artifacts be smaller than the weak areas of the image. Let E_1 be distributed evenly over M cells.

Then

$$\frac{E_1}{E_2^2} > \frac{\alpha_2^M}{2\alpha_1} \quad [4.2]$$

Also, since $2E_2 + E_1 = E_{\max}$, then

$$E_2 < \frac{-4\alpha_1}{M\alpha_2} + \sqrt{\frac{16\alpha_1^2}{M^2\alpha_2^2} + \frac{2E_{\max}\alpha_1}{M\alpha_2}} \quad [4.3]$$

Increasing M requires decreasing E_2 . For practical purposes, the weakest nonzero image irradiance should exceed the strongest

artifact by some safety factor. This can be directly incorporated into equation [4.2].

The case just discussed is particularly poor in image fidelity. More general cases can be imagined, but the problem of estimating image fidelity still remains. Estimating deterministic image fidelity for small, discrete objects should not be necessary because those objects should always be imaged linearly, as shown in Section 3.4.2. The discussion here will concentrate on extended objects of more than about ten radiating cells.

Recall from equation [4.1] that G is proportional to the total exposure in the encoding step. For N radiating object cells, the average cell contains \bar{G} information elements with a standard deviation of σ elements, where

$$\bar{G} = \frac{\sum_{j=1}^N G_j}{N} = \frac{G}{N} \quad [4.4]$$

and

$$\sigma = \sqrt{\frac{N \sum_{j=1}^N G_j^2 - \left(\sum_{j=1}^N G_j \right)^2}{N(N-1)}} \quad [4.5]$$

Define the mean object variation, V , as

$$V = \sigma / G. \quad [4.6]$$

The artifact amplitude transmittance is proportional to the square of the exposure variation, so artifact irradiance is proportional to V^4 . Further, the ratio of σ^2 (the variance) to the total artifact transmittance is independent of N . This striking result indicates that artifact degradation can be estimated if $\sum G_j^2$, $(\sum G_j)^2$, and N are known.

$(\sum G_j)^2$ is easily measured during reconstruction as the flux

in the d.c. term. For a linear recording, $\sum G_j^2$ is the total image flux. For nonlinear ZPCI, the "image" flux contains artifact contributions as well as desired image information. Remember from Chapter II that $\sum G_j^2$ contains information about N, so N is found in the total image flux, but again the presence of artifacts obscures the information. N can also be found by measuring the image size. This method introduces error in the value for N because artifacts are counted as image cells. Measurement of image flux will yield a low value for N, whereas measurement of the image size yields a high value for N. The average of these two values is a reasonable value to use for N. The following prescription for evaluating artifact significance can be used:

- (1) Know the t-E function for the film being used.
- (2) For a given coded image, find the total exposure by measuring the d.c. flux in the reconstruction.
- (3) Find t_{\max} and t_{\min} for the coded image.
- (4) Compute the diffraction efficiency vs N for the linear transmittance component.
- (5) Measure the total image flux. This will include both artifacts and loyal image contributions and will be larger than the loyal image flux alone.
- (6) From (4) and (5), compute a value for N. This value will be lower than the actual value. Call this value N_1 .
- (7) Measure the image size to find N. This value will be too high. Call it N_2 . Let $\bar{N} = \frac{1}{2} (N_1 + N_2)$.
- (8) Compute σ . This calculation will contain an overestimated

value for $\sum_j G_j^2$ and can be corrected by multiplying $\sum_j G_j^2$ by an underestimated value for N, namely N_1 . \bar{N} can be used as a reasonable estimate of N for the rest of the calculation. Hence,

$$\sigma = \sqrt{\frac{N_1 \sum_j G_j^2 - \left(\sum_j G_j \right)^2}{\bar{N} (\bar{N} - 1)}} \quad [4.5a]$$

and

$$V = \frac{\sigma}{G} \cdot \quad [4.6a]$$

Now that σ and V can be easily found, artifact flux must be related to these quantities. Since $N > 10$, it is safe to use the total artifact flux divided by the image area as the artifact irradiance. This approximation is safest when the object contains only smooth contours, but it can still provide reasonable estimates for objects with sharp contours. For $V = 0$, i.e. for a uniform object, artifact degradation can be calculated accurately. For $V \rightarrow 1$, artifact degradation can be equated to the worst case, i.e. two bright spots containing most of the energy as described earlier. With these two limiting values for artifact irradiance, the V^4 dependence permits artifact strength to be calculated for any value of σ . Since there is still artifact flux for $V = 0$, the expression for the flux will be of the form

$$F_a = F|_{V=0} + \beta_N V^4, \quad [4.7]$$

where $\beta_N = F_a$ for the worst case with N resolution cells. Minimum artifact irradiance occurs at $V = 0$ and is a small value.

β_N is the upper limit for F_a (neglecting $F|_{V=0}$) and can be calculated in the following manner. All radiating source cells (except two) each consist of one information element. The remainder

of the information elements are equally divided between the other two cells. Thus, β_N is dependent upon N and G .

Equation [4.6a] is the most useful indicator of artifact strength. For example, $V = 0$ for the two-disk object of Figure 3.8, while for the object of Figure 3.5, $V = 0.55$ (strictly speaking, neither object subtends enough resolution cells in first order to be large enough to use this analysis, but the results should indicate the applicability of mean object variation to artifact estimation).

Section 4.3.3 Noise Strength and Object Size

SNR was defined in Chapter II. The purpose of this short section is to outline a simple procedure for estimating average frequency of the image.

The calculation of average frequency ξ_0 in equation [2.40] can be performed by Fourier transforming the image and locating the mean frequency. Let $F(\underline{\xi})$ represent the irradiance of the Fourier transform of the image. The total flux in the Fourier transform is given by

$$\int_{-\infty}^{\infty} d^2 \xi F(\xi) = I_F .$$

Let $|\xi_{\min}|$ be the minimum image frequency ($|\xi_{\min}|$ is determined by the maximum extent of the image). Let $|\xi_{\max}|$ be the high frequency cutoff of the projected zone plate shadow. Then the mean flux per unit frequency is $I_M = I_F / (|\xi_{\max}| - |\xi_{\min}|)$. The mean frequency ξ_0 can be found by the following equations:

$$I_F^* = \int_{-\infty}^{\infty} d^2 \underline{\xi} F(\underline{\xi}) \underline{\xi}$$

$$\xi_0 = \frac{I_F^*}{I_F} .$$

It is useful to calculate the standard deviation of the average frequency as well;

$$\sigma = \sqrt{\frac{\int F(\xi) \xi^2 d^2 \xi - I_F(\xi_0)^2}{I_F - 1}}$$

Note here that I_F must be made much larger than unity. From Section 4.3.2.2, $I_F \approx G$ for convenience. If σ/ξ_0 is large, then ξ_0 has little meaning, as in the case of two points separated by a large distance.

Since finding SNR involves an extra task during reconstruction, image degradation mechanism. Artifacts can be estimated from quantities measured in the reconstruction.

4.3.4 Optimization Procedures

This section is the most important one in the thesis because it contains specific optimization procedures. Due to object size constraints, the only prevalent use for ZPCI is inertial confinement fusion (ICF), in which the typical source is of limited spatial extent and emits copious amounts of high energy photons and particles. Thus, the discussion here will focus on ICF applications of ZPCI.

The primary tools in ZPCI optimization are shadowgram processing and the reconstruction bench. Depending upon the nature of the information desired, the procedures for using these tools vary. The following paragraphs illustrate the procedures in general fashion and with two practical examples.

Several decisions must be made concerning the imaging arrangement before encoding can be performed. The radiation to be detected determines the recording medium, zone plate material and thickness,

and filtering. The required nominal lateral spatial resolution defines the outer zone width, and the anticipated object size defines the zone plate size. For purposes of film calibration, the innermost transparent zone should not resolve any object structure.

Linear ZPCI is not always a practical reality, and much of the decoding effort should be devoted to determining image fidelity. Four constituent procedures are involved. First, a t-E calibration for the encoding detector is required. Second, the detector must be processed to occupy the desired region of the t-E curve. Next, comparison diagnostics should be available for corroborating results with the zone plate camera. Finally, fidelity measurements must be performed (as outlined in Sections 4.3.2.2 and 4.3.3), and the best reconstructed order can be chosen.

t-E calibration is necessary unless the encoding detector has known properties. In ICF, t-E can vary from shot to shot, especially for soft x-rays. Track detectors do not require t-E calibration because they respond fairly uniformly from shot to shot. Calibration data can be obtained by inserting detectors (identical to the encoding detector) at various distances from the object and with filtering and processing identical to that of the encoding detector. The calibration exposures should be obtained in a camera situated adjacent to the zone plate camera to avoid directional emission effects due to phenomena such as plasma opacity.

The lack of exposure control in ICF can be accommodated by controlling film processing. Developer conditions can be altered

to control the dynamic range of silver halide x-ray detectors, but t-E linearity is not easily controlled. Processing changes should be used to impart to the coded image the appropriate density range. Thus, the calibration camera should have two detectors for each exposure level; one set of detectors is processed in a prescribed manner, and the resulting t-E curve is used to determine what processing should be used for the second set of detectors (and the coded image). The second set of detectors provides the t-E calibration for the coded image. Note that if the width of the innermost transparent zone in the zone plate is larger than the object, the maximum density on the shadowgram is known before it is processed.

An alternative calibration method is the film stack approach of Ceglio,⁽⁴⁸⁾ in which several films and appropriate filters are sandwiched in the zone plate camera. Development of one shadowgram provides information about the development required for the remaining shadowgrams. This method does not provide t-E information, but it can be used in the calibration camera as well as the zone plate camera to provide t-E information for several spectral channels simultaneously. Film stacks require much labor and are best kept to a minimum if possible.

The importance of companion diagnostics cannot be overemphasized. In many cases, especially those of strong deterministic degradation, it is useful to know the gross features of the object in order to provide a rough check of the image fidelity of the ZPCI camera.

Once the above requirements have been satisfied, the actual

reconstruction can begin. The first order focal length should be determined as in Figure 1.2. Then the system of Figure 3.3 can be used to perform the reconstruction with all orders at predetermined distances from the d.c. block. The procedure of Section 4.3.2.2 can then be used to determine image fidelity. In addition, if noise is a suspected problem, the procedures of Section 4.3.3 can be used. If more than one image order is obtainable, the noise should not be too troublesome in the lowest order.

Should the object display minimal structure, higher resolution might be desired. The coded image can be copied and bleached as in Appendix I, and the additional image efficiency of the bleached copy can be used to obtain higher order images than the original. In this case, a t-E curve must be estimated, and the image information is only qualitative. The increased resolution mitigates artifact formation in the higher orders.

The image with superior fidelity must be a compromise between artifact formation, resolution, and SNR. Such a compromise depends to a great extent upon subjective interpretation. The maximum tolerable noise level should not be exceeded, but the problem of determining noise is complex, as noted earlier. Nonetheless, at some high image order the noise will become stronger than the image, and so typically a middle order is the best image. Figure 3.6 provides a good example of the compromise.

The optimization procedures outlined here have not included calculations of information capacity because, as with any image evaluation criterion, information capacity varies with object

information content and system linearity. Equations such as [4.7] are much more useful in calculating the impact of nonlinearity, object size, and zone plate size. The most important aspect in ZPCI is the understanding of how each variable in the system is related to every other variable; such an understanding results in prudent application of the system. The following examples provide an overview of the considerations necessary in applying ZPCI to the imaging of laser fusion plasma emissions.

4.3.4.1 Example: α -Particle Imaging

α -particle imaging is useful for diagnosing thermonuclear burn characteristics in ICF.⁽¹⁴⁾ ZPCI is ideally suited to α -particle imaging for several reasons. First, the encoding step is very nearly ideal; there is no diffraction of the particles, so the only contribution to imperfect shadowcasting is the scattering of particles obliquely incident on zone edges. Also, since the track detector is a binary detection medium (Section 2.4.4), a contact copy of the coded image can have controlled t-E properties. Finally, shot noise is the dominant image degradation, so increasing the zone plate size can improve SNR. Grain noise can be minimized by copying the coded image onto a fine-grain emulsion.

Gold zone plates about 6 μm thick are sufficient to encode 3.5 MeV α -particle emissions in ICF. Cellulose nitrate (CN) can be used as the detector. After development, CN can be contact-copied in green light onto a fine-grain emulsion, which then serves as the reconstruction mask. If the CN track density is low, the

copy can be made onto a coarse-grain emulsion, but grain noise then becomes a problem.

Reconstruction of the coded image proceeds in the prescribed manner. It is useful to first decode a linear copy; the presence of even order reconstructions would indicate imperfect shadowcasting. Linear decoding allows quantitative image analysis. If even orders are not present in the linear case, a nonlinear reconstruction can then be performed; in this case, the even orders yield quantitative artifact information, and the image fidelity can be estimated without the procedures of Section 4.3.2.2.

There is evidence that the α -particle image is a sensitive indicator of implosion symmetry in ICF. Figure 4.1a shows soft x-ray and α -particle images from a highly symmetrical implosion of a D-T fusion target performed on the six beam Zeta laser system at the University of Rochester. Even with the spherically symmetric x-ray emission, the α -particle image shows evidence of "spokes," i.e. of the six beam imprints. Figure 4.1b is the x-ray image of another implosion with different laser focussing conditions than those in Figure 4.1a. Such asymmetry would be obvious in the corresponding α -particle image. It is imperative in situations such as these that the image fidelity be superior in order to avoid erroneous data interpretation.

4.3.4.2 Example: X-Ray Imaging

While α -particle imaging is particularly easy with ZPCI, x-ray imaging is very challenging. The encoding step will be degraded by

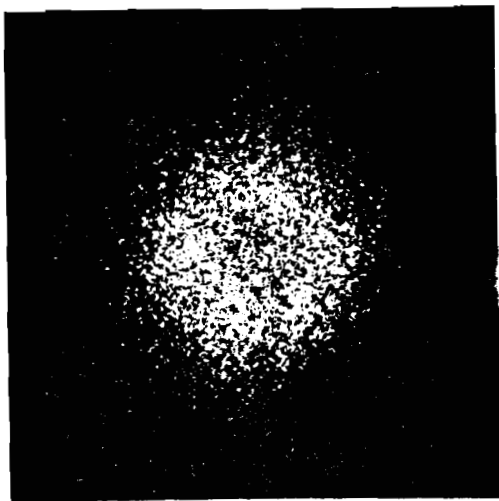
Figure 4.1 Images of X-Ray and α -Particle Emissions in ICF Studies.

- (a) X-ray and α -particle images from a highly symmetrical laser-fusion implosion experiment. The α -particle image shows evidence of the imprints from the six laser beams that irradiated the spherical target.
- (b) X-ray image from a target irradiated with the laser beams focussed on the surface of the target. Note the modulation in the image. The α -particle image from the same target might exhibit beam imprint effects very clearly here, but the particle flux is so low in this type of experiment that it is difficult to obtain a coded image.

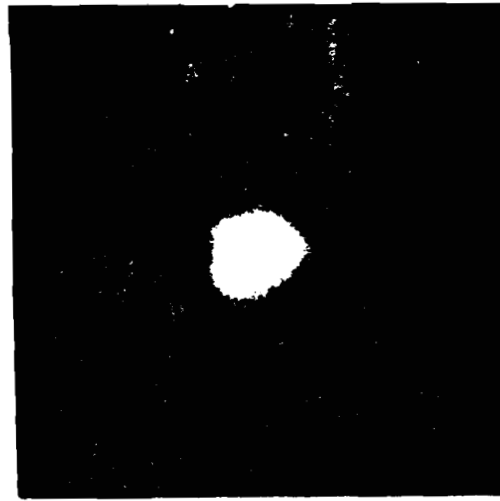
The photographs in (a) will appear in J. Soures, et. al., "A Review of High Density, Laser Driven Implosion Experiments at the Laboratory for Laser Energetics," in Laser Interaction and Related Plasma Phenomena, V. 5, H. Schwartz, H. Hora, M. J. Lubin, and B. Yaakobi eds., Plenum Press, New York, 1981. They also appeared under the same title in LLE technical memo #98. All photographs in this figure are reproduced with the permission of the Laboratory for Laser Energetics of the University of Rochester.

a

X-RAY IMAGE



ALPHA ZONE PLATE IMAGE



X-RAY IMAGE

b

Fresnel diffraction effects and partial x-ray transmission through zone edges. Hence, even orders will always be reconstructed. The outer zone width must be chosen to be large enough so that its Fresnel diffraction pattern is not wider than its shadow. For such purposes, the longest wavelength to be encoded can be used in the Fresnel diffraction calculation (for a slit the width of the outer zone and a point source and observing screen positioned as in the encoding geometry).

The t-E curve for x-rays will vary significantly depending upon plasma conditions and in general will be nonlinear. The calibration camera of Section 4.3.4 is useful in this case. A moderate developer such as D-19 should be used for the initial t-E calibration, and subsequent calibrations can be made with other developers as needed.

X-ray exposures offer little versatility in film processing due to the nonlinear nature of the original coded image. However, when only qualitative information is desired, bleaching can be used to increase SNR. Ideally, the original coded image should be recorded on a photographic plate so the emulsion can be directly bleached. ICF plasmas usually emit enough x-rays that high resolution plates can be used. If the x-ray flux is low enough that a coarse-grain recording medium is required, then the coded image should be copied onto a plate which can be bleached.

The optimization steps of Section 4.3.4 should be followed rigorously with x-ray images. Some relevant points are:

- (1) The innermost transparent zone of the zone plate should be wider than the source extent for easy measurement of the total exposure, a quantity of interest for the optimization relation (equation [4.5a]).
- (2) The t-E calibration yields, for a given object, the total image flux expected in the reconstruction. Any deviation from this value can be attributed to artifact flux. Note that the flux in all orders must be measured in order to account for the effects of Fresnel diffraction in the encoding step.
- (3) Image size can be measured easily with an automated data acquisition system, such as an optical multichannel analyzer. The discussion here should make it clear that ZPCI should not be used for x-ray imaging unless no other diagnostic provides adequate information. In ICF, examples of such needs include suprathreshold x-ray imaging and the high energy tail of the thermal x-ray spectrum, both of which are low flux cases, poorly suited to pinhole camera imaging or grazing reflection microscopy.

CHAPTER V

SUMMARY AND SUGGESTIONS FOR FUTURE INVESTIGATIONS

The objectives of this thesis have been to investigate image degradation mechanisms in ZPCI and to devise image characterization and optimization procedures. This chapter contains a summary of the contributions made and suggestions for future work in zone plate imaging.

Several contributions were made in ZPCI theory. A simple categorization scheme of optical coded imaging systems culminated in an analogy between ZPCI and multiple exposure holography, facilitating the analyses of deterministic degradation and noise. The treatment of nonlinear ZPCI was generalized to include phase reconstructions, raising questions concerning both image efficiency and image degradation. Artifact formation was analyzed with and without the assumption of perfect shadowgraphy in the encoding. Perfect shadowcasting leads to simple image analysis, whereas practical use of ZPCI leads to a more complicated deterministic degradation problem in which artifacts are order-independent. Finally, a noise model was developed to account for effects due to mask density variations and object spatial frequency content.

Three experimental contributions were made. The first quantitative comparison of linear and nonlinear ZPCI was performed, clarifying the roles of object information content and system nonlinearity. The first experimental studies of grain noise investigated in qualitative fashion the variation of SNR with both object information content and system nonlinearity. Thick zone plate fabrication was improved by the application of reactive sputtering to the process.

The primary contribution of this work was in the area of optimization, which is a balance of image degradation and image efficiency. Simple, reliable methods for determining image fidelity were devised. ZPCI can now be applied with confidence.

Several areas deserve further consideration in ZPCI. Work in zone plate fabrication should concentrate on submicron zone widths with aspect ratios of ten or higher. Such zone plates would permit particle imaging with submicron resolution. Tailored zone profiles would be beneficial in x-ray ZPCI to boost the efficiencies of arbitrary image orders. Fabrication of tailored zone profiles is a difficult task and would require the use of complicated phenomena such as faceting effects in ion etching.

The most important area in ZPCI at the moment is automated data acquisition, which would permit easy estimation of image degradation and computerized image enhancement techniques. Other areas of interest are off-axis imaging and quantitative noise studies. Off-axis ZPCI eliminates the d.c. reconstruction term; it can also be used with spatial heterodyning to shift the object frequency content into a region in which noise is reduced from its low frequency peak. Quantitative noise studies should be done with linear imaging in order to avoid confusion in image interpretation.

REFERENCES

1. L. Mertz and N. O. Young, "Fresnel Transformation of Images," in Proc. Int'l. Conf. on Opt. Instr., London, 1961, pp. 305-312.
2. H. H. Barrett, et. al., "The Use of Half-Tone Screens in Fresnel Zone Plate Imaging of Incoherent Sources," Opt. Commun. 5, 398-401 (1972).
3. H. H. Barrett, et. al., "A Spatially-Coded X-Ray Source," Radiology 104, 429-430 (1972).
4. H. H. Barrett, et. al., "Fresnel Zone Plate Imaging in Radiology and Nuclear Medicine," Opt. Eng. 12, 8-12 (1973).
5. H. H. Barrett and F. A. Horrigan, "Fresnel Zone Plate Imaging of Gamma Rays; Theory," Appl. Opt. 12, 2686-2702 (1973).
6. J. Fonroget, et. al., "Fonction de Transfert du Modulation d'un Systeme de Gammagraphie Holographique," Opt. Commun. 15, 76-89 (1975).
7. J. Brunol and J. Fonroget, "Bruit Multiplex en Gammagraphie Par Codage," Opt. Commun. 22, 301-306 (1977).
8. J. Brunol, et. al., "Imagerie Tridimensionnelle en Gammagraphie," Opt. Commun. 25, 163-168 (1978).
9. J. Brunol, et. al., "Micro-Coded Aperture Imaging Applied to Laser Plasma Diagnosis," Opt. Commun. 31, 129-134 (1979).
10. E. E. Fennimore and T. M. Cannon, "Coded Aperture Imaging with Uniformly Redundant Arrays," Appl. Opt. 17, 337-347 (1978). See also G. N. Minerbo, et. al., "Three-Dimensional Reconstruction of the X-Ray Emission in Laser Imploded Targets," Appl. Opt. 19, 1723-1729 (1980).
11. N. M. Ceglio, "Zone Plate Imaging of Laser Produced Plasmas," PhD Thesis, Massachusetts Institute of Technology, 1976.
12. N. M. Ceglio, "Zone Plate Coded Imaging on a Microscopic Scale," J. Appl. Phys. 48, 1563-1565 (1977).
13. N. M. Ceglio, et. al., "Zone Plate Coded Imaging of Laser-Produced Plasmas," J. Appl. Phys. 48, 1566-1569 (1977).
14. N. M. Ceglio and L. W. Coleman, "Spatially Resolved α -Emission from Laser Fusion Targets," Phys. Rev. Lett. 39, 20-23 (1977).
15. J. Gur, "Pseudoholography at High Orders," PhD Thesis, University of Rochester, 1978.

16. J. Gur and J. M. Forsyth, "Optical Simulation of a Technique for Obtaining Submicron Resolution X-Ray Images in Laser Pellet Compression Experiments," *Appl. Opt.* 17, 1-2 (1978).
17. D. Gabor, "Microscopy by Reconstructed Wavefronts," *Proc. Roy. Soc. (London)* A197, 454-487 (1949).
18. G. L. Rogers, "Experiments in Diffraction Microscopy," *Proc. Roy. Soc. (Edinburgh)* A63, 193-221 (1952).
19. E. N. Leith and J. Upatnieks, "Reconstructed Wavefronts and Communication Theory," *J. Opt. Soc. Am.* 52, 1123-1130 (1962).
20. A. W. Lohmann, "Reconstruction of Vectorial Wavefronts," *Appl. Opt.* 4, 1667-1668 (1965).
21. L. Mertz, "Orthogonal Transformations Appropriate to Optics," *J. Opt. Soc. Am.* 50, 505 (1960).
22. N. O. Young, "Photography Without Lenses or Mirrors," *Sky and Telescope* 25, 8-9 (1963).
23. M. H. Horman and H. H. M. Chau, "Zone Plate Theory Based on Holography," *Appl. Opt.* 6, 317-323 (1967).
24. K. I. Clifford and G. S. Waldman, "Comments on Zone Plate Theory Based on Holography," *Appl. Opt.* 6, 1415 (1967).
25. M. H. Horman, "Reply to Comments on Zone Plate Theory Based on Holography," *Appl. Opt.* 6, 1415-1418 (1967).
26. D. B. Brown, et. al., "Sensitivity of X-Ray Films. I. A Model for Sensitivity in the 1-100 keV Region," *J. Appl. Phys.* 47, 3722-3731 (1976).
27. C. M. Dozier, et. al., "Sensitivity of X-Ray Films. II. Kodak No-Screen Film in the 1-100 keV Region," *J. Appl. Phys.* 47, 3732-3739 (1976).
28. R. F. Benjamin, et. al., "X-Ray Calibration of RAR 2490 Film for Application to Laser Plasma Experiments," *Appl. Opt.* 16, 393-397 (1977).
29. G. B. Parrent and B. J. Thompson, Physical Optics Notebook, Society of Photo-Optical Instrumentation Engineers, Redondo Beach, California, 1969, Article 14.
30. C. E. K. Mees and T. H. James, The Theory of the Photographic Process, 3rd ed., Macmillan, New York, 1966, Chapter 10.
31. R. J. Collier, C. B. Burckhardt, and L. H. Lin, Optical Holography, Academic Press, New York, 1971, p. 338.

32. G. Oster, et. al., "Theoretical Interpretation of Moire Patterns," J. Opt. Soc. Am. 54, 169-173 (1964).
33. H. H. M. Chau, "Moire Pattern Resulting from Superposition of Two Zone Plates," Appl. Opt. 8 1707-1712 (1969).
34. H. H. M. Chau, "Properties of Two Overlapping Zone Plates of Different Focal Lengths," J. Opt. Soc. Am. 60, 255-258 (1970).
35. H. M. Smith, Principles of Holography, John Wiley and Sons, New York, 1975, p. 133.
36. R. L. Lamberts and C. N. Kurtz, "Reversal Bleaching for Low Flare Light in Holograms," Appl. Opt. 10, 1342-1347 (1971).
37. R.L. Lamberts, "Characterization of a Bleached Photographic Material," Appl. Opt. 11, 33-41 (1972).
38. M. Chang and N. George, "Holographic Dielectric Grating: Theory and Practice," Appl. Opt. 9, 713-719 (1970).
39. J. F. Hamilton, "The Photographic Grain," Appl. Opt. 11, 13-21 (1972).
40. M. Born and E. Wolf, Principles of Optics, 5th ed., Pergamon Press, Oxford, 1975, Chapter 13.
41. R. L. Van Renesse, "Scattering Properties of Fine-Grained Bleached Emulsions," Phot. Sci. Eng. 24, 114-119 (1980).
42. N. J. Phillips, et. al., "Advances in Holographic Bleaches," Phot. Sci. Eng. 24, 120-124 (1980).
43. J. W. Goodman, "Film-Grain Noise in Wavefront-Reconstruction Imaging," J. Opt. Soc. Am. 57, 493-502 (1967).
44. A. Kozma, "Effects of Film-Grain Noise in Holography," J. Opt. Soc. Am. 58, 436-438 (1968).
45. C. B. Burckhardt, "Storage Capacity of an Optically Formed Spatial Filter for Character Recognition," Appl. Opt. 6, 1359-1366 (1967).
46. G. B. Brandt, "Coherent Optical Power Spectra of Photographic Materials," Appl. Opt. 9, 1424-1428 (1970).
47. H. M. Smith, "Light Scattering in Photographic Materials for Holography," Appl. Opt. 11, 26-32 (1972).
48. N. M. Ceglio and J. T. Larson, "Spatially Resolved Suprathermal X-Ray Emission from Laser-Fusion Targets," Phys. Rev. Lett. 44, 579-581 (1980).
49. Shannon and Weaver, The Mathematical Theory of Communication, University of Illinois Press, Urbana, Illinois, 1962.

50. B. L. Henke and M. A. Tester, "Techniques of Low Energy X-Ray Spectroscopy," in Advances in X-Ray Analysis, V. 18, Plenum Press, New York, 1975, pp. 76-106.
51. See reference 11, p. 56, equation 2-21-a.
52. A. Graube, "Advances in Bleaching Methods for Photographically Recorded Holograms," Appl. Opt. 13, 2942-2946 (1974).
53. F. Kalk and D. Glocker, "Thick Zone Plate Fabrication Using Reactive Sputter Etching," submitted for publication.
54. D. Ciarlo and N. Cegliò, "Ultrathick Photoresist Processing," in Proceedings of SPIE Symposium on Semiconductor Microlithography, San Diego, March, 1980.
55. H. Lehmann and R. Widmer, "Dry Etching for Pattern Definition," J. Vac. Sci. Technol. 15, 319 (1978).
56. I. S. Goldstein and F. Kalk, "Oxygen Plasma Etching of Thick Polymer Layers," to be published in J. Vac. Sci. Technol., 1981.

APPENDIX I

FILM PROCESSING METHODS

A.1.1 Processing of Kodak RAR 2491 Film

Develop: D-19 6 min.
 Stop: Indicator stop bath 30 sec.
 Rinse: Running H₂O 30 sec.
 Fix: Rapid Fixer 3 min.
 Rinse: H₂O 2 min.
 Clear: Perma Wash 1 min.
 Rinse: H₂O 1 min.
 De-spot: Photo Flo 30 sec.
 Air Dry

A.1.2 Processing of Kodak 649-F Plates

Develop: D-19 5 min.
 Stop: Indicator stop bath 30 sec.
 Rinse: H₂O 30 sec.
 Fix: Rapid Fixer 5 min.
 Rinse: H₂O 2 min.
 Clear: Perma Wash 2 min.
 Rinse: H₂O 2 min.
 De-spot: Photo Flo 30 sec.
 Air Dry

A.1.3 Bleaching of Kodak 649-F Plates

After the final rinse of Section A.1.2, the following steps were performed:

Bleach: Brominated methanol (5-10%) until clear
 Rinse: Methanol:H₂O 1:1
 Rinse: Methanol
 Dry: Forced air or N₂

A.1.4 Measurement of Optical Density of Processed Films

Density of each film specimen was measured on a Joyce Loebel 3CS microdensitometer and converted to amplitude transmittance with the equation $t = 10^{-D/2}$. Uniformly exposed films and copies of coded images were surveyed in areas of uniform density (for the copies, these areas were around the outside of the coded image).

APPENDIX II

THICK ZONE PLATE FABRICATION

High energy imaging presents a challenging aperture fabrication problem. Zone plate and pinhole cameras have lateral spatial resolutions proportional to the smallest lateral aperture structure. But adequate shadowgraphy contrast depends upon aperture thickness, so the objective in zone plate fabrication is a large thickness-to-linewidth ratio (aspect ratio). This section deals with the use of dry etching to delineate aperture patterns and the resultant fabrication capabilities.⁽⁵³⁾

Gold micro-Fresnel zone plates are made by producing a negative mold at least as thick as the desired product, and then electroplating gold into the voids. Usually this mold is formed photolithographically in thick layers of photoresist, as outlined in Figure A.1. The most difficult steps are 2, 3, and 4, which will be termed pattern delineation steps. The processing schedule for photoresist layers thicker than about 15 μm is very demanding. Ciarlo and Ceglio⁽⁵⁴⁾ have succeeded in delineating patterns as thick as 40 μm in photoresist, but many problems are in evidence. For example, cracks and bubbles can occur during u.v. exposure, and resist layers can exhibit thickness nonuniformities. These problems, though imposing, can be overcome with proper care in processing, but a more fundamental problem is zone tapering, which is due to diffractive spreading of the exposure illumination by the fine details in the photomask. The maximum aspect ratio achieved by the standard technique is about four, while zone plates with aspect ratios as high as ten would prove useful for imaging experiments.

To avoid the problems inherent in thick photoresist processing,

ZONE PLATE FABRICATION SEQUENCE

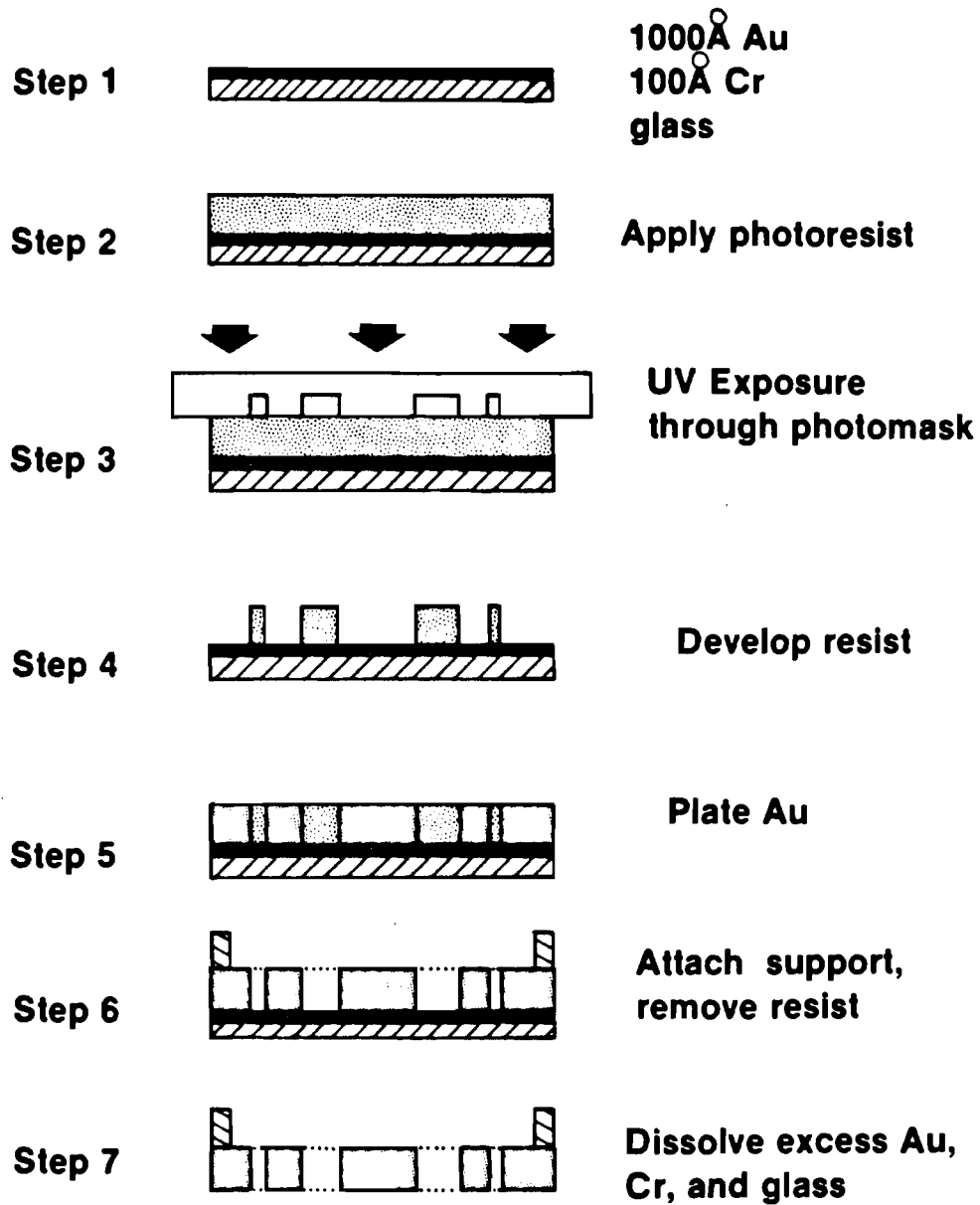


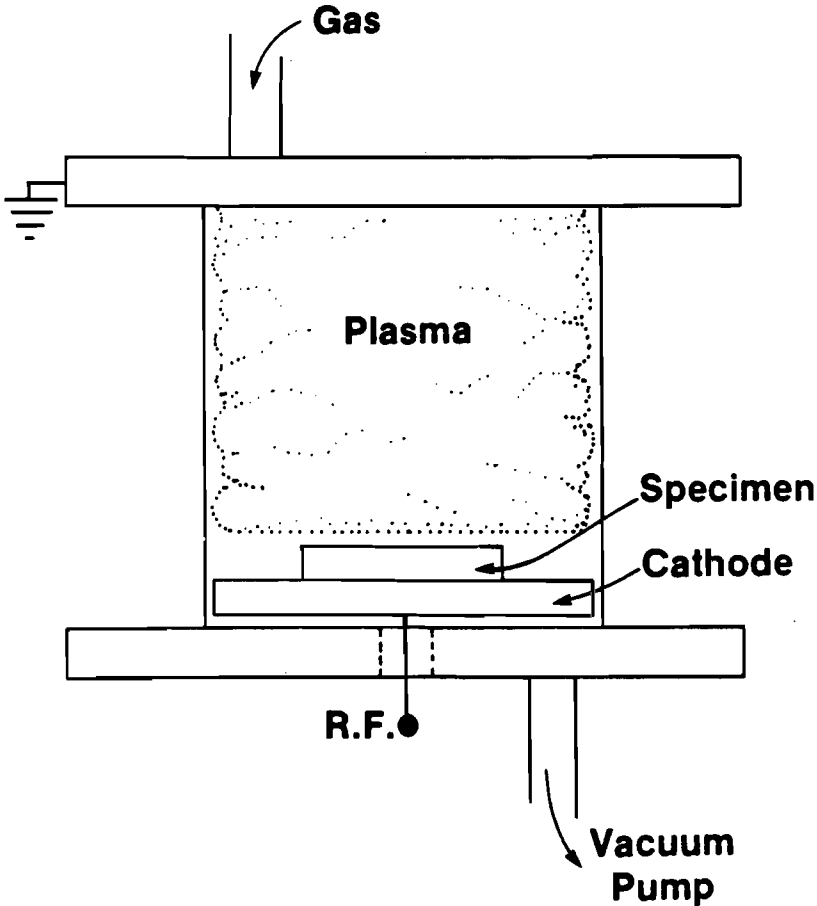
Figure A.1

reactive sputter etching (RSE)⁽⁵⁵⁾ has been employed to delineate thick molds. Figure A.2 is a schematic of the RSE apparatus. A radio frequency glow discharge sustains a plasma in a gas which is being pumped through a chamber at low pressure. The specimen to be etched is placed on the cathodic electrode. The gas is chosen so that it will chemically react with the specimen, creating volatile reaction products which are pumped away by the vacuum system. The mechanisms in the RSE process are not completely understood, but RSE is known to be somewhat material specific (due to its chemical nature) and highly directional (presumably due to the acceleration of "reactive ions" in the discharge) as well. Organic media can be reactively etched in a 13.56 MHz oxygen discharge at rates approaching 250 nm/min., while oxygen etches inorganic media much more slowly.⁽⁵⁶⁾

A thick zone plate mold can be delineated with RSE as shown in Figure A.3. The thick polymer applied in step 2 is coated with a thin film of an inorganic material with a low etch rate in O₂. A thin (500 nm) photoresist film is spun onto the top layer, and the zone plate pattern is photolithographically delineated into the resist. Wet or dry etching can be used to transfer the zone plate pattern into the inorganic material, which serves as an etch mask in the subsequent O₂ RSE step (step 4). Steps 5 through 7 are unchanged from the original process.

Crucial to the RSE method of pattern delineation is the choice of the polymer and mask materials such that the RSE step will etch only the polymer. The polymer must be capable of being deposited in thick, uniform layers and must withstand the processing steps which

SCHEMATIC DIAGRAM OF REACTIVE SPUTTER ETCHER



T236

Figure A.2

ULTRATHICK ZONE PLATE FABRICATION

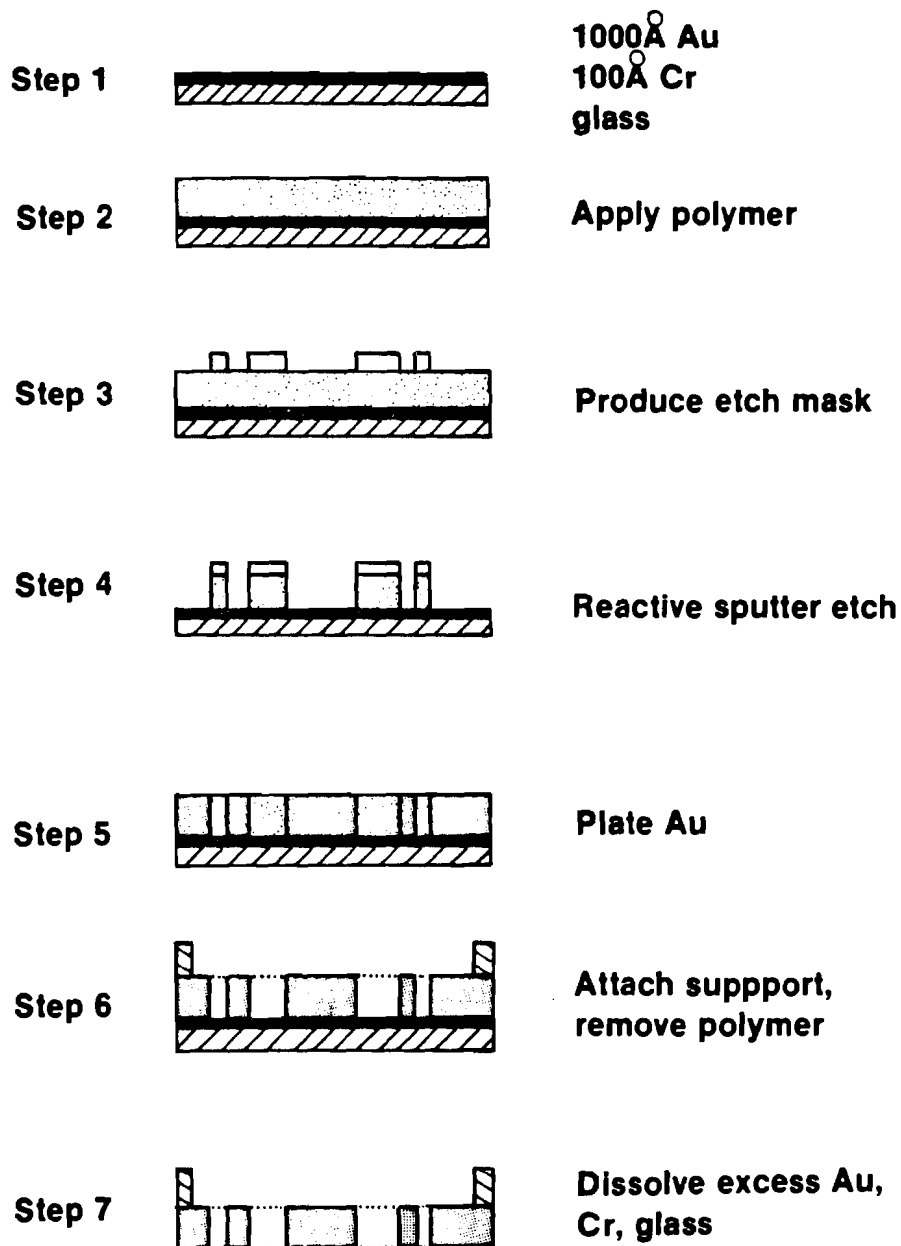


Figure A.3

follow pattern delineation, including gold plating and wet chemical etching. In addition, since an integral etch mask is required, it must be possible to deposit metal films with excellent adhesion to the polymer.

To date, an ideal polymer has not been found. Consequently, a somewhat different fabrication procedure was adopted. A standard piece of mylar film of the desired thickness (in this case 50 μm) was coated on both sides with approximately 400 nm of aluminum. One side was then coated with approximately 200 nm of gold. The gold surface was epoxied to a glass cover slip, which offered the support necessary for the subsequent steps. A thin layer of positive photoresist was spun on the Al surface and exposed through a zone plate mask. After resist development, the exposed aluminum was chemically etched away, leaving an integral Al mask on the mylar. The masked mylar was then reactively etched in O_2 at a power density of 0.28 W/cm^2 , a pressure of 10 mT, and a flowrate of 15 cc/min to delineate the zone plate pattern in the mylar and expose the Al at the back surface of the mold. The backing layer of Al served to protect the Au during etching and was subsequently chemically removed. Gold was then electroplated into the mold, and the gold-mylar assembly was epoxied to a supporting ring. The final step consisted of placing the zone plate in the RSE and etching away the mylar. Figures A.4 and A.5 are scanning electron micrographs of a mylar mold and a gold zone plate made by this method. The zone plate thickness is 40 μm , and the outer zone width is 15 μm . The radial struts are 5 μm wide, but their thicknesses are somewhat less than 40 μm due to

Figure A.4 Scanning Electron Micrograph of a Mylar Zone Plate Mold.

The mold was produced by the method described in the text. Note the vertical sidewalls. The smallest crevices are about fifty microns deep and five microns wide.

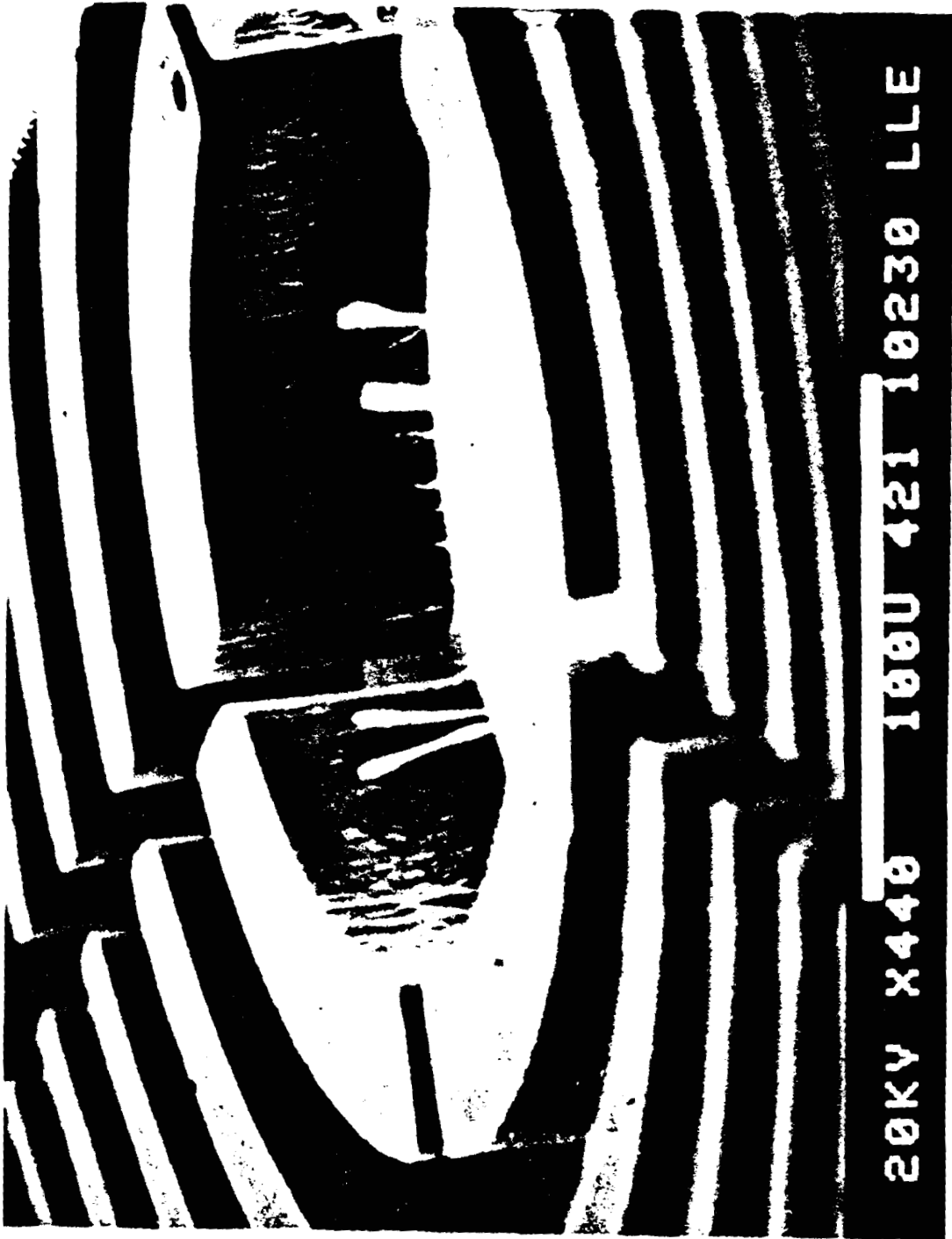


Figure A.4

Figure A.5 Scanning Electron Micrograph of a Thick Zone Plate.

The technique employed to fabricate this zone plate can be used to create high aspect ratio microstructures with virtually arbitrary linewidths.

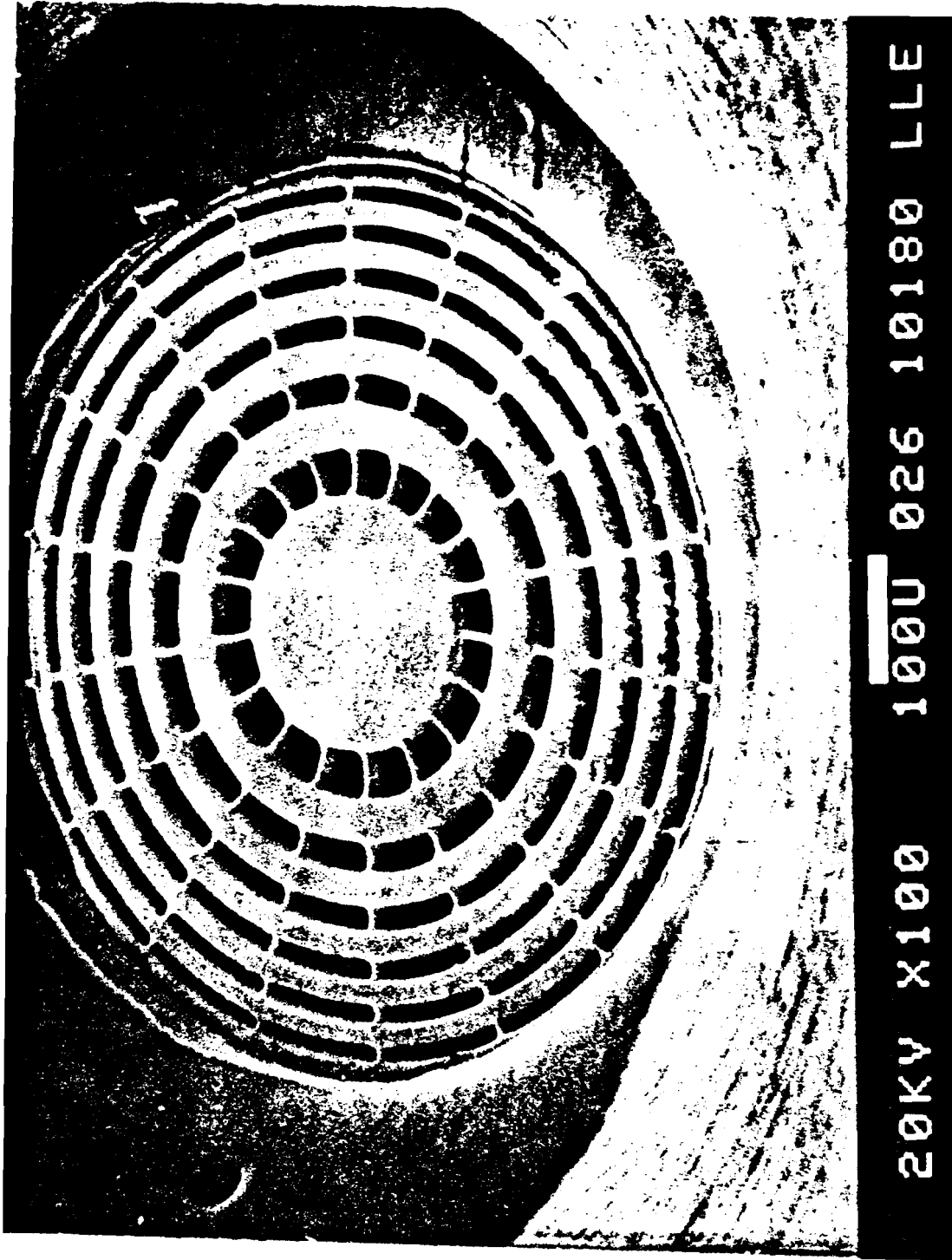


Figure A.5

what appears to be a dependence of the RSE rate on either (1) electric field distortion effects from the conducting mask,⁽⁵⁵⁾ or (2) channel aspect ratio. This effect is the subject of current investigation and is not believed to be a fundamental obstacle to the fabrication of high aspect ratio microstructures. Figure A.6 is a micrograph of a mold pattern illustrating the departure of the zone sidewalls from a perfectly vertical geometry.

The fabrication of high aspect ratio zone plates makes possible submicron imaging of 3.5 MeV α -particle emissions from laser fusion targets, high resolution imaging (5 μm) of high energy plasma x-ray emissions (10-100 keV x-rays), and even possibly submicron imaging of soft x-ray emissions (1-10 keV) from the same plasmas. The work outlined here is the first step toward realizing those goals.

Figure A.6 Photograph Illustrating Nonvertical Sidewalls of a Zone Plate Mold.

In this photo, the zones are about eight microns wide at the top. The reason for the nonvertical nature of the zones is not known at this time. One possible explanation is the deviation of the etchant ion trajectories by electric field distortion due to the presence of the metal (Al) etch mask. Another explanation is that the incoming etchant ions "wander" in the channels because they undergo abnormally high collision rates there. Such rates would be caused by locally high densities of the volatile reaction products in the vicinity of a surface being etched.



Figure A.6